Cylindrical Machining Workpiece Temperature and Bore Cylindricity

by

Lei Chen

A dissertation submitted in partial fulfillment
of the requirements for the degree of
Doctor of Philosophy
(Mechanical Engineering)
in The University of Michigan
2017

Doctoral Committee:

Professor Albert J. Shih, Chair
Professor Pingsha Dong
Assistant Professor Chinedum E. Okwudire
Dr. Juhchin A. Yang, Ford Motor Company

Lei Chen

leichan@umich.edu

ORCID iD: 0000-0003-4042-9912

DEDICATION

This dissertation is dedicated to my beloved parents, Douren Chen and Liting Du, for making me who I am, and to my beautiful fiancée Ke Liu, for loving and supporting me all the way.

ACKNOWLEDGMENTS

I truly appreciate the help and support I have received from many people along my way to this degree.

First of all, I would like to express my deepest appreciation to my advisor, Professor Albert Shih, who has been a tremendous mentor for me. He is always there for discussing my research, revising my paper writing, improving my presentation skills, and preparing me in all aspects for the future career. He is my best role model for a diligent researcher, a supportive advisor, and an enthusiastic teacher. Also, I have received unconditional support from him both academically and personally. He is like a father to me. It has been an honor to work with and learn from him.

I would like to thank my committee member, Dr. Juhchin Yang, for providing valuable suggestions and guidance from the viewpoint of industrial needs with his broad knowledge in modelling technics. I value the time he has spent with me and I am grateful to have worked with him closely during the past two years. It is impossible to complete this research without the support from him and his virtual manufacturing team at the Ford Motor Company.

I would like to extend my deepest gratitude to my other committee members, Professors Pingsha Dong and Chinedum Okwudire for their guidance and critiquing of my research as it progressed. I really appreciate their support and advice throughout this entire process.

I would like to thank Drs. Rahul Chaudhari and Xiaozhong Song from the Timken Company for giving me a wonderful internship experience and making the hard turning experiments possible.

My special thanks go to Drs. David Stephenson and John Agapiou. I value the suggestions, guidance, and help they provided on the cylinder boring experimental studies with their expertise in machining science.

I would like to thank all my lab mates at Wu Manufacturing Research Center for providing a homelike feeling through all the support and care. Especially, I thank Dr. Roland

Chen for bringing me into the research group and guiding me in the early years of my research. I thank Dr. Bruce Tai for his guidance and patient answers to all sorts of questions through my studies. Barry Belmont, Yihao Zheng, Wenwu Wu, Jordan Kreda and Po-Ting Sung all provided me numerous supports through my research. I am also thankful to meet all my friends outside the lab who have enriched my PhD life.

Last but not the least, I owe my greatest thanks to my family. I thank my parents for their unconditional love and support for decades to make me who I am today. I thank my fiancée Ke, who has been a constant source of support and encouragement during the challenges of graduate school and life, who has sacrificed incredibly to see me through this, and whom I so longingly look forward to spend the future life with.

TABLE OF CONTENTS

LIST OF TABLES

LIST OF FIGURES

ABSTRACT

Cylindrical machining processes are widely used in industry to achieve better dimensional and geometrical tolerances and finer surface finish on cylindrical workpieces. Hard turning is utilized to machine hardened steels for large bearing rings and finish boring is used to machine cylinder bores during automotive engine block production. Workpiece temperature is critical for cylindrical machining processes. In hard turning, high machined surface temperature leads to the formation of white layer, reducing the workpiece fatigue life. In finish boring, thermal expansion due to workpiece temperature rise causes bore cylindricity errors, leading to engine performance issues. Besides thermal expansion, other factors like cutting force, spindle, and fixture/clamping also affect the bore cylindricity in finish boring. This dissertation studied the cylindrical machining workpiece temperature through both experiment and modelling and identified bore cylindricity error sources in finish boring.

Firstly, two experimental methods were developed to measure machined surface temperatures in hard turning. The first method, based on a tool-foil thermocouple, estimated the machined surface temperature using a metal foil embedded in the workpiece to measure the tool tip temperature. The second method used a thermocouple embedded in the tool with its tip continuously sliding on the machined surface behind the cutting edge. The inverse heat transfer method was applied on a three-dimensional thermal model to find the machined surface temperature near the cutting edge. These two methods, although based on distinct approaches, gave correlated predictions in hard turning tests, indicating both to be feasible for the measurement of hard turning machined surface temperatures.

Secondly, four finite element method (FEM) models, namely the advection model, surface heat model, heat carrier model and ring heat model, were studied to predict the workpiece temperature in finish boring. Cylinder boring experiments were conducted to measure the workpiece temperature and evaluate the capability of four models in terms of accuracy and efficiency. Results showed good correlations between model-predicted and experimentally-

measured temperatures. Advantages and disadvantages of each model were discussed. For studying detailed cylinder boring workpiece temperature, it was suggested to use the ring heat model to estimate the moving heat flux and the heat carrier model for local workpiece temperature calculation.

Thirdly, experimental and FEM analysis was combined to identify the bore cylindricity error sources in finish boring. Experiments were conducted to measure the workpiece temperature, cutting and clamping forces, spindle error, and bore shape. FEM analysis of the workpiece temperature, thermal expansion, and deformation due to cutting and clamping forces was performed. The coordinate measurement machine (CMM) measurements of the bore after finish boring showed the 5.6 μm cylindricity and a broad spectrum from 2nd to 10th harmonics. The FEM revealed effects of workpiece thermal expansion (1.7 μm cylindricity), deformation due to cutting force (0.8 μm cylindricity), and clamping force (1.9 μm cylindricity) on the finished bore and the dominance by the 1st to 3rd harmonics using the three-jaw fixture. The spindle synchronous radial error motion (3.2 μm cylindricity) was dominated by 4th and higher order harmonics and matched well with the high (above 4th) harmonics in CMM measurements (2.9 μm cylindricity). The spindle error was found to be the dominant error source for bore cylindricity in finish boring.

The experimental methods, FEM models and approaches developed in this dissertation provide better understanding of cylindrical machining processes and are useful for optimization of the process parameters.

CHAPTER 1
INTRODUCTION

1.1 Motivation

Cylindrical machining processes remove material from a cylindrical workpiece to achieve better dimensional and geometrical tolerances and finer surface finish. Generation of external surfaces by cylindrical machining is referred to as turning. When applied to inner surfaces, it is called boring. Both types of cylindrical machining processes are widely used in industry.

Hard turning, the single-point turning of hardened parts with over 45 Rockwell C hardness, is common in the production of precision mechanical power transmission components such as bearings [1]. One major problem in the hard turning of hardened AISI 52100 bearing steel is the formation of white layer [1-5], a hard and brittle layer of un-tempered martensite with refined grains. After polishing and etching, the white layer appears featureless and white when viewed under an optical microscope. Severe plastic deformation and high machined surface temperatures lead to the formation of white layers in hard turning. A mechanically induced white layer can be beneficial, as it generates compressive residual stress and increases the fatigue life of machined surfaces [1,2]. However, a thermally induced white layer may be harmful. The high machined surface temperature results in tensile residual stress, which can reduce fatigue life [1,2]. For worn cutting tools, the thermal effect becomes dominant in hard turning white layer formation [3,4]. Once the workpiece temperature exceeds the austenitization temperature, martensitic phase transformation takes place and leads to thermally induced white layers [5]. Accurate experimental measurement of the machined surface temperature is important for a better understanding of hard turning in production.

There have several existed experimental methods in literatures to measure tool and workpiece temperatures in single-point turning, including the radiation thermometry [6-8], tool-

workpiece thermocouple [9-12], and embedded thermocouple [13-15]. Most of proposed methods were focused on cutting tool temperature, tool-chip interface temperature and workpiece temperature millimeters away from the machined surface. There are limited experimental methods for accurately measuring the machined surface workpiece temperature in hard turning.

Boring is a machining process to enlarge a hole for better tolerances and surface finish. Finish boring is a critical process for machining an accurate cylinder for engine block, hydraulic actuator, pumps, and other precision mechanical components. The geometrical accuracy of cylinders is defined by cylindricity, which is critical to the product performance. Using the cylinder bore in engine block as an example, cylindricity is important for the engine power, oil consumption, and piston ring friction [16-18]. The cylindricity tolerance specifies a tolerance zone bounded by two concentric cylinders within which the surface must lie [19]. For a typical engine cylinder of about 70 to 100 mm in diameter, the typical cylindricity tolerance is about 20 to 25 μm. To achieve such accurate cylindricity, a three-pass cylinder boring process, including the rough boring, semi-finish boring, and finish boring, is common in the engine block production. Finish boring is the machining process to achieve the cylinder bore dimensional and geometrical accuracy before the subsequent honing process. Workpiece thermal expansion resulted by the high local temperature during finish boring is one of the sources causing the bore cylindricity error [20-25]. To study thermal expansion induced bore distortion, detailed workpiece temperature distribution in finish boring is required.

Experimental [22-25], analytical [22, 25] and numerical [21, 23, 24] methods have been utilized to study the workpiece temperature in boring. The experimentally measured temperature at a single point is used as the input for the inverse heat transfer problem to determine the heat flux in thermal models. The experimental approaches, in general, lack the spatial and temporal resolution to measure the workpiece temperature which is rapidly changing (in the time domain) and has a large gradient on the machined surface (in the spatial domain). Analytical models are limited to simple, cylindrical geometry and often oversimplify the temperature field. For cylinder bores in an engine block, the numerical method, especially finite element method (FEM) is preferred with its capability to handle complex geometries. However, simulating finish boring of a large diameter cylinder with a small depth of cut is still challenging due to the very fine mesh and extensive computational capacity required to model the local temperature rise. There is lack of FEM techniques to address this technical challenge accurately and efficiently for workpiece

temperature distribution calculation in finish boring.

Besides workpiece thermal expansion, cutting force, machine tool (particularly spindle), and fixture/clamping all lead to cylindricity errors in finish boring. Cutting force leads to deformation of workpiece and deflection of the boring tool [20-22]. On machine tool, the spindle error changes the tool trajectory thus affects the bore shape [26-28]. After boring, the fixture and clamping forces reach a new state with a thinner liner. The clamping force is a potential cylindricity error source depending on the workpiece geometry. It is important to clarify the contribution from each error source for better understanding and parameter optimization of finish boring process.

Research has been conducted to study the cylindricity in boring [20-23]. It was reported that workpiece geometry around the cylinder bore and thermal expansion of the bore are major factors determining the bore cylindricity. There is a lack of accurate thermal models to predict the workpiece temperature and thermal expansion in finish boring. Also, previous studies were based on the assumption of no machine nor spindle error. In finish boring process, the cylindricity error is usually within 10 μm. The machine and spindle error at the cutting tip (about 200 mm from the spindle) will be in the μm level and needs to be considered as an error source for cylindricity in finish boring. There lacks a bore cylindricity error source identification considering all the aforementioned error sources under finish boring cutting conditions.

1.2 Research Goal and Objectives

The ultimate goal of this study is to provide better understandings of workpiece temperature and bore cylindricity error formation during cylindrical machining processes. To achieve this goal, three specific objectives are summarized as the following:

(1) Develop experimental methods to measure machined surface temperature in hard turning process and validate the methods through experiments. The methods should be capable of measuring workpiece temperature near the cutting edge.

(2) Develop computational models to evaluate workpiece temperature distribution in finish cylinder boring, compare the accuracy and efficiency through case studies, and find the proper modelling concepts and strategies for the best trade-off.

(3) Clarify the amount of bore cylindricity error resulting from each error source during finish cylinder boring process and validate it through experiments and simulations.

Fulfillment of the objectives will help accurate and efficient evaluation of the workpiece temperature during cylindrical machining processes and thus mitigate the thermal induced issues. Bore cylindricity error source identification approach will be applicable to engine block cylinder boring development to optimize the process parameters for boring, help planning the subsequent honing operations to correct the bore shape and eliminate the need for some of the subsequent processes.

1.3 Organization of the Dissertation

The rest of this dissertation is organized as follows.

In Chapter 2, the tool-foil thermocouple method and the embedded thermocouple method together with the corresponding FEM thermal models and inverse heat transfer method are developed to measure machined surface temperature in hard turning. Hard turning experiments are conducted to validate these two methods.

In Chapter 3, four FEM thermal models for finish boring workpiece temperature are introduced. Finish boring experiment is conducted for model comparison. The FEM simulation results are compared with experimental measurements from embedded thermocouples and the tool-foil thermocouple. Advantages, disadvantages and applicable scenarios of the four models are discussed in terms of accuracy and efficiency.

In Chapter 4, finish boring bore cylindricity error source identification is presented. Experimental setups for finish boring and coordinate measuring machine (CMM) and spindle error measurement are introduced. FEM for calculation of the workpiece temperature, thermal expansion, and workpiece deformation due to cutting and clamping forces are presented. Experimental and FEM results are elaborated for error source identification through harmonic analysis.

In Chapter 5, the conclusions and contributions of this dissertation are summarized, and possible future works are proposed.

References

[1] A. Ramesh, S.N. Melkote, L.F. Allard, L. Riester, T.R. Watkins, Analysis of white layers formed in hard turning of AISI 52100 steel, Materials Science and Engineering 390 (1) (2005) 88-97.

[2] Y.B. Guo, A.W. Warren, F. Hashimoto, The basic relationships between residual stress, white layer, and fatigue life of hard turned and grinded surfaces in rolling contact, CIRP Journal of Manufacturing Science and Technology 2 (2) (2010) 129-134.

[3] Y.K. Chou, C.J. Evans, White layers and thermal modeling of hard turned surfaces, International Journal of Machine Tools and Manufacture 39 (12) (1999) 1863-1881.

[4] Y.K. Chou, H. Song, Thermal modeling for white layer predictions in finish hard turning, International Journal of Machine Tools and Manufacture 45 (4) (2005) 481-495.

[5] Y.B. Guo, G.M. Janowski, Microstructural characterization of white layers by hard turning and grinding, Trans. NAMRI/SME 32 (2004) 367-374.

[6] T. Ueda, M. Al Huda, K. Yamada, K. Nakayama, H. Kudo, Temperature measurement of CBN tool in turning of high hardness steel, CIRP Annals-Manufacturing Technology 48 (1) (1999) 63-66.

[7] E.G. Ng, D.K. Aspinwall, D. Brazil, J. Monaghan, Modelling of temperature and forces when orthogonally machining hardened steel, International Journal of Machine Tools and Manufacture 39 (6) (1999) 885-903.

[8] M. Al Huda, K. Yamada, A. Hosokawa, T. Ueda, Investigation of temperature at tool-chip interface in turning using two-color pyrometer, Journal of Manufacturing Science and Engineering 124 (2) (2002) 200-207.

[9] D.A. Stephenson, Tool-work thermocouple temperature measurements - theory and implementation issues, Journal of Engineering for Industry 115 (4) (1993) 432-437.

[10] C.E. Leshock, Y.C. Shin, Investigation on cutting temperature in turning by a tool-work thermocouple technique, Journal of Manufacturing Science and Engineering 119 (4A) (1997) 502-508.

[11] A.U. Anagonye, D.A. Stephenson, Modeling cutting temperatures for turning inserts with various tool geometries and materials, Journal of Manufacturing Science and Engineering 124 (3) (2002) 544-552.

[12] M. Bono, J. Ni, A method for measuring the temperature distribution along the cutting edges of a drill, Journal of Manufacturing Science and Engineering 124 (4) (2002) 921-923.

[13] T.I. El-Wardany, E. Mohammed, M.A. El-Bestawi, Cutting temperature of ceramic tools in high speed machining of difficult-to-cut materials, International Journal of Machine Tools and Manufacture 36 (5) (1996) 611-634.

[14] X.J. Ren, Q.X. Yang, R.D. James, L. Wang, Cutting temperatures in hard turning chromium hardfacings with PCBN tooling, Journal of Materials Processing Technology 147 (1) (2004) 38-44.

[15] J. L. Battaglia, L. Puigsegur, O. Cahuc, Estimated temperature on a machined surface using an inverse approach, Experimental Heat Transfer 18 (1) (2005) 13-32.

[16] Z. Ma, N.A. Henein, W. Bryzik, J. Glidewell, Break-in liner wear and piston ring assembly friction in a spark-ignited engine, Tribology Transactions 41 (4) (1998) 497-504.

[17] M.R. Rodrigues, S.F. Porto, S.F., Torque plate honing on block cylinder bores, SAE Technical Paper 931679 (1993).

[18] K. Matsuo, S. Kiga, S. Murata, N. Satou, H. Miyake, K. Suzuki, K. Sugiyama, T. Monchujo, Reduction of piston system friction by applying a bore circularity machining technique to the cylinder block, SAE Technical Paper 2005-01-1656 (2005).

[19] J.D. Meadows, Geometric Dimensioning and Tolerancing Handbook: Applications, Analysis & Measurement, ASME Press, New York, 2009.

[20] G. Subramani, S.G. Kapoor, R.E. DeVor, A model for the prediction of bore cylindricity during machining, Journal of Manufacturing Science and Engineering 115 (1) (1993) 15-22.

[21] N.N. Kakade, J.G. Chow, Finite element analysis of engine bore distortions during boring operation, Journal of Manufacturing Science and Engineering 115 (4) (1993) 379-384.

[22] Y. Zheng, H. Li, W.W. Olson, J.W. Sutherland, Evaluating cutting fluid effects on cylinder boring surface errors by inverse heat transfer and finite element methods, Journal of Manufacturing Science and Engineering 122 (3) (2000) 377-383.

[23] Y. Tang, K. Ding, H. Sasahara, K. Nishimura, T. Watanabe, Clarification of the amount of machining error resulting from the cutting force and thermal expansion during the cylinder liner boring process, Journal of Advanced Mechanical Design, Systems, and Manufacturing 2 (3) (2008) 332-342.

[24] Y. Tang, H. Sasahara, Investigation of thermal behavior on cylinder liner during its boring process, International Journal of Machine Tools and Manufacture 47 (14) (2007) 2162-2171.

[25] G. Subramani, M.C. Whitmore, S.G. Kapoor, R.E. DeVor, Temperature distribution in a hollow cylindrical workpiece during machining: theoretical model and experimental results, Journal of Manufacturing Science and Engineering 113 (4) (1991) 373-380.

[26] K. Kim, K.F. Eman, S.M. Wu, In-process control of cylindricity in boring operations, Journal of Engineering for Industry 109 (4) (1987) 291-296.

[27] D.L. Martin, A.N. Tabenkin, F.G. Parsons, Precision spindle and bearing error analysis, International Journal of Machine Tools and Manufacture 35 (2) (1995) 187-193.

[28] J.P. Choi, S.J. Lee, H.D. Kwon, Roundness error prediction with a volumetric error model including spindle error motions of a machine tool, The International Journal of Advanced Manufacturing Technology 21 (12) (2003) 923-928.

CHAPTER 2
MEASUREMENT OF MACHINED SURFACE TEMPERATURE IN HARD TURNING

2.1 Introduction

Hard turning, the single-point turning of hardened parts with over 45 Rockwell C hardness, is common in the production of precision mechanical power transmission components such as bearings [1]. One major problem in the hard turning of hardened AISI 52100 bearing steel is the formation of the white layer [1-5], a hard and brittle layer of un-tempered martensite with refined grains. After polishing and etching, the white layer appears featureless and white when viewed under an optical microscope. Severe plastic deformation and high machined surface temperatures lead to the formation of white layers in hard turning. A mechanically induced white layer can be beneficial, as it generates compressive residual stress and increases the fatigue life of machined surfaces [1,2]. However, a thermally induced white layer may be harmful. The high machined surface temperature results in tensile residual stress, which can reduce fatigue life [1,2]. For worn cutting tools, the thermal effect becomes dominant in hard turning white layer formation [3,4]. Once the workpiece temperature exceeds the austenitization temperature, martensitic phase transformation takes place and leads to thermally induced white layers [5]. Accurate experimental measurement of the machined surface temperature, the topic of this chapter, is important for a better understanding of the hard turning process in production.

There have existed several experimental methods in literatures to measure tool and workpiece temperatures in single-point turning, including the radiation thermometry [6-8], tool-workpiece thermocouple [9-12], and embedded thermocouple [13-15].

Radiation thermometry is a non-contact temperature measurement method and it is feasible for tool and chip temperature measurement. Ueda et al. [6] measured the temperature at tool flank

using a pyrometer with an optical fiber coupler through a pre-drilled hole in the workpiece. Ng et al. [7] used an infrared pyrometer to measure the chip surface temperature in hard turning. Al Huda et al. [8] investigated the tool-chip interface temperature with a pyrometer through an optical fiber embedded inside the cutting tool. As for workpiece temperature measurement, if the workpiece is stationary, an embedded pyrometer may be effective for measuring the machined surface temperature. However, the workpiece rotates during hard turning, and with radiation thermometry it is difficult to reach the newly exposed machined surfaces. The emissivity of the machined surface is another challenge for accurate radiation thermometry measurement [16].

The tool-workpiece thermocouple measures the average temperature at the interface between the tool and workpiece [9-12]. This tool-workpiece interface temperature may provide a reasonable estimate of the machined surface temperature during hard turning [11]. Inspired by the drill-foil thermocouple method for drilling temperature measurement [12], a thermocouple between the cutting tool and a foil embedded in the workpiece is investigated during hard turning to ascertain the temperature at the tool tip and machined surface interface. This is a conservative approach to estimate the machined surface temperature under the assumption that a steady state temperature at the tool-workpiece interface is reached during the hard turning process.

Embedded thermocouple method is also widely used in temperature studies of hard turning. El-Wardany et al. [13] embedded a thermocouple in a grinded recess on the tool rake face to measure the tool temperature during hard turning. Ren et al. [14] clamped a thermocouple between the tool and shim to remotely evaluate tool-chip temperature. Battaglia et al. [15] placed embedded thermocouples inside the rotating workpiece and conducted temperature measurement millimeters away from the machined surface. The embedded thermocouple method has the response time, size, and wire connection constraints for direct measurement of machined surface temperature. For example, one of the smallest commercially available thermocouples has a 0.1 mm diameter tip and a 0.1-second (s) response time. However, if the thermocouple is placed in the workpiece underneath the machined surface, at the common hard turning cutting speed of 100 to 180 m/min it takes only 0.002 to 0.004 s for the tool to cut through the 0.1 mm thermocouple tip length. The contact time is thus much shorter than the thermocouple response time. It is also technically challenging to precisely embed the miniature thermocouple tip beneath the machined surface. Additionally, if the thermocouple is implanted in the tool near the cutting edge, the tool life may be affected. To overcome these obstacles, in this study, a method of sliding miniature

thermocouple tip behind the cutting edge on the newly generated machined surface is studied. This method requires the development of inverse heat transfer method and numerical thermal model for hard turning to predict the machined surface temperature.

There are few experimental methods for accurately measuring the machined surface temperature in hard turning. In this study, two methods, denoted as the "tool-foil thermocouple method" and the "embedded thermocouple method", are developed to measure machined surface temperatures in the hard turning of hardened AISI 52100 bearing steel.

The hard turning experimental setup and process parameters used in this study are first shown in Sec. 2.2. The tool-foil thermocouple method is then presented in Sec. 2.3. The embedded thermocouple method together with the corresponding Finite Element Method (FEM) thermal models and inverse heat transfer method are introduced in Sec. 2.4. The results of the hard turning experiment and temperature predictions by the two methods are shown in Sec. 2.5, followed by the discussions.

2.2 Hard Turning Experimental Setup and Process Parameters

The hard turning of large bearing rings is typically conducted on a vertical lathe, as shown in Fig. 2.1(a). The workpiece is clamped on the machine by a magnetic chuck. The workpiece rotates during turning, while the cutting tool moves in the radial and axial directions. An XYZ coordinate is defined at the tool-workpiece contact region with X in the radial direction, Y in the tangential direction and Z along the axial direction of the cylindrical workpiece. Cutting tool holder configuration and Polycrystalline Cubic Boron Nitride (PCBN) cutting insert geometry determine the oblique cutting lead, rake and relief angles, as shown in Fig. 2.1(b).

In this study, the workpiece had a 432 mm outer diameter and 356 mm inner diameter, with a height of 102 mm. The work material was AISI 52100 bearing steel through-hardened with properties characterized as 7810 kg/m^3 density, 475 J/kg·°C specific heat, 46.6 W/m·°C thermal conductivity and 58–62 Rockwell C hardness. The PCBN cutting tool used was Sumitomo DNGA432. The tool holder was Kennametal MDJNL164D. The cutting tool and tool holder together had a –5° side rake angle, 3° side lead angle, 32° end lead angle and 5° side relief angle.

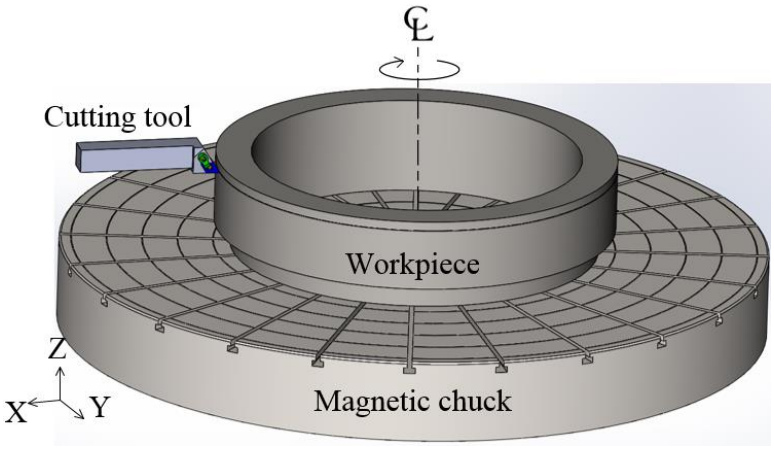

(a)

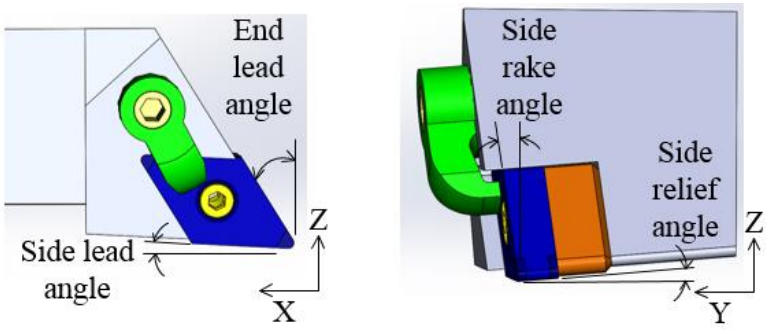

(b)

Figure 2.1 Setup for the hard turning of bearing ring on a vertical lathe: (a) an overview and (b) angles of oblique cutting.

For all hard turning tests, the radial depth of cut was 0.1 mm and cutting speed was 100 m/min. Three levels of feed at 0.05, 0.1 and 0.15 mm/rev were studied. For each hard turning test, a new tool was used to cut 12 times, with each cut lasting for 2 min (200 m length of cut). The tool-foil thermocouple and embedded thermocouple methods were used to measure the machined surface temperature for all 36 tests. Specific designs and experimental setups to implement these two machined surface temperature measurement methods are presented in the following sections.

2.3 Method I: the Tool-foil Thermocouple Method

2.3.1 Experimental Setup

Figure 2.2(a) shows the exploded view of the key components in the tool-foil thermocouple method. The workpiece consists of two bearing rings, denoted as the top bearing ring and bottom bearing ring. These two rings were positioned using two dowel pins and fixed using four clamping

bolts. Four shallow slots were grinded into the contact surfaces of the top and bottom bearing rings. After clamping the top and bottom rings, these slots formed a groove. Inside this groove was a metal foil compressed between the top and bottom insulation layers, which electrically insulated the metal foil from the workpiece. During hard turning, when the cutting tool contacted and cut the metal foil, a thermocouple junction was created between the cutting tool and metal foil. An electric brush was used to obtain the voltage signal from the rotating foil to form the tool-foil circuit, as shown in Fig. 2.2(b). This voltage signal could be converted to the interface temperature between the cutting tool tip and metal foil using a calibration curve (to be discussed in Sec. 2.3.2). Figure 2.2(c) shows the close-up cross-sectional view of the tool-foil contact region (the dashed section in Fig. 2.2(b)) in the XZ plane. The cutting tool moved along the feed (Z) direction during turning. The tool tip came in contact with the copper foil intermittently and generated voltage pulses in the tool-foil circuit (Fig. 2.2(b)). The cutting forces simultaneously recorded during hard turning tests were used to confirm the contact. While cutting the foil and insulation material, a reduction could be identified in the measured cutting force. This drop in cutting force was used to confirm the contact of tool and foil and corresponding tool-foil voltage signal during hard turning.

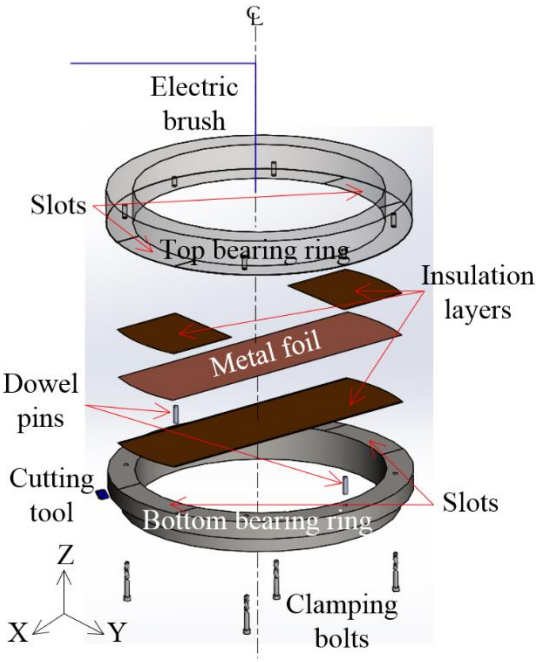

(a)

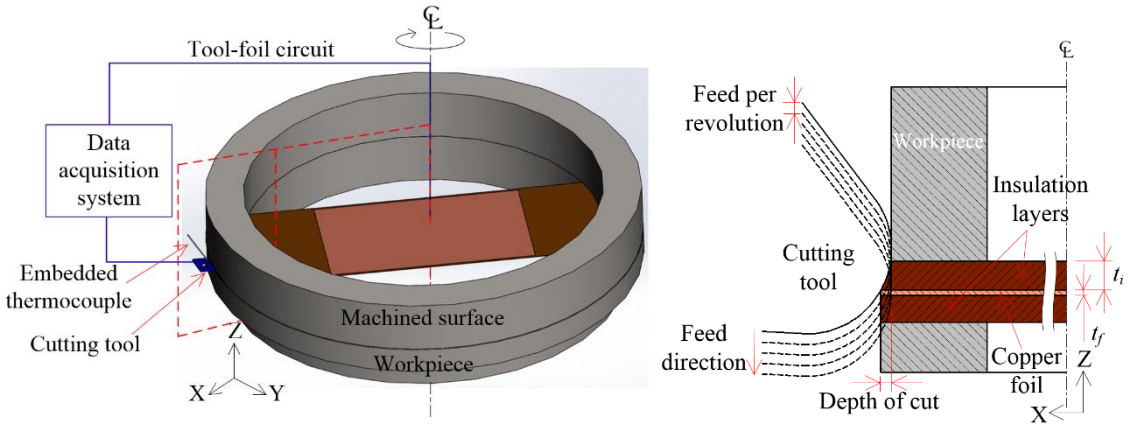

(b) (c)

Figure 2.2 The tool-foil thermocouple method: (a) exploded view, (b) overview of the setup for tool-foil voltage measurement, and (c) close-up cross-section view of the cutting tool with metal foil and insulation layers during hard turning.

Figure 2.3 shows the experimental setup of the tool-foil thermocouple method on a vertical CNC lathe (VN-50 by Fuji Machine Manufacturing, Chiryu, Japan). The insulation layers were made of polyester shim stocks with 0.25 mm thickness (t_i), as shown in the close-up side view (YZ plane) of the groove in Fig. 2.4(a). Copper C110 was selected as the foil material due to its high electrical conductivity. The copper foil thickness (t_f) was 0.05 mm. The depth of the groove (0.5 mm) was slightly smaller than the total thickness of the two insulation layers and foil (0.55 mm), in order to create sufficient compression to secure the foil during hard turning. As shown in Fig. 2.4(b),

the groove width L_S was 127 mm, which was also the width of the insulation layers. The width of the copper foil, as shown in Fig. 2.4(a), was narrower than the width of the groove by $2L_G$ to ensure proper insulation during hard turning. In this study, L_G = 2 mm. The groove and foil widths were experimentally tested to ensure proper voltage signal acquisition. A wider foil enabled a longer contact time between the embedded foil and the cutting tool to capture a large temperature gradient on the machined surface. It overcame the response time limitation of a regular thermocouple. However, a wide embedded foil could also disturb the steady-state cutting condition reached between the PCBN cutting tool and the bearing steel workpiece. As a result, an excessively wide foil would be measuring the cutting temperature of PCBN and copper instead. To reach a compromise, the arc length of the copper foil in contact with the tool was set to be 124 mm. At the 100 m/min cutting speed, the contact time between the tool and foil was 0.074 s, which was adequate for the tool-foil thermocouple junction to respond. Shorter groove widths were studied, but did not generate adequate voltage signals for the tool-foil thermocouple voltage measurement.

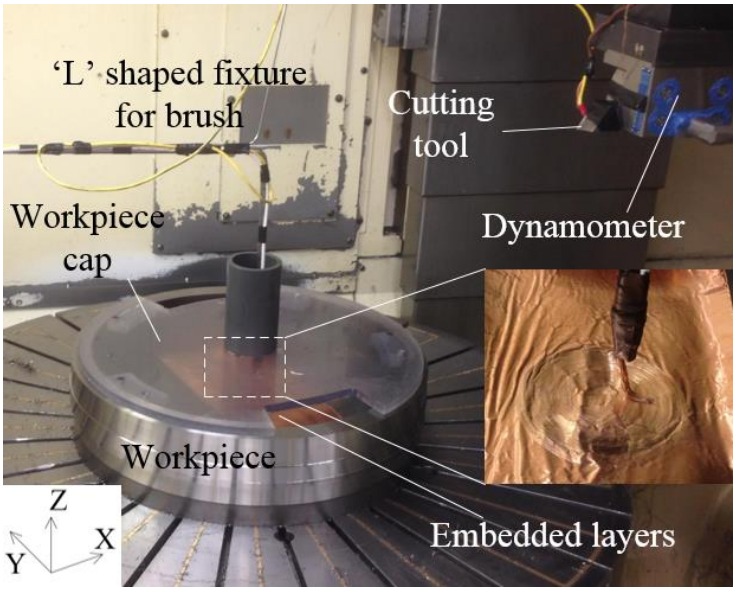

Figure 2.3 Experimental setup for hard turning tests on a vertical lathe.

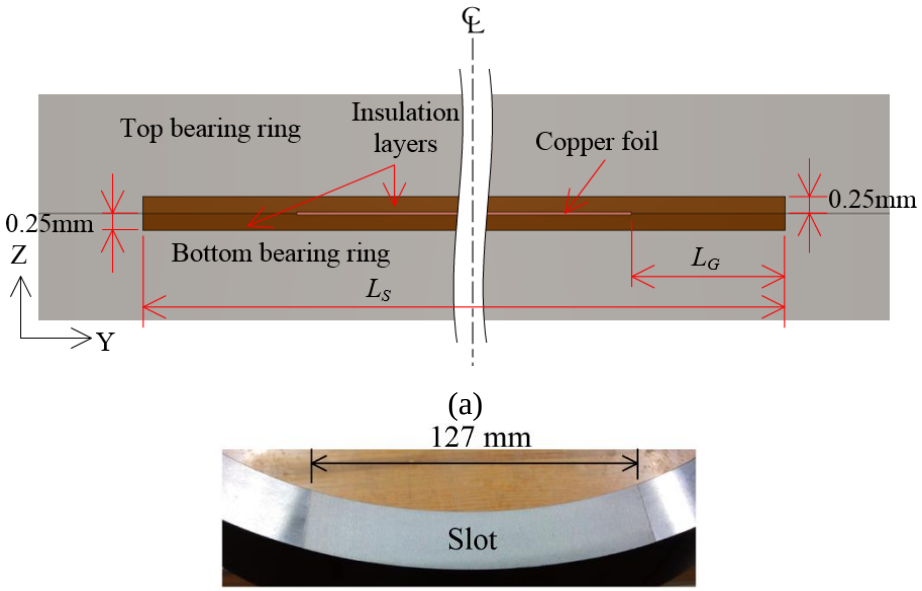

(a)

(b)

Figure 2.4 The groove with metal foil sandwiched between two insulation layers: (a) close-up side view and (b) top view of the slot grinded in the bearing ring.

To maintain the contact with the foil, an electric brush was built by preloading a bare copper wire strand using an L-shaped metal rod, as shown in Fig. 2.3. Since the brush and foil were of the same material, the friction heat generated between the brush and foil did not generate extra voltage signals. During temperature measurement, cutting-produced chips were shielded from the foil by two methods to avoid extraneous voltage signal noise. The first method applied 0.55 MPa compressed air through an air nozzle at the cutting tip, preventing chip accumulation at the tool-workpiece interface and thus the contact between chip and foil. Chip-foil contact could also occur at the center of the workpiece where the embedded foil was exposed for the brush contact. So the second method was to place a custom-built cap made of polymethyl methacrylate on the top of the workpiece, as shown in Fig. 2.3, to prevent chip contact.

2.3.2 Calibration

The output from the tool-foil thermocouple method was a voltage measurement of the tool-foil circuit. A calibration curve was needed to convert such voltage to machined surface temperature. The experimental setup for the temperature-versus-voltage calibration curve of the tool-foil thermocouple method is shown in Fig. 2.5. The copper foil and PCBN cutting tool in contact were heated by a butane torch, which can raise the temperature to over 900°C. A K-type

thermocouple was placed at the tool-foil interface. While heating, voltages generated by this K-type thermocouple and the tool-foil thermocouple were recorded simultaneously, enabling generation of a tool-foil voltage-versus-temperature calibration curve. Results of the calibration curve for the tool-foil thermocouple method will be presented in Sec. 2.5.1.

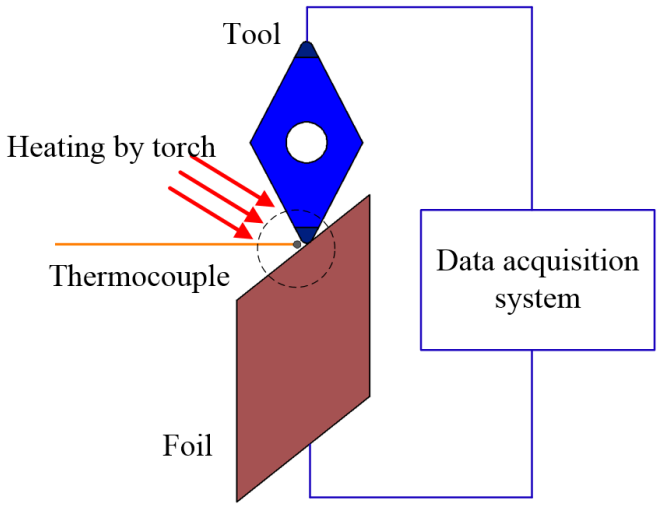

Figure 2.5 Calibration setup for tool-foil thermocouple

2.4 Method II: Embedded Thermocouple Method

2.4.1 Experimental Setup

Figure 2.6(a) shows how the thermocouple was embedded via a micro-slot on the side of the cutting tool (Fig. 2.6(b)). Figure 2.6(c) shows the embedded thermocouple, which extends through the slot to the relief surface behind the cutting edge. With such a setup, the micro-tip of the embedded thermocouple could slide on the rotating workpiece while the cutting tool was moving in the axial direction. Detailed views of this thermocouple tip in contact with the grooved machined surface are shown in Fig. 2.6(d). The grooved machined surface is along the cutting tool path right behind the cutting edge. The temperature measured at this point is the input for the inverse heat transfer method (to be discussed in Sec. 2.4.2) to predict the peak machined surface temperature close to the cutting edge.

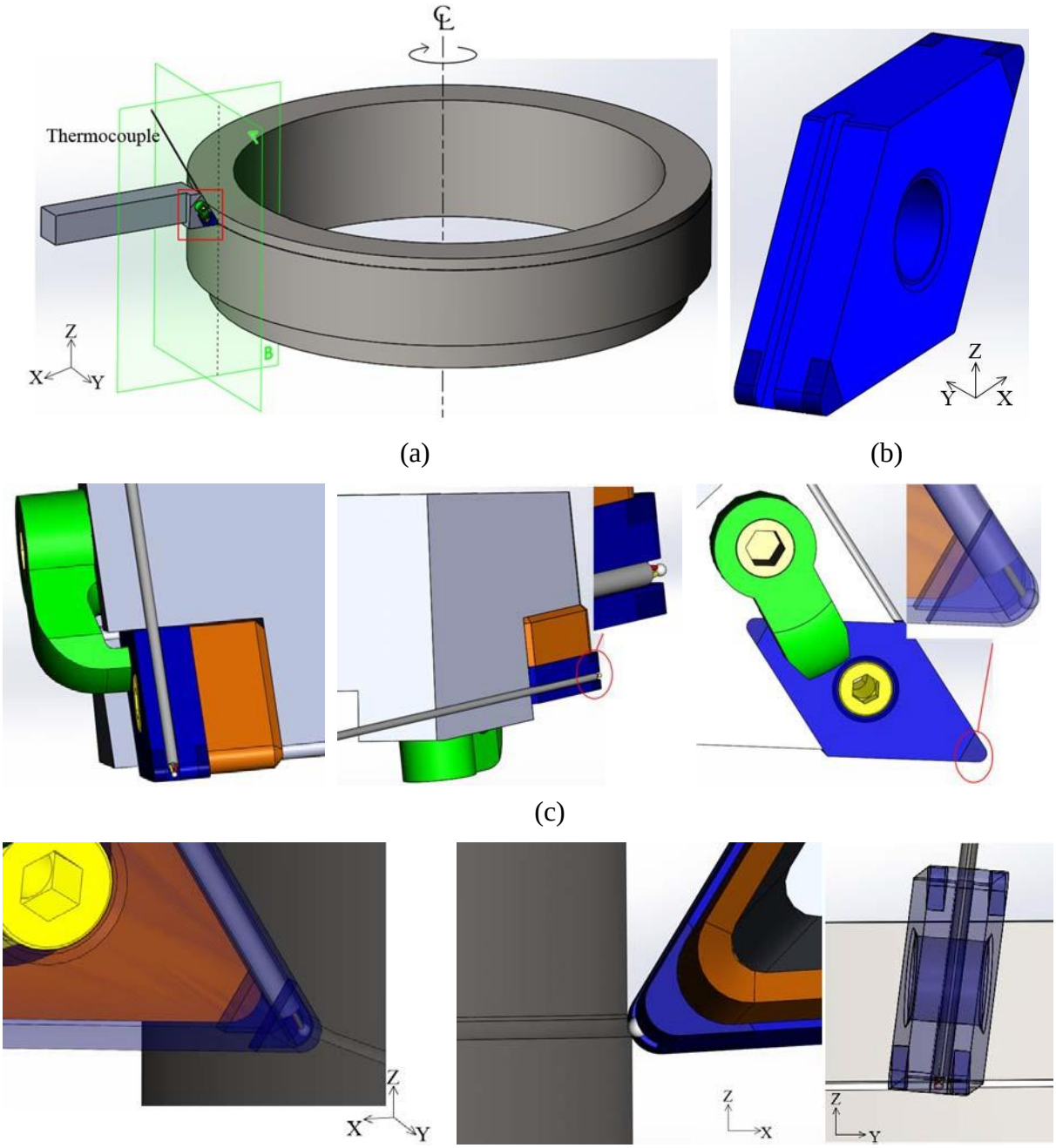

Figure 2.6 Embedded thermocouple method: (a) overall setup, (b) cutting tool with a slot grinded for thermocouple to reach the machined surface, (c) the micro-thermocouple tip in the cutting tool, and (d) the contact between the micro-thermocouple tip and grooved machined surface.

In the hard turning test described in Sec. 2.2, a 1 mm wide and 1 mm deep slot was grinded in the carbide substrate of the PCBN cutting tool, as shown in Fig. 2.7(a). A K-type thermocouple

with a 0.5 mm diameter tip was fixed inside the slot and protected by welded aluminum, as shown in Fig. 2.7(b). The thermocouple tip was placed 1.5 to 1.7 mm from the cutting tip based on the optical microscope measurement. Two orthogonal views (from the A and B planes marked in Fig. 2.6(a)) of the close-up view of the 0.5 mm diameter thermocouple tip are shown in Figs. 2.7(c) and (d).

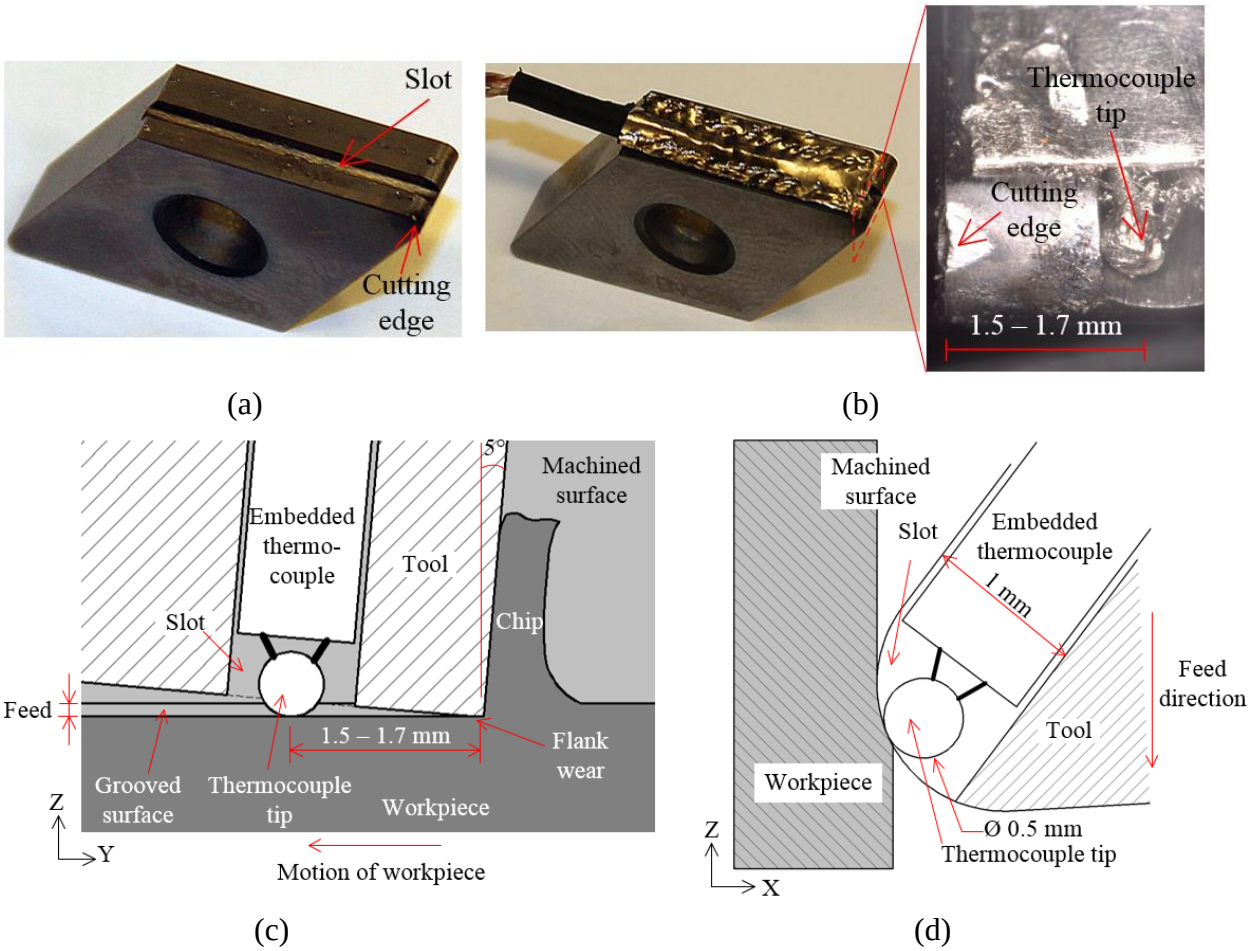

Figure 2.7 Cutting tool with embedded thermocouple: (a) slot grinded for thermocouple insertion, (b) cutting tool with thermocouple and aluminum protection, (c) interface between the embedded thermocouple tip and the machined surface, and (d) the contact between the micro-thermocouple tip and grooved machined surface.

During hard turning, the tool holder was mounted on a three-axis dynamometer (Model 9121 by Kistler) for cutting force measurement. In each cutting test, the voltage outputs from the tool-foil thermocouple, thermoelectric voltage from the embedded thermocouple in the cutting tool, and dynamometer outputs for the three cutting force components were recorded simultaneously by

a multi-channel digital oscilloscope (Model DL750 by Yokogawa) with a sampling rate of 1000 Hz.

2.4.2 FEM Thermal Model

Experimental output from Method II was the temperature measurement at 1.5 to 1.7 mm behind the cutting edge by the embedded thermocouple in the cutting tool. To convert this measurement to the machined surface temperature near the cutting edge, a thermal model and associated inverse heat transfer method were needed.

2.4.2.1 Advection Thermal Model Concept

As shown in Fig. 2.8, there are three main heat sources in hard turning: shear plane heat source, flank face frictional heat source and rake face frictional heat source. The first two sources are dominant for workpiece temperature rise. The heat source on rake face mainly determines the tool-chip interface temperature and its impact on the workpiece temperature, though limited, can be through heat conduction on the flank face. Since this study is focused on workpiece temperature in hard turning and tool-chip temperature is not of particular interest, the first two heat sources are primarily considered in the FEM thermal model, namely the shear plane heat source and the flank face frictional heat source. These two heat sources are assumed to be independent, so the total temperature rise in the workpiece is the superimposition of temperature effect from the two heat sources. The shear plane heat source is assumed to be constant during 12 repetitions under each cutting condition, while the flank face frictional heat source increases along with cumulative cutting time. Under this assumption, the shear plane heat source determines the workpiece temperature alone with a sharp tool; the flank face frictional heat source adds the temperature difference between a worn tool and a sharp tool.

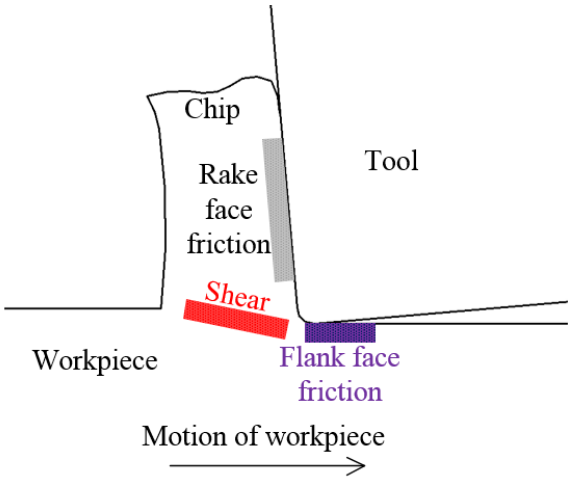

Figure 2.8 Major heat sources in hard turning.

To study the energy dissipation of the two aforementioned heat sources, in the FEM thermal model, the advection thermal model concept [17] is applied to simulate the material removal and heat transfer process, as illustrated by Step *m* to Step *m*+1 in Fig. 2.9. For the shear plane heat source, based on Dawson and Malkin's inclined moving heat source model [18], a constant surface heat flux is applied on the shear plane in each step, and the shear plane material is removed at the end of the step to simulate chip removal (and also heat partitioning). The flank face frictional heat source is simulated by a surface heat flux on the flank wear area that is moved along the cutting tool path by discrete time steps together with chip removal.

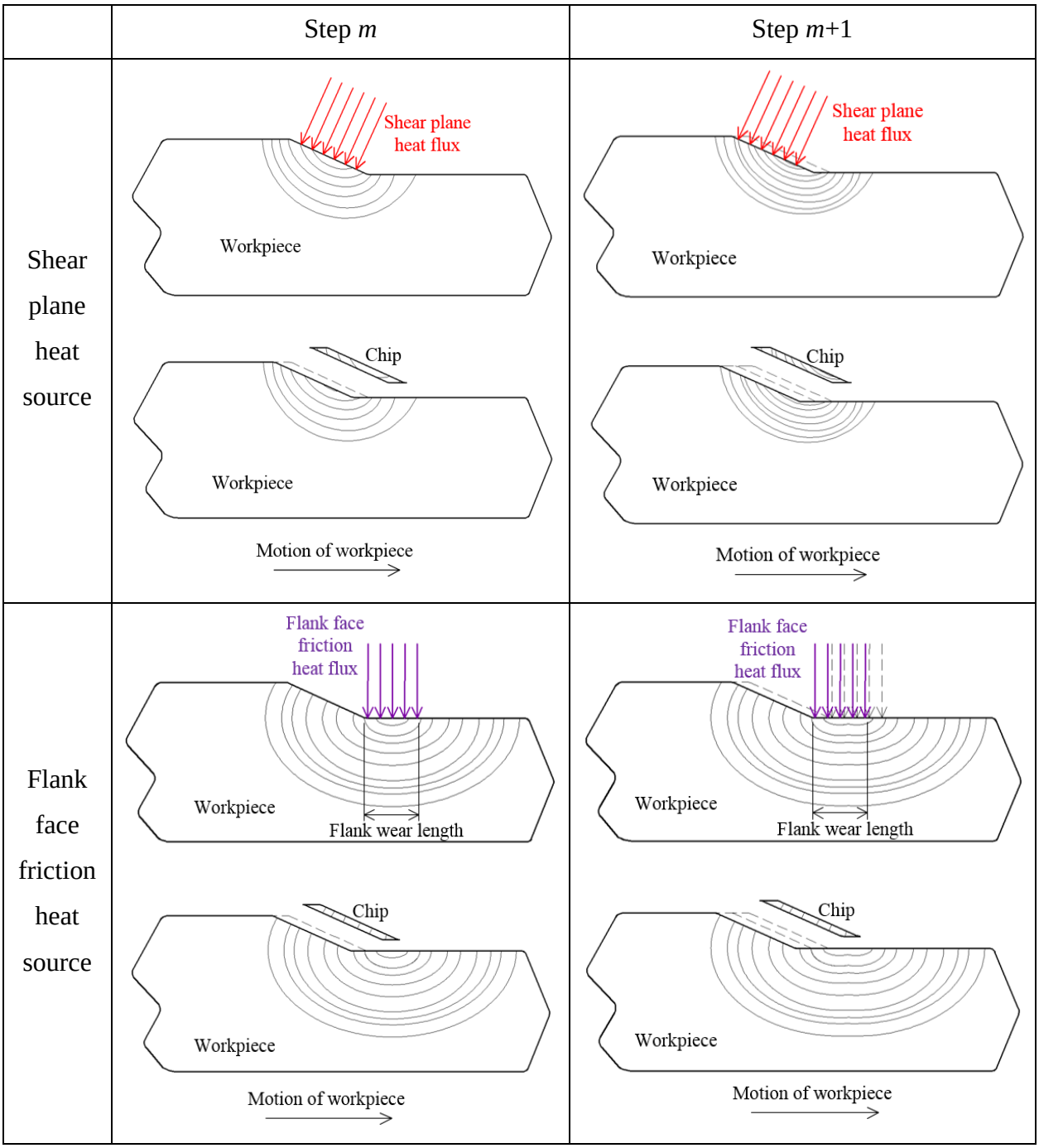

Figure 2.9 Advection thermal model for hard turning to simulate two heat sources.

As shown in Fig. 2.7(d), embedded thermocouple in the cutting tool measures temperature at the grooved machined surface behind the cutting tip. Geometry of the grooved machined surface is neglected in a two-dimensional (2D) plane strain model setup, which influences the accuracy of the inverse heat transfer problem. Also, flank wear length is not identical along the cutting edge.

Analyzing the flank wear effect in a 2D model oversimplifies the problem. Thus, in this study, a three-dimensional (3D) thermal model is developed.

2.4.2.2 3D Model Setup

The geometry of a sector of the bearing ring workpiece is utilized to develop the 3D FEM thermal model. Advection thermal model concept is applied on the geometry for material removal along the cutting tool path by discrete time steps, as shown in Fig. 2.10(a). After material removal of 3 mm length along the cutting direction, steady-state workpiece temperature is obtained in the workpiece geometry as shown in Fig. 2.10(b).

An overview of the FEM mesh of the workpiece before material removal is shown in Fig. 2.11(a). A total of 300 layers of elements with 0.01 mm layer depth along the cutting tool path, as marked in Fig. 2.11(a), will be removed in 300 discrete time steps in the simulations to reach a steady-state result. Step time is calculated using the element length along the cutting direction (0.01 mm) divided by the cutting speed (100 m/min), which is 6×10^{-6} s in this study. After 300 steps of material removal, the final mesh with the grooved machined surface, surface to be removed, and shear plane (marked by four points C, D, E, and F) between these two surfaces is shown in Fig. 2.11(b). Temperature rise due to two heat sources is simulated independently based on such model setup. The software used in this study is ABAQUS v6.11-1.

The shear plane heat source is simulated as a constant surface heat flux applied on the moving shear plane in each discrete time step. The shear plane is moving along the cutting direction during material removal and always connecting the grooved machined surface and the surface to be removed. In each time step, the moving shear plane (red surface in Fig. 2.11(c) marked by four points C', D', E', and F') is the surfaces of elements to be removed at the end of the step. It consists a layer of five elements for the 0.05 mm/rev feed and 10 elements (two layers of five elements in each) for the 0.1 mm/rev feed, as shown in the close-up view in Fig. 2.11(c). For the 0.15 mm feed, the shear plane has 15 elements, which consists of three layers of 0.05 mm high elements. Layers to be removed as chips are inclined to simulate the shear angle, also shown in Fig. 2.11(c), which is calculated based on the chip thicknesses collected from the experiments, the undeformed chip thickness and the rake angle.

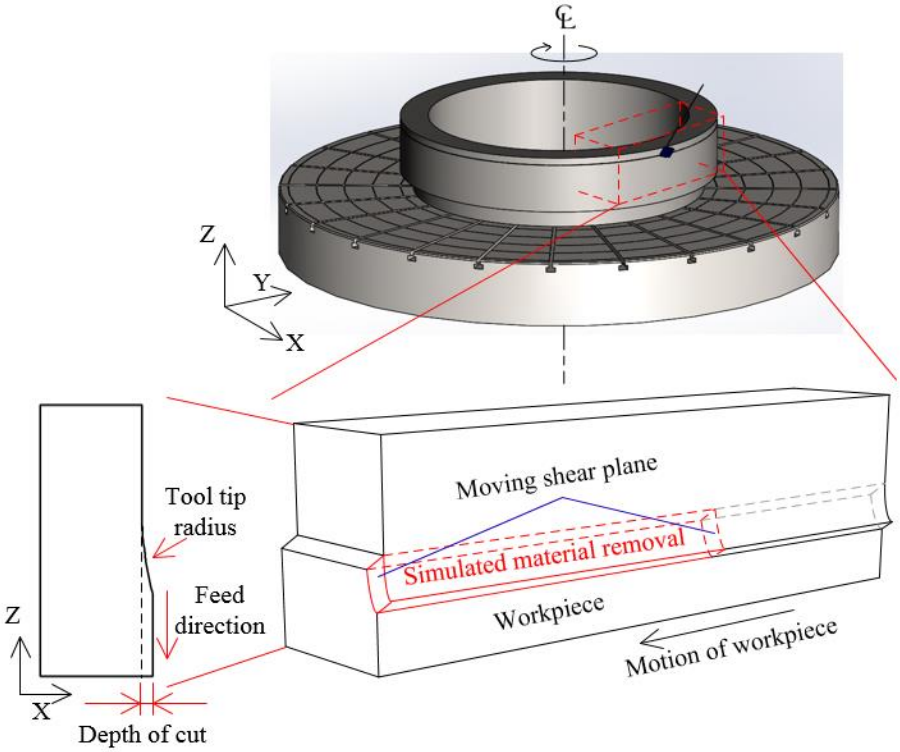

(a)

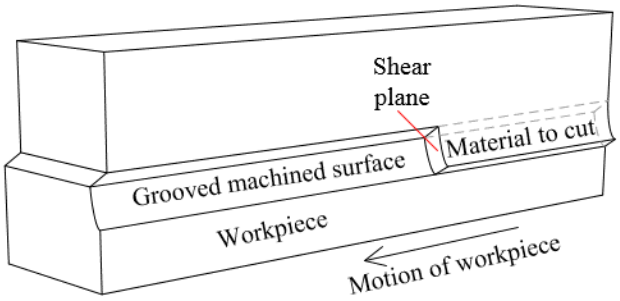

(b)

Figure 2.10 3D geometry for advection thermal model of hard turning: (a) geometry of a sector of the bearing ring workpiece and (b) geometry of the sector after material removal.

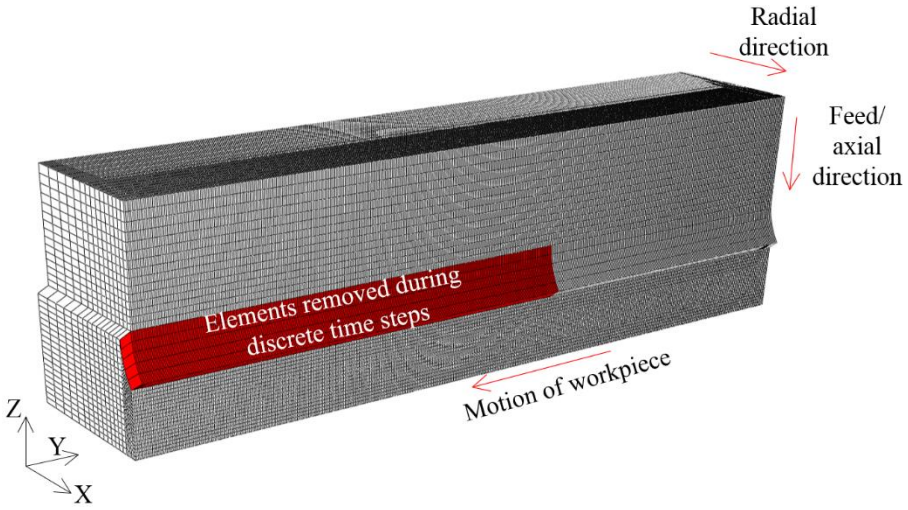

(a)

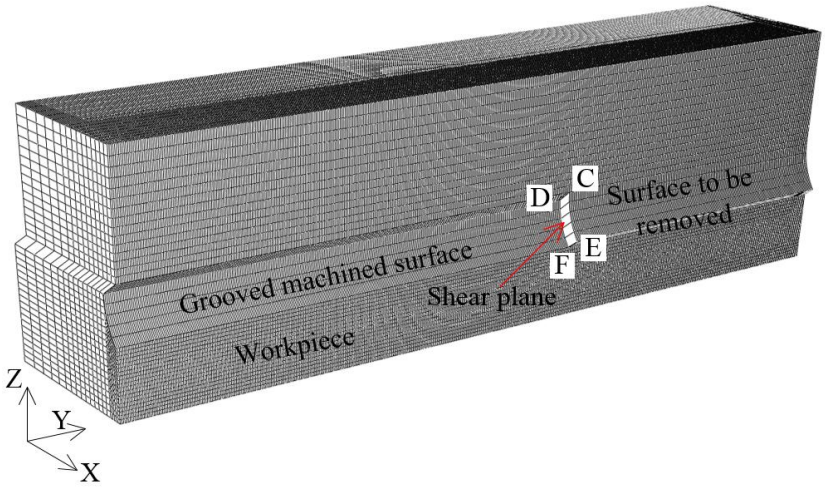

(b)

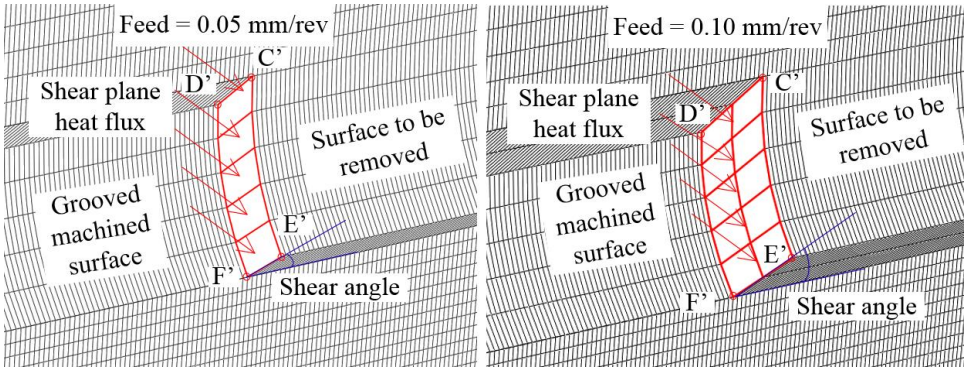

(c)

Figure 2.11 Workpiece FEM thermal model mesh to predict machined surface temperature in hard turning for the embedded thermocouple method: (a) overview of the workpiece before material removal, (b) the workpiece after material removal, and (c) close-up view of the shear plane.

The flank face frictional heat source is simulated as a surface heat flux applied on the moving flank wear area during material removal. The XZ cross-section view from the machined surface in the Y direction for the 0.1 mm/rev feed is shown in Fig. 2.12(a). The tool tip radius is the radius of the grooved machined surface and the surface to be removed (Fig. 2.2(c)). In the same cross-sectional view, the depth of cut and feed—two key hard turning process parameters—are marked in the FEM mesh. Figure 2.12(b) shows a sample optical microscope picture of the tool flank wear surface. The three points C'', D'', and F'' are in constant contact with points C', D', and F' (Fig. 2.11) on the moving shear plane during hard turning. The wear between arc C'D', marked as $V_{C'D'}$, is larger than that of arc D'F', marked as $V_{D'F'}$. This tool wear pattern has been observed consistently in turning [19]. Arc C'D'F' is the moving cutting edge during discrete time steps. The grooved machined surface behind the arc is the flank face during cutting. The area of flank face heat flux depends on the steadily increasing tool flank wear length ($V_{C'D'}$ and $V_{D'F'}$) during hard turning, as marked by arrows in Fig. 2.12(c).

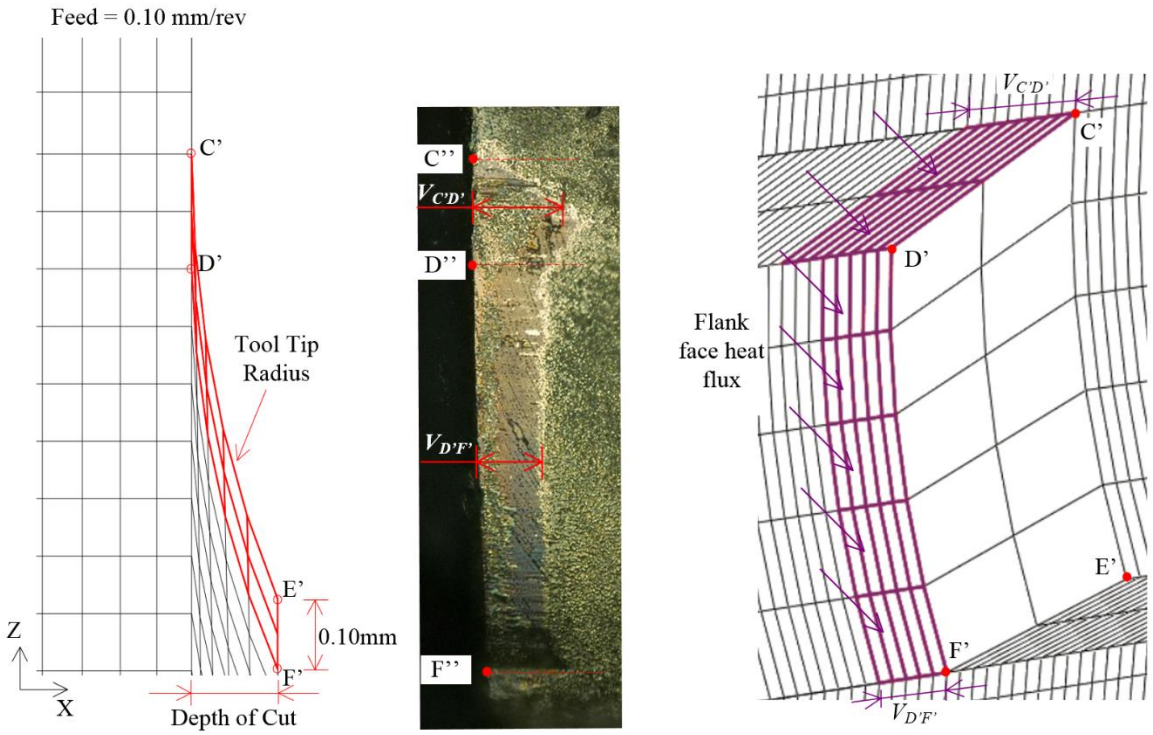

(a) (b) (c)

Figure 2.12 Flank face frictional heat source in the FEM thermal model: (a) close-up view from the tangential direction of grooved surfaces, (b) a sample optical microscope picture of the tool wear showing two levels of flank wear, and (c) close-up view of the flank face heat flux.

At the start of hard turning, the tool is sharp and $V_{C'D'} = V_{D'F'} = 0$. A preliminary study is carried out following cutting test plans described in Sec. 2.2 (36 tests in total) to determine the changing value of $V_{C'D'}$ and $V_{D'F'}$ according to cumulative cutting time. Fig. 2.13 shows $V_{C'D'}$ and $V_{D'F'}$ measured every two minutes for the 0.05, 0.1, and 0.15 mm feeds in three hard turning tests. It is assumed that the values of $V_{C'D'}$ and $V_{D'F'}$ stay constant during each two-minute cutting.

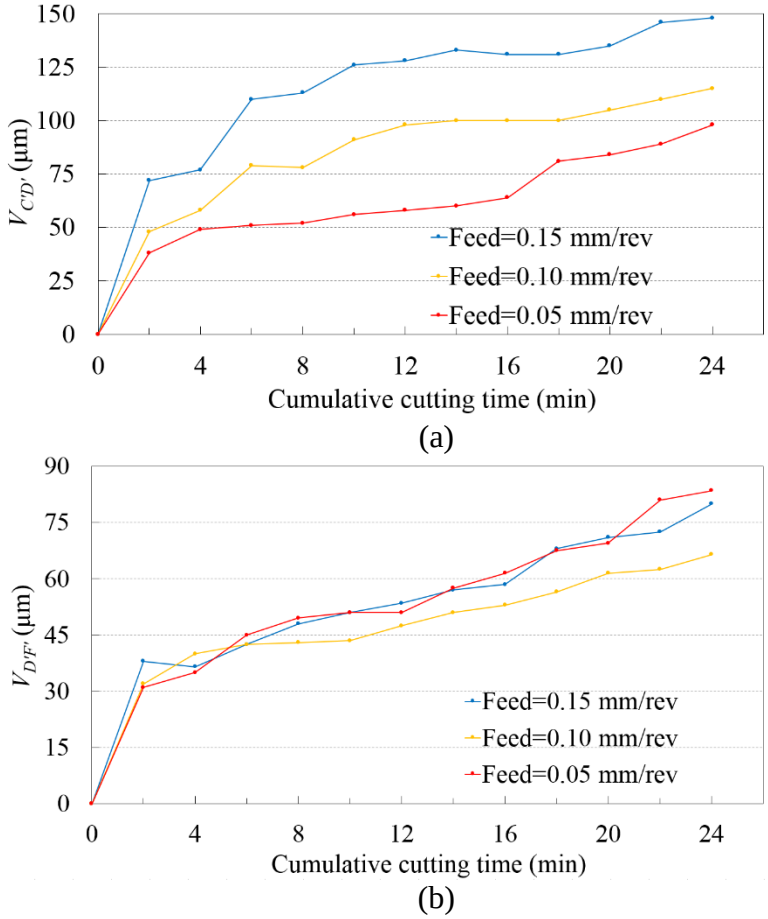

Figure 2.13 Tool flank wear vs. cumulative cutting time: (a) $V_{C'D'}$ and (b) $V_{D'F'}$.

2.4.2.3 3D Model Input

Based on the 3D thermal model setup, simulations were conducted to study steady-state temperature rise caused by the shear plane heat source and flank face frictional heat source, respectively. The surface heat flux strengths in the simulations were determined through the inverse heat transfer method.

The inverse heat transfer method utilizes the measured thermocouple temperature to estimate the peak machined surface temperature near the cutting edge, denoted as T_w. $T_w(t) = T_o + T_s + T_f(t)$, where T_o is the initial (room) temperature of the workpiece; T_s is the workpiece temperature rise contributed by the shear plane heat flux, which is a constant over time; and T_f is the workpiece temperature rise contributed by the flank face heat flux. T_f increases with time t due to the increasing flank wear and frictional heat.

To find T_s, the shear plane heat flux was applied to the shear plane area. This heat flux was determined by minimizing the objective function composed of the discrepancy between (1) the thermocouple measured temperature in the first cut (2 min) using a sharp tool without flank wear, and (2) the average temperature for five to seven nodes around the thermocouple tip location predicted by the FEM thermal model with a given shear plane heat flux. This is a single variable optimization problem to find the shear plane heat flux and T_s using the developed FEM thermal model. Based on the hard turning tests, the shear plane heat flux values were 2260, 2130 and 2090 MW/m^2 for the 0.05, 0.1 and 0.15 mm/rev feeds, respectively. Fig. 2.14(a) shows an example of the workpiece temperature distribution for hard turning with a 0.05 mm feed and only the shear plane heat flux as input.

To solve T_f, since both T_s and T_o are known, the flank face heat flux uniformly distributed in the flank wear area ($V_{C'D'}$ and $V_{D'F'}$ in Fig. 2.12) can be determined using the inverse heat transfer method. The objective function is the discrepancy between the embedded thermocouple measured temperature and the FEM thermal model predicted temperatures using a given flank face heat flux and length of flank wear zone (Fig. 2.13). Minimizing this objective function yields the flank face heat flux results. The flank face heat flux values were 132 to 734, 400 to 628, and 152 to 489 MW/m^2 for the 0.05, 0.1 and 0.15 mm/rev feeds, respectively. Fig. 2.14(b) shows an example of the workpiece temperature distribution for hard turning with a 0.05 mm feed and only the friction heat flux as input.

Both the shear plane heat flux and flank face heat flux are inputs to predict the steady-state peak machined surface temperature, which is found to occur along the intersection of cutting edge and the machined surface and is evaluated by the average of the temperatures at nodes between points C and D.

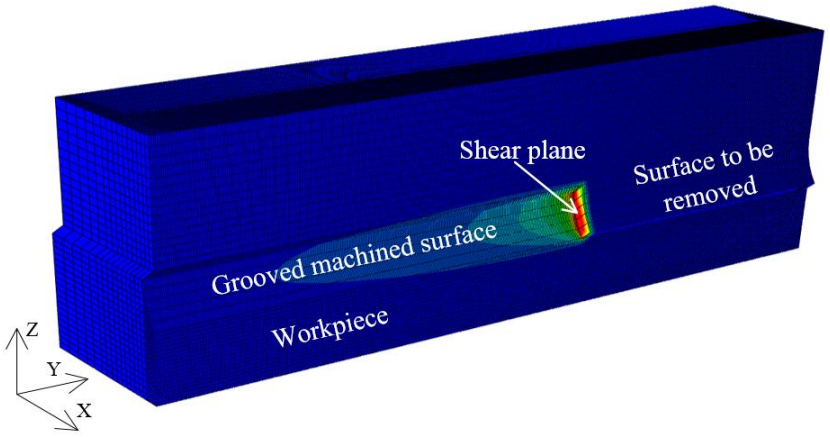

(a)

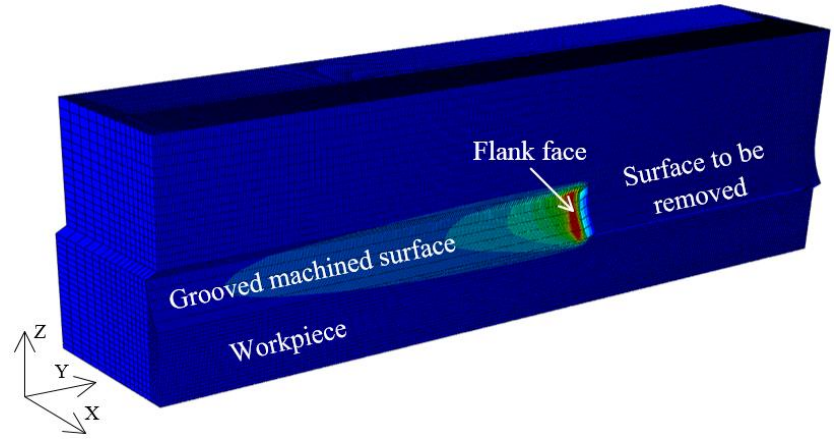

(b)

Figure 2.14 FEM thermal model predicted workpiece temperatures with: (a) shear plane heat flux only and (b) friction heat flux only.

2.5 Results and Discussion

2.5.1 The Tool-foil Thermocouple Calibration

Figure 2.15 shows the temperature-versus-voltage calibration curve in three tests based on the setup described in Sec. 2.3.2 for the tool-foil thermocouple method. The three calibration tests showed repeatable results. This calibration equation, as described in Fig. 2.15, was used to convert the measured tool-foil thermocouple voltage to temperature.

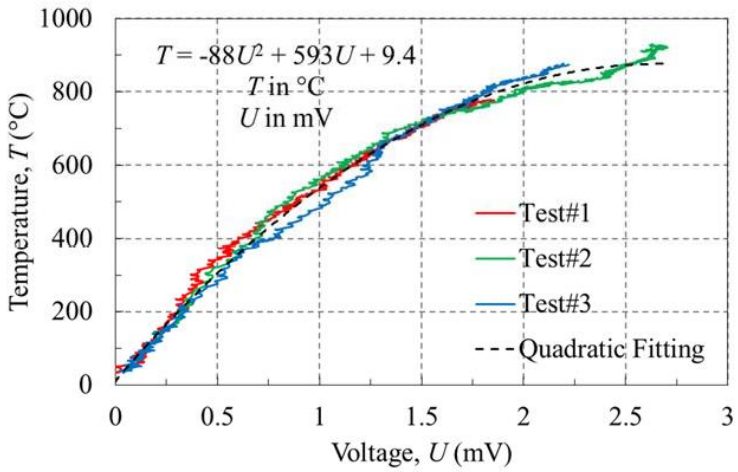

Figure 2.15 Calibration curve of the tool-foil thermocouple voltage output (*U*) and temperature (*T*).

2.5.2 Machined Surface Temperature

Figure 2.16(a) shows a set of sample results for the tangential force, embedded thermocouple temperature and tool-foil thermocouple voltage for hard turning at a 0.05 mm/rev feed rate, from 16 to 18 min, using a sharp tool from the start. There was no significant increase in the embedded thermocouple temperature or tool-foil thermocouple voltage during the 2 min (120 s) cutting time, supporting the steady-state assumption for the tool-foil thermocouple method. For the tool-foil voltage signal, notches of the tangential cutting force matched with the measured tool-foil thermocouple output voltage, as shown in Fig. 2.16(b). The peaks of tool-foil thermocouple voltage correspond to the low points (valleys) of the cutting force. The average value of these tool-foil thermocouple voltages was converted to temperature using the calibration curve in Sec. 2.5.1.

Figure 2.17 shows peak machined surface temperature measurement results for 12 tests (0 to 24 min cumulative cutting time) using the tool-foil thermocouple and embedded thermocouple methods for 0.05, 0.1 and 0.15 mm/rev feeds. The error bars show the maximum and minimum peak machined surface temperature predictions based on possible thermocouple tip locations. Both methods yield similar results using two very different approaches with an average deviation of 30°C over the 500°C to 800°C range. These results indirectly validate the accuracy of the measurement results. The general trend of higher machined surface temperatures with larger feed and longer cutting time (higher flank wear) can also be observed. The peak machined surface temperature is mainly determined by the shear plane heat source while the flank face frictional

heat source further increases the value by 50°C to 150°C with longer cutting time.

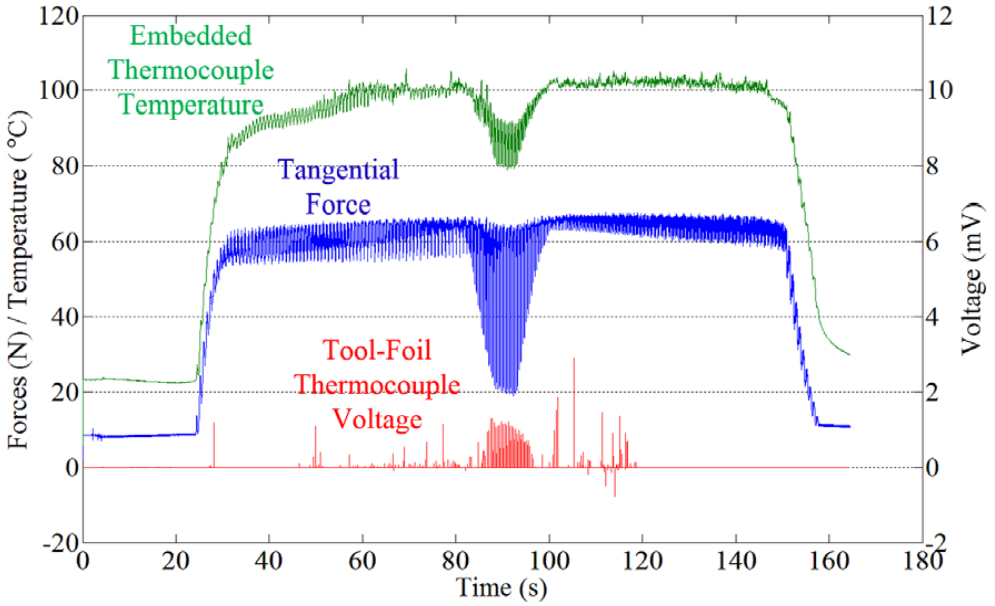

(a)

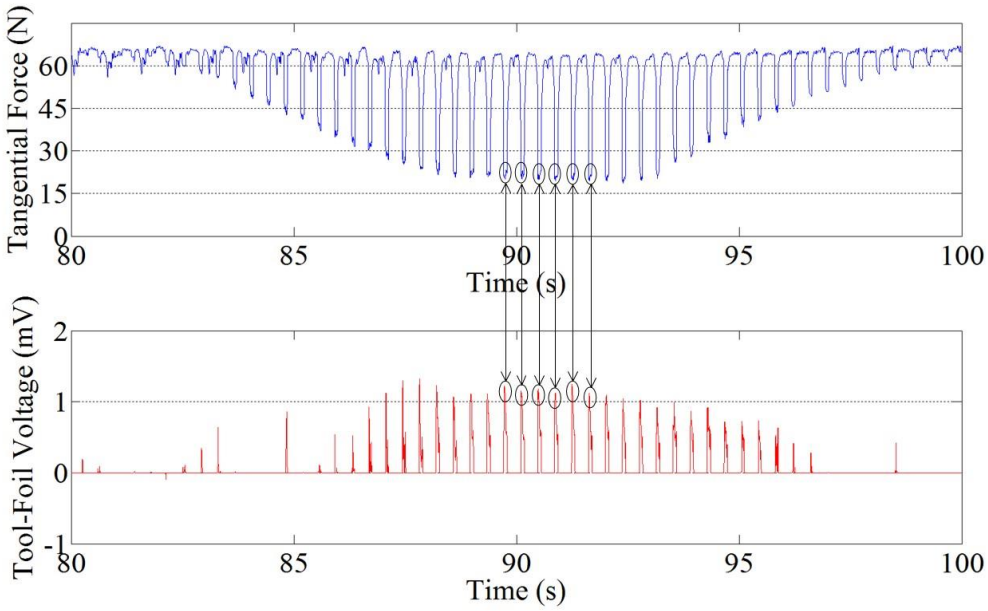

(b)

Figure 2.16 Sample hard turning test measurements at a 0.05 mm feed: (a) the measured tangential force, embedded thermocouple temperature and tool-foil thermocouple voltage and (b) the tangential cutting force and tool-foil thermocouple voltage over a 20 s duration.

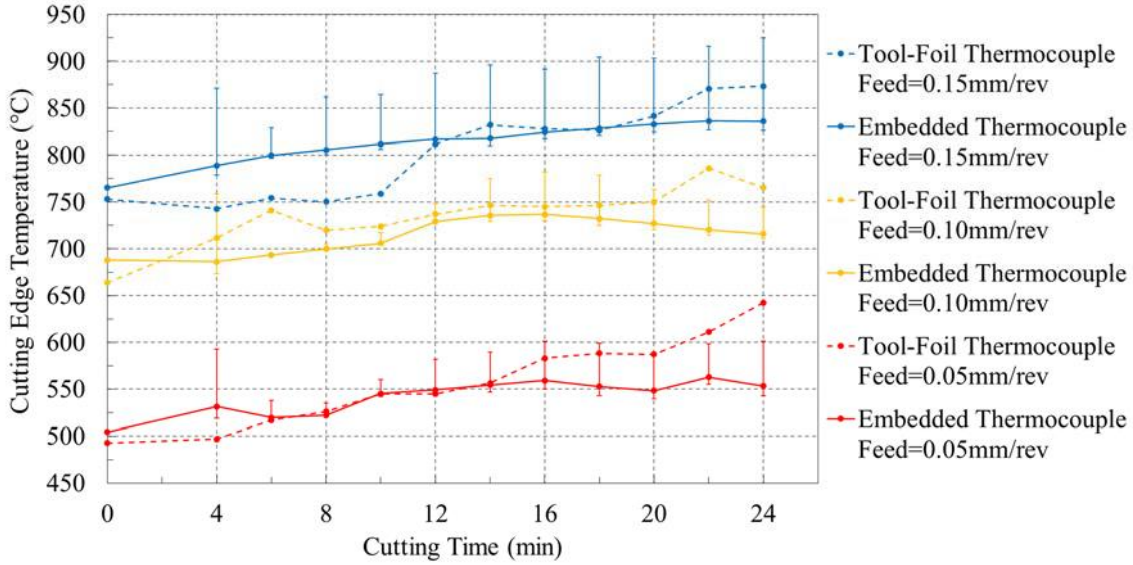

Figure 2.17 Peak machined surface temperatures measured by the tool-foil thermocouple and embedded thermocouple methods.

2.5.3 Discussions

Both methods have advantages and disadvantages. The tool-foil thermocouple method requires the preparation of the workpiece with foil and insulation layers. The measurement is based on an assumption of continuity in the temperature at the tool-workpiece interface and on the machined surface. This continuity has been observed in previous turning studies [20-22] but may not be valid under high cutting speeds and severe cutting conditions. The embedded thermocouple method's experimental setup is easier, since it requires only the modification of the PCBN cutting tool. However, this method requires FEM thermal modeling and inverse heat transfer analysis to convert the experimental measurements to the machined surface temperature. Also, it is difficult to identify the exact location of the embedded thermocouple tip and its contact with the machined surface, resulting in uncertainty regarding the machined surface temperature predictions.

To apply the developed experimental methods to predict the white layer formation during hard turning, metallurgical studies need to be conducted first to correlate the measured peak machined surface temperature to the initiation of white layer. The tool-foil thermocouple method can then be utilized to build a data base mapping the cutting condition and accumulative cutting time to a peak machined surface temperature value. Such value provides a guideline for tool life management in hard turning to prevent thermally induced white layer in hard turning.

2.6 Conclusion

The peak temperature on machined surface in hard turning occurred along the intersection of cutting edge and the machined surface based on the prediction from the embedded thermocouple method. This temperature matched with measurement from the tool-foil thermocouple method and validated both measurement methods for the peak temperature on machined surface in hard turning. The shear plane heat source was demonstrated to be more significant than the flank face frictional heat source on peak machined surface temperature. Ongoing research is being conducted to correlate the peak machined surface temperature to the white layer formation to determine the tool life in hard turning.

References

[1] A. Ramesh, S.N. Melkote, L.F. Allard, L. Riester, T.R. Watkins, Analysis of white layers formed in hard turning of AISI 52100 steel, Materials Science and Engineering 390 (1) (2005) 88-97.

[2] Y.B. Guo, A.W. Warren, F. Hashimoto, The basic relationships between residual stress, white layer, and fatigue life of hard turned and grinded surfaces in rolling contact, CIRP Journal of Manufacturing Science and Technology 2 (2) (2010) 129-134.

[3] Y.K. Chou, C.J. Evans, White layers and thermal modeling of hard turned surfaces, International Journal of Machine Tools and Manufacture 39 (12) (1999) 1863-1881.

[4] Y.K. Chou, H. Song, Thermal modeling for white layer predictions in finish hard turning, International Journal of Machine Tools and Manufacture 45 (4) (2005) 481-495.

[5] Y.B. Guo, G.M. Janowski, Microstructural characterization of white layers by hard turning and grinding, Trans. NAMRI/SME 32 (2004) 367-374.

[6] T. Ueda, M. Al Huda, K. Yamada, K. Nakayama, H. Kudo, Temperature measurement of CBN tool in turning of high hardness steel, CIRP Annals-Manufacturing Technology 48 (1) (1999) 63-66.

[7] E.G. Ng, D.K. Aspinwall, D. Brazil, J. Monaghan, Modelling of temperature and forces when orthogonally machining hardened steel, International Journal of Machine Tools and Manufacture 39 (6) (1999) 885-903.

[8] M. Al Huda, K. Yamada, A. Hosokawa, T. Ueda, Investigation of temperature at tool-chip interface in turning using two-color pyrometer, Journal of Manufacturing Science and Engineering 124 (2) (2002) 200-207.

[9] D.A. Stephenson, Tool-work thermocouple temperature measurements - theory and implementation issues, Journal of Engineering for Industry 115 (4) (1993) 432-437.

[10] C.E. Leshock, Y.C. Shin, Investigation on cutting temperature in turning by a tool-work thermocouple technique, Journal of Manufacturing Science and Engineering 119 (4A) (1997) 502-508.

[11] A.U. Anagonye, D.A. Stephenson, Modeling cutting temperatures for turning inserts with various tool geometries and materials, Journal of Manufacturing Science and Engineering 124 (3) (2002) 544-552.

[12] M. Bono, J. Ni, A method for measuring the temperature distribution along the cutting edges of a drill, Journal of Manufacturing Science and Engineering 124 (4) (2002) 921-923.

[13] T.I. El-Wardany, E. Mohammed, M.A. El-Bestawi, Cutting temperature of ceramic tools in high speed machining of difficult-to-cut materials, International Journal of Machine Tools and Manufacture 36 (5) (1996) 611-634.

[14] X.J. Ren, Q.X. Yang, R.D. James, L. Wang, Cutting temperatures in hard turning chromium hardfacings with PCBN tooling, Journal of Materials Processing Technology 147 (1) (2004) 38-44.

[15] J. L. Battaglia, L. Puigsegur, O. Cahuc, Estimated temperature on a machined surface using an inverse approach, Experimental Heat Transfer 18 (1) (2005) 13-32.

[16] M.A. Davies, T. Ueda, R. M'saoubi, B. Mullany, A.L. Cooke, On the measurement of temperature in material removal processes, CIRP Annals-Manufacturing Technology 56 (2) (2007) 581-604.

[17] L. Chen, J. Yang, A.J. Shih, B. Tai, Investigation of finite element thermal models for workpiece temperature in cylinder boring, ASME MSEC, Charlotte, North Carolina, USA, June 8-12, 2015.

[18] P.R. Dawson, S. Malkin, Inclined moving heat source model for calculating metal cutting temperatures, Journal of Engineering for Industry 106 (3) (1984) 179-186.

[19] S. Kalpakjian, S. Schmid, Manufacturing Engineering and Technology, Seventh Ed., Pearson Education, Upper Saddle River, New Jersey, 2014.

[20] R. Komanduri, Z.B. Hou, Thermal modeling of the metal cutting process—Part III: temperature rise distribution due to the combined effects of shear plane heat source and the tool-chip interface frictional heat source, International Journal of Mechanical Sciences 43 (1) (2001) 89-107.

[21] W. Grzesik, M. Bartoszuk, P. Nieslony, Finite element modelling of temperature distribution in the cutting zone in turning processes with differently coated tools, Journal of Materials Processing Technology 164 (2005) 1204-1211.

[22] A.G. Mamalis, J. Kundrák, A. Markopoulos, D.E. Manolakos, On the finite element modelling of high speed hard turning, The International Journal of Advanced Manufacturing Technology 38 (5) (2008) 441-446.

CHAPTER 3
EXPERIMENTAL STUDY AND FINITE ELEMENT MODELING OF WORKPIECE TEMPERATURE IN FINISH CYLINDER BORING

3.1 Introduction

Boring is a machining process to enlarge a hole to achieve better dimensional and geometrical tolerances and finer surface finish. Cylinder boring is a key process for engine block machining in automotive powertrain production. Accuracy of cylinder boring process is defined by the cylindricity, which is a geometric tolerance of a surface of revolution where all points are to be equidistant from a common axis. The cylindricity tolerance specifies a zone bounded by two concentric cylinders within which the surface must lie [1]. Lack of cylindricity in a cylinder bore leads to oil consumption, piston ring wear, engine power and other engine performance issues [2-6]. Cylinder boring includes the rough boring and finish boring processes. Finish boring is typically the last pass using a single-point tool and determines the cylinder bore shape before honing to generate the final size and surface finish [2].

In boring, the cylindricity error is induced from both mechanical and thermal error sources [2-6]. Mechanical error sources include the elastic deformation due to cutting forces, fixture and clamping loads on workpiece, boring tool deflection, and machine tool error. Thermal error is due to the thermal expansion of both workpiece and boring tool.

Research was conducted to evaluate the cylindricity error resulting from both mechanical and thermal error sources. Subramani et al. [2] predicted the cylindricity in rough boring of cast iron engine block using the finite element method (FEM) incorporating a mechanistic force model (for cutting force induced elastic deformation) and an analytical thermal model (for thermal expansion of the workpiece). Thermal expansion was found to be a significant part leading to cylindricity error, more dominant than the cutting force induced elastic deformation in some cases. Kakade and Chow [3] reported that thermal distortions were approximately an order of magnitude

larger than mechanical distortions, contributing to more than 90% of the total cylindricity error. Experimental study by Tang et al. [4, 5] also concluded that during the dry boring of cast iron, the deformation caused by thermal expansion dominated about 66% to 87% of the total deformation. In Zheng et al. [6], boring tests on aluminum liners under both dry and wet conditions also showed thermal deformations dominated (90% vs. 10% for dry machining and 85% vs. 15% for wet machining). In addition to cylindricity error, high workpiece temperature can also degrade the surface integrity due to thermal softening and temperature-induced tensile residual stress, which can affect the fatigue life of the workpiece [7-10]. Prediction of the workpiece temperature in finish boring, the topic of this research, is important to estimate the thermal distortion and dimensional and geometrical accuracy of a cylinder.

Experimental, analytical and numerical methods have been utilized to study the workpiece temperature in boring.

Experimentally, the infrared and embedded thermocouples have been applied to measure workpiece temperature in boring [4-6, 11]. The experimentally measured temperature at a single point is used as the input for the inverse heat transfer problem to determine the heat flux in thermal models. The experimental approaches, in general, lack the spatial and temporal resolution to measure the workpiece temperature which is rapidly changing (in the time domain) and has a large gradient on the machined surface (in the spatial domain).

Analytically, thermal models were developed to study workpiece temperature in boring [6, 11]. Subramani et al. [11] developed an analytical model to predict the boring workpiece temperature. The interface between tool and workpiece was considered to be a helically moving volumetric heat source, which was determined by the inverse heat transfer method. The workpiece temperature was solved using integral transforms. Zheng et al. [6] simplified the problem to a one-dimensional thermal model by neglecting the radial and circumferential temperature gradients and applied the integral transforms to find the temperature in a thin aluminum workpiece. Analytical models are limited to simple, cylindrical geometry and often oversimplify the temperature field. For an engine block with complex geometry, the FEM based numerical method has been developed.

FEM can model the complex 3D geometry for detailed analysis of workpiece temperature [12-16] and has been applied to predict the workpiece temperature in rough boring [3,4]. However, simulating finish boring of a large diameter cylinder with a small depth of cut is still a technical

challenge. For example, a thin layer of 0.4 to 1.0 mm is typically removed in finish boring of the 80 to 100 mm diameter engine block cylinder bore. A fine FEM mesh for such large diameter and small depth of cut will require extensive computing resources to model the large temperature gradient near the heat source close to the cutting point. The complex overall workpiece geometry, e.g. the water jacket and clamping bolt holes in the engine block, also demands fine FEM mesh and extensive computational capacity. In this chapter, four FEM techniques are developed to address this technical challenge for finish boring thermal modeling.

Several FEM thermal models for workpiece temperature in machining has been developed. Dawson and Malkin [16] presented an inclined heat source model using a band of heat source in the shear plane and assuming that all shear plane heat was conducted to the workpiece. Based on the inclined heat source assumption, Bono and Ni [17] developed the 2D advection FEM model to predict the drill-workpiece heat partition and workpiece temperature distribution in drilling. The heat partition on the shear plane was achieved by simulating the material removal process, making the advection model more accurate in predicting the workpiece temperature. Kakade and Chow [3] applied 3D FEM with single nodal heat source, constant heat partition ratio, and layer-by-layer element removal to study the workpiece temperature and cylinder bore distortion. Tai et al. [18] developed a heat carrier model to transfer heat from a drill to the workpiece in minimum quantity lubrication (MQL) deep-hole drilling. Heat carriers acted as a moving heat sources to conduct heat into the workpiece. Tang et al. [5] and Watts [19] investigated the workpiece temperature using a moving circumferential ring heat source for boring. The aforementioned four modelling concepts are adopted and evaluated in this chapter and compared with experimental measurements to investigate the accuracy and computational efficiency in predicting workpiece temperature in finish boring.

In this chapter, four FEM thermal models for boring temperature modeling are first introduced. Finish boring experiments are then presented. The FEM simulation results and comparison with experimental measurements are discussed.

3.2 Thermal Models for Boring Workpiece Temperature

An overview of the four FEM thermal models for boring, namely Model #1 Advection model, Model #2 Surface heat model, Model #3 Heat carrier model, and Model #4 Ring heat model, are shown in Fig. 3.1.

Model #1, the advection model [17], simulates heat transfer along with material removal from step n to step n+1. The heat source is a surface heat flux loaded on the shear plane, which magnitude is determined through the inverse heat transfer method. An element is removed at the end of each time step to simulate chip (and heat) removal. The time increment for removing elements is determined by the element size and cutting speed. The heat flux is applied on the up-front 3D element surface against the cutting edge, as shown in Fig. 3.1. The FEM mesh size is determined by the depth of cut and feed per revolution to match the material removal.

Model #2, the surface heat model, is modified from the single nodal heat model developed by Kakade and Chow [3] by applying the surface heat flux on the element surface. The depth of cut in finish boring is small (in comparison to the bore diameter) and can be seen as negligible. The machined workpiece geometry is used in this model. However, since Models #2 does not have layers of elements to be removed as in Model #1, the heat partition needs to be incorporated to estimate the heat that flows into the workpiece. In this study, the heat partition ratio is determined experimentally using the inverse heat transfer method by minimizing the discrepancy between model prediction and experimental measurement using the embedded thermocouple method.

Model #3, the heat carrier model, regards the tool as an isothermal heat carrier to conduct a constant surface heat flux into the workpiece. The heat carrier has the given tool motion (speed and path). The heat capacity of the thermal carrier is set to be low to ensure the heat flows to the workpiece [18]. Similar to Model #2, this model also uses the final shape of workpiece for meshing without considering element removal.

Model #4, the ring heat model, has the heat flux concentrated to a ring-shape band along the tool path in one revolution [19]. This ring heat flux moves along the axial direction by feed per revolution in each step. For every revolution of the tool, a ring-shape heat flux is applied on the machined surface of one layer of elements. The time step is longer as no detailed element-by-element movement is needed.

Model	Step n	Step n+1	3D Models
Model #1: Advection model	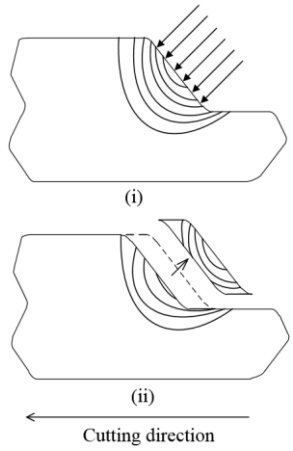	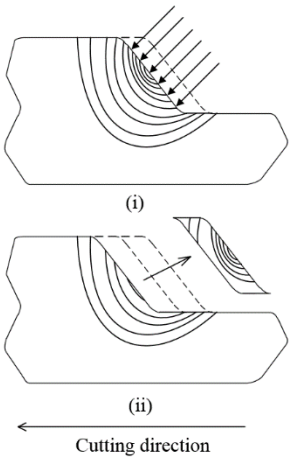	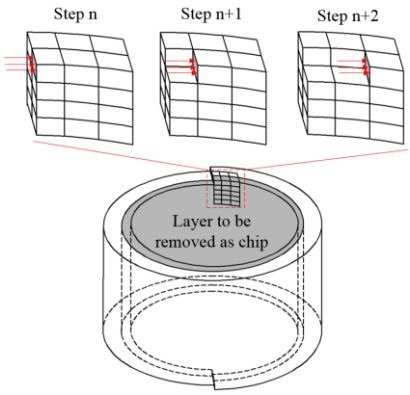
Model #2: Surface heat model	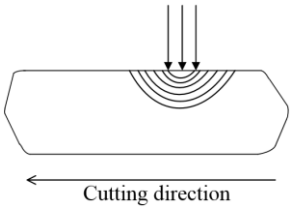	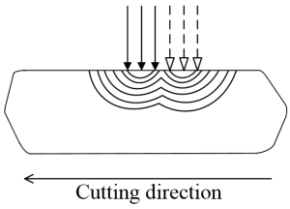	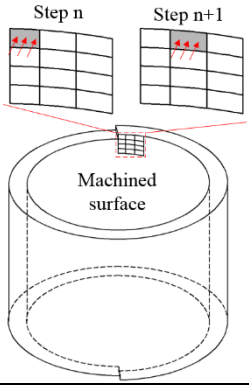
Model #3: Heat carrier model	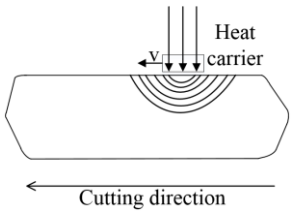	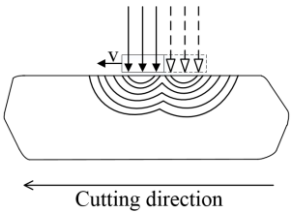	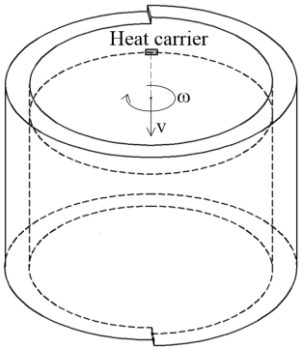
Model #4: Ring heat model	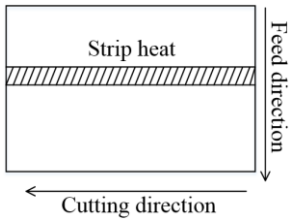	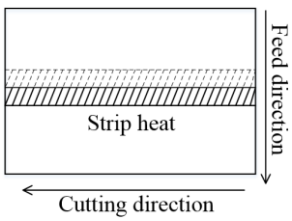	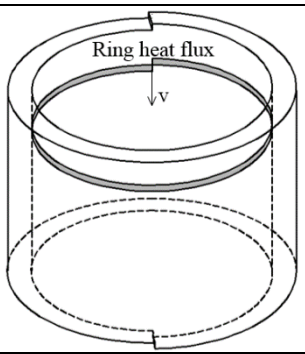

Figure 3.1 Four FEM thermal models for boring.

3.3 Experimental Setup for Finish Boring Tests

Finish boring experiments, as shown in Fig. 3.2, were conducted on a horizontal machining center (HMC-400EP by Cincinnati Machine, Cincinnati, OH). The workpiece in the tests was the grey cast iron liner with 79.2 mm inner diameter, 97.0 mm outer diameter and 41.6 mm length. The work-material had a density of 7200 kg/m^3, specific heat of 544 J/kg·K, thermal conductivity of 45.2 W/m·K, and Brinell hardness of 235. The workpiece was clamped by a two-piece three-jaw aluminum fixture, as shown in Fig. 3.2, with two clamping bolts. Two load cells were used to measure the clamping forces. The fixture was attached to a pallet with a piezoelectric dynamometer (Model 9273 by Kistler, Winterthur, Switzerland) in between to measure three cutting forces (F_x, F_y, and F_z) and axial torque (M_z), as marked in Fig. 3.2, during boring. A single point boring bar (Model 312.611 by Big Kaiser, Hoffman Estates, IL) and a polycrystalline cubic boron nitride (PCBN) insert (Kennametal TPGW2151EC) were used for dry finish boring with 0.4 mm radial depth of cut, 0.15 mm/rev feed rate, and 794 m/min cutting speed.

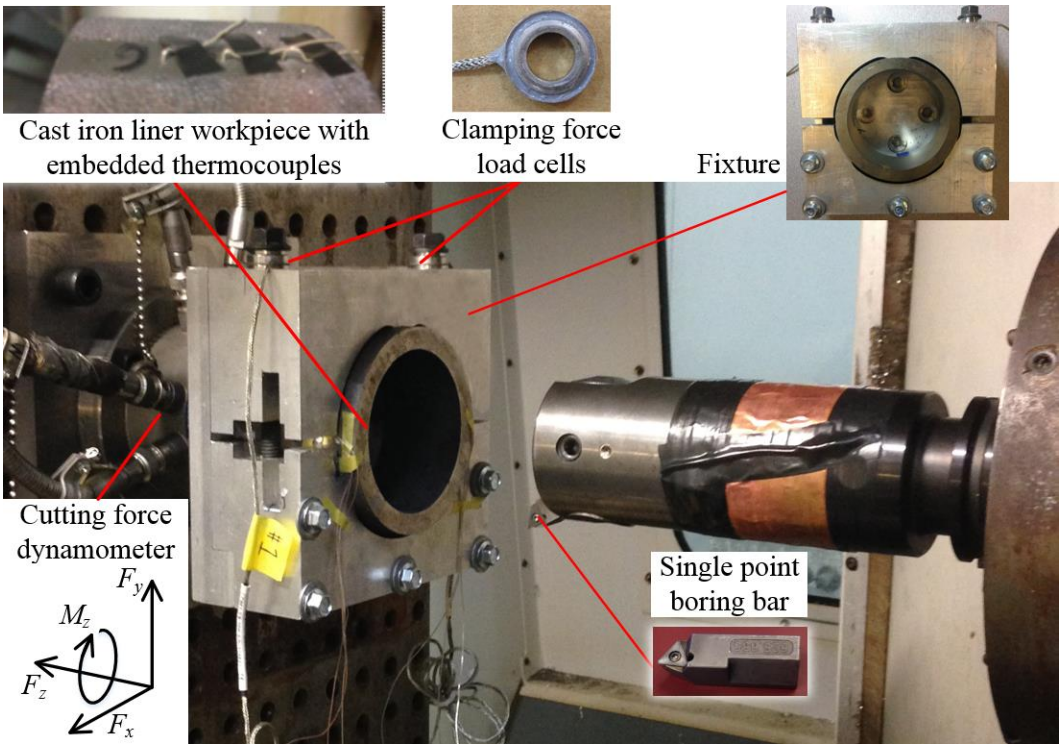

Figure 3.2 Experimental setup for finish boring experiment with embedded thermocouples.

For workpiece temperature measurement, two methods, the embedded thermocouple in the workpiece and tool-foil thermocouple method [20], were utilized in two separate boring tests.

3.3.1 Embedded Thermocouples in Workpiece

Six blind holes, three on each side, were pre-drilled on the workpiece for thermocouple insertion, as shown in Fig. 3.3(a). Six thermocouples (Type 5TC-TT-K-24-36 by Omega, Norwalk, CT), denoted as TC1 to TC6, were fixed inside these holes with high conductivity thermal paste at the tip. During cutting, the thermocouple voltage outputs were recorded by a data acquisition module (Model OMB-DAQ-2408 by Omega Engineering, Norwalk, CT) with sampling frequency of 20 Hz. After boring, the machined workpiece was sectioned into two pieces, as shown in Fig. 3.3(b), to measure the distance between the thermocouple hole bottom and the machined surface. Results of the distance are listed in Table 3.1 for TC1 to TC6.

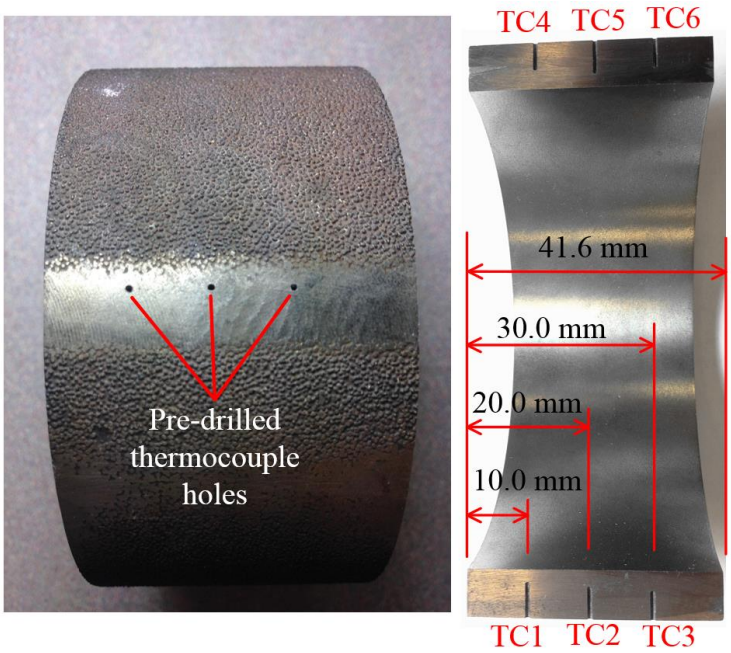

(a) (b)

Figure 3.3 Six embedded thermocouples in the workpiece: (a) pre-drilled holes for thermocouple insertion and (b) cross-sectional view of the workpiece after cutting.

Table 3.1 Distance between thermocouple hole bottom and machined surface

Thermocouple Number	Distance (mm)
TC1	2.0
TC2	2.5
TC3	3.0
TC4	3.1
TC5	2.1
TC6	2.6

3.3.2 Tool-Foil Thermocouple Method

The tool-foil thermocouple method [20] was applied to measure the finish boring workpiece surface temperature. As shown in Fig. 3.4(a), the cylindrical workpiece was sectioned to the top and bottom rings. These two rings were positioned using three dowel pins and fixed by three clamping bolts. Four shallow slots were ground on the contact surfaces between these two rings. These slots formed two grooves after clamping two rings. In each groove was a 0.05 mm thick copper foil sandwiched between two 0.25 mm thick insulation layers made of polyester shim stock, which electrically insulated the copper foil from the workpiece. When the rotating cutting tool moved along the axial feed direction, it cut and contacted the embedded copper foil a few times and a thermocouple junction was formed between the PCBN tool tip and the foil, as shown in Fig. 3.4(b). By measuring the potential difference between the metal foil and tool, temperature at the tool-foil interface on the machined surface could be measured by using the tool temperature-voltage calibration data.

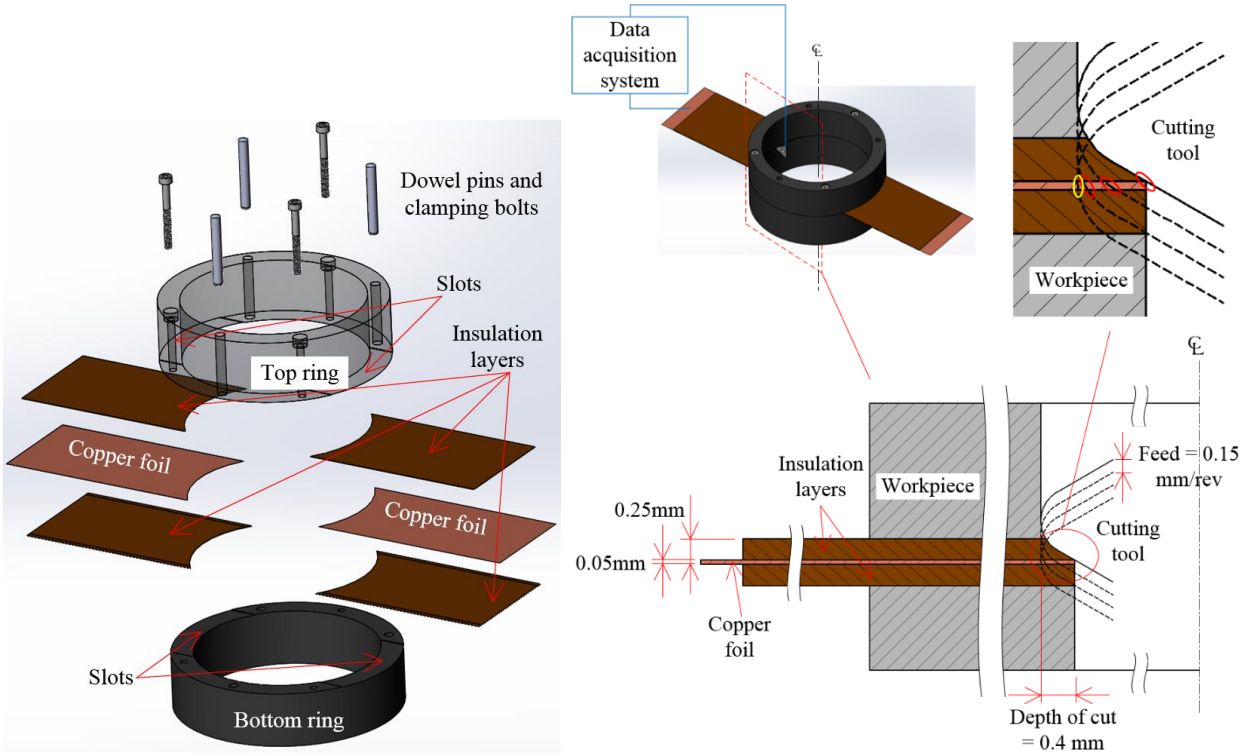

(a) (b)

Figure 3.4 Tool-foil thermocouple method for finish boring: (a) exploded view of workpiece and (b) close-up cross sectional view of tool-foil contact during boring.

The experimental setup for tool-foil thermocouple method implementation is shown in Fig. 3.5. The workpiece with embedded foil was clamped in the fixture with wires collecting voltage signal from two pieces of copper foil. A layer of vinyl electrical insulation tape was wrapped around the boring bar and copper foil was wrapped outside the tape. The tool was connected to the wrapped copper foil through another piece of foil clamped underneath the tool. A copper wire brush was preloaded on this foil wrapped around the boring bar to transmit the voltage signal to the data acquisition system (Model DL750 multi-channel digital oscilloscope by Yokogawa, Tokyo, Japan) during boring. The wire brush and foil wrapped on the boring bar were of the same material to ensure the heat generated by brush friction would not result in extra voltage in the measurement. The sampling rate was 5000 Hz.

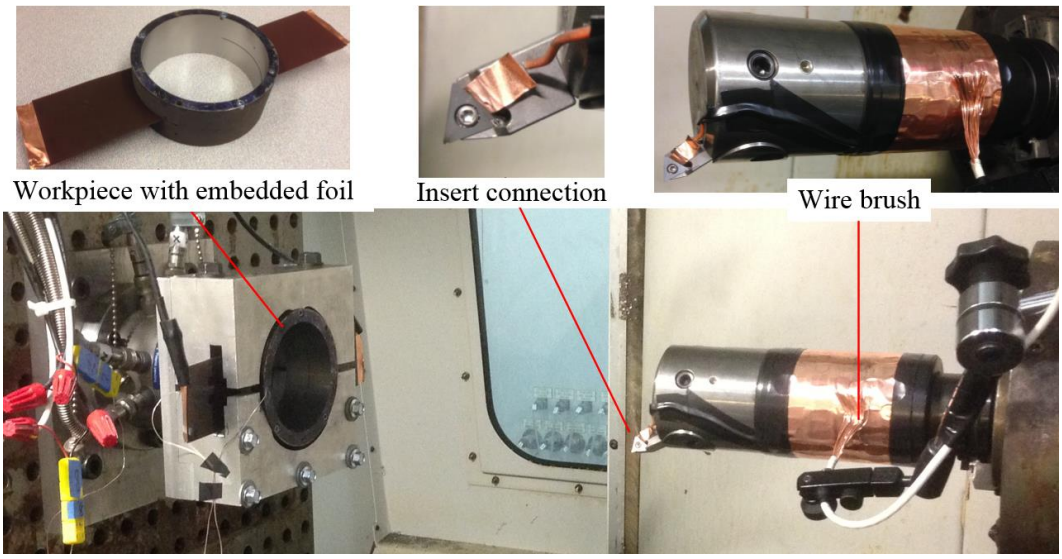

Figure 3.5 Experimental setup for tool-foil thermocouple measurement.

The tool-foil voltage-temperature calibration test setup is shown in Fig. 3.6. The copper foil and PCBN cutting tool in contact were heated by a butane torch. A K-type thermocouple was placed at the tool-foil interface. While heating, the tool-foil voltage was recorded together with a thermocouple measurement to create the voltage vs. temperature calibration data.

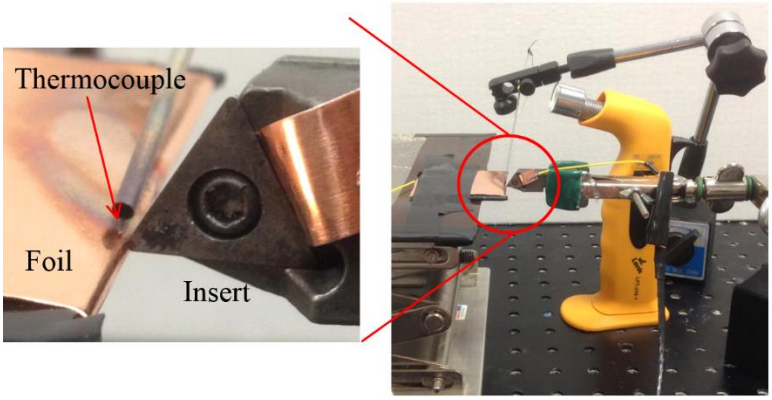

Figure 3.6 Experimental setup for tool-foil thermocouple calibration.

3.4 FEM Thermal Models

3.4.1 FEM Mesh Setup

The cylindrical geometry of the liner workpiece was used in FEM thermal models. The workpiece could be meshed with adjacent elements orthogonal to each other, as shown in Fig. 3.7(a). This type of mesh was ideal for the ring heat source (Model #4). However, for Models #1 to #3, the heat sources and heat carrier would move along a circumferential cutting path instead of following the actual spiral tool path. Therefore, the spiral mesh shown in Fig. 3.7(b) that lined up with the tool trajectory was adopted. As marked in Fig. 3.7(b), two small steps existed at the start and end of the spiral mesh in order to form a cylindrical structure.

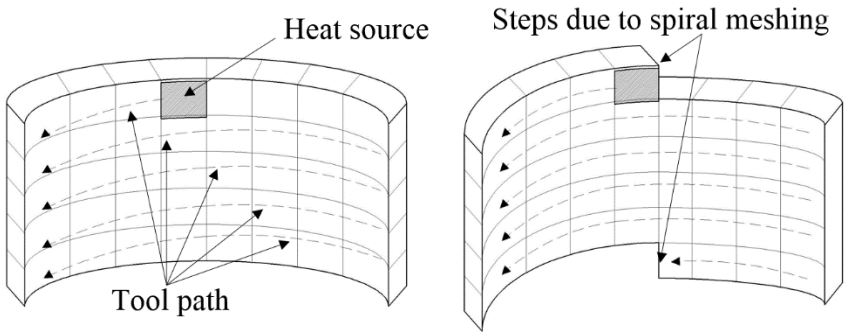

Figure 3.7 (a) Structured mesh and (b) spiral mesh based on tool motion.

Figure 3.8 shows the spiral mesh used in this study using ABAQUS v6.11-1 FEM software. The model contained 277 layers with the element height (layer thickness) of 0.15 mm, the same as the feed per revolution. Along the circumference, each revolution contained 360 elements, which made the element size about 0.7 mm along the circumferential direction. In Models #1, #2, and #4, a solid continuum element type DC3D8, a 3D 8-noded linear brick element for heat transfer analysis in ABAQUS, was selected. In Model #3, the 3D 8-noded brick element C3D8T for coupled thermal-mechanical analysis was used. The contact surface between the workpiece and the heat carrier was defined with a contact thermal resistance that allowed continuous heat conduction across the boundary.

The mesh size along the radial direction is illustrated in Fig. 3.8. In Model #1, the thickness of inner layer to be removed was 0.4 mm, same as the radial depth of cut. This inner layer was

removed element-by-element after each time step. This layer was not included in Models #2 to #4 as these methods utilized the machined workpiece geometry. For the 8.5 mm radial thickness of the machined workpiece, 11 layers of elements were generated. The innermost layer was 0.2 mm thick and thickness of the following layers further away from the machined surface gradually increased with a constant bias of 1.25. This mesh size was determined using the convergence test to balance the computational cost and accuracy of workpiece temperature.

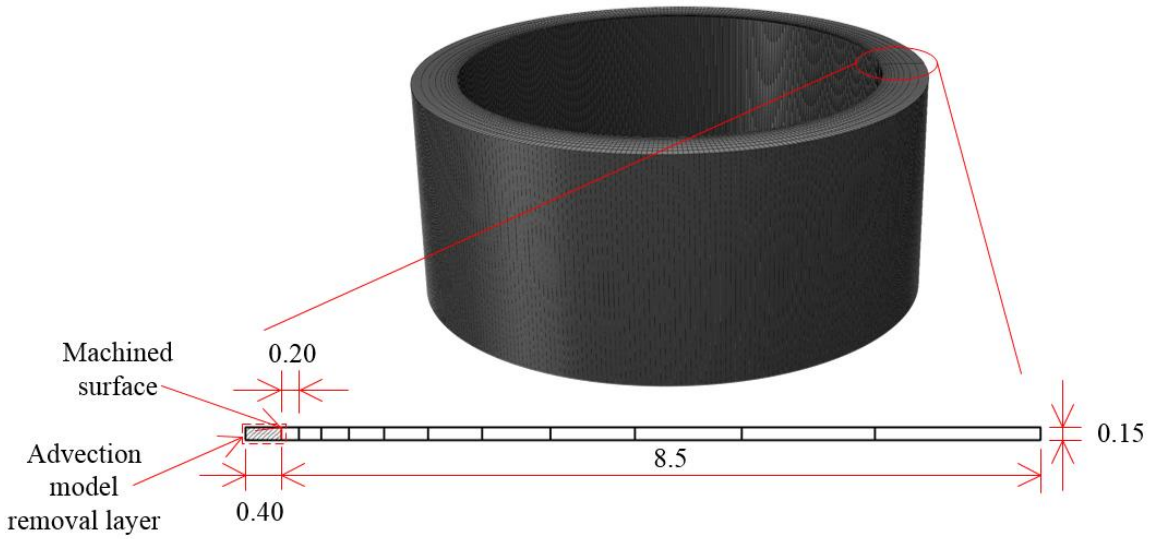

Figure 3.8 FEM mesh of the workpiece and the radial cross-sectional view of the spiral mesh step (unit: mm).

3.4.2 Inputs for FEM Thermal Models

In Models #1 and #2, the time step was 5.28×10^{-5} s, which was the element length along the circumferential direction divided by the cutting speed. No discrete steps were needed for Model #3. For Model #4, the time step was 1.90×10^{-2} s ($=5.28\times10^{-5}\times360$ s as one revolution covers 360 elements). The initial temperature was 26°C.

The total heat source was calculated using experimentally measured tangential cutting force times cutting speed, assuming all cutting energy converted to heat. A heat partition coefficient, *B*, was required to specify the ratio of heat that would be applied on each model. Inverse heat transfer method, as described in [4, 6, 11], was utilized to solve *B* for each model. The discrepancy between measured temperature by TC1 and FEM model prediction was defined as the objective in the inverse heat transfer problem. The objective function was set to minimize

the root-mean-square deviation (RMSD) of the time-temperature curves between experimental measurements and FEM models. The *B* obtained from the inverse heat transfer problem was different from the heat partition ratio defined on the shear plane. For Model #1, *B* represents the portion of total thermal energy that was generated on the shear plane and partitioned between the workpiece and chip. For Model #2 to #4, *B* indicates the percentage of total heat that left in the workpiece after machining.

In the four FEM models, the corresponding partition of the total heat was applied uniformly as a surface heat flux on different elemental surfaces as indicated in Fig. 3.1. In Model #1, the shear plane heat source was applied uniformly on the 0.4 mm × 0.15 mm element surface, as marked with hatch in Fig. 3.8. In Model #2, the fraction of heat that flew into the workpiece was applied uniformly on the machined surface area of one element (0.7 mm × 0.15 mm) as a surface heat flux. In Model #3, the fraction was evenly added on the 0.7 mm × 0.15 mm heat carrier outer surface facing the bore machined surface. In Model #4, the heat flux was applied on the 360 elemental surfaces of the spiral ring (80 mm in diameter and 0.15 mm in height).

The surface heat flux strength for each model was calculated through total heat source times heat partition coefficient divided by corresponding elemental surface area.

In Model #3, time increment is a critical parameter. While ABAQUS/Standard (in Models #1, #2, and #4) needs iterations to solve a nonlinear problem, ABAQUS/Explicit solver (in Model #3) determines the solution without iterating by explicitly advancing the kinematic state from the previous increment. In Model #3, the stable time increment was related to the thermal conductance in the gap between the heat carrier and workpiece. Although higher thermal conductance guarantees a non-disturbed flow across the gap, it also lowers the time increment, resulting in longer computational time. Trial-and-error found that conductance of 100 W/m·K offered a good compromise between thermal contact and computational time.

3.5 Results

3.5.1 Experimental Results

3.5.1.1. Cutting Force and Torque Measurement

The measured three directional cutting forces and one axial torque components are shown in Fig. 3.9. F_x and F_y were two sine waves with 90° phase shift while axial force and torque were almost constant. The tangential, radial, and axial cutting forces were 96.6 N, 53.2 N and 28.1 N, respectively.

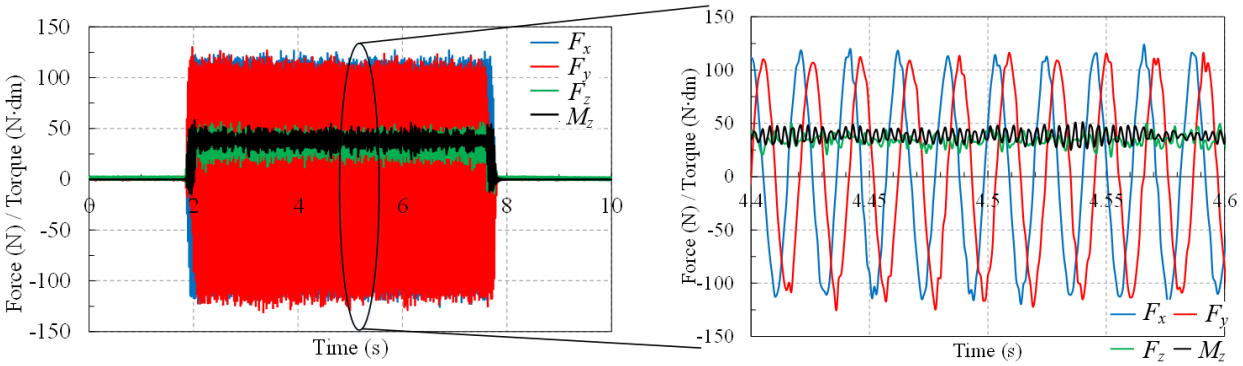

Figure 3.9 Cutting forces and torque measurement by piezoelectric dynamometer.

3.5.1.2. Embedded Thermocouple Temperature Measurement

The temperature measured by the six thermocouples (TC1 to TC6) is shown in Fig. 3.10. The temperature varied depending on the distance between thermocouple hole bottom and machined surface (listed in Table 3.1). TC1 was the closest to the machined surface (2.0 mm) and had the highest peak temperature. In general, the workpiece temperature increased by about 4 to 7°C at different radial locations during boring.

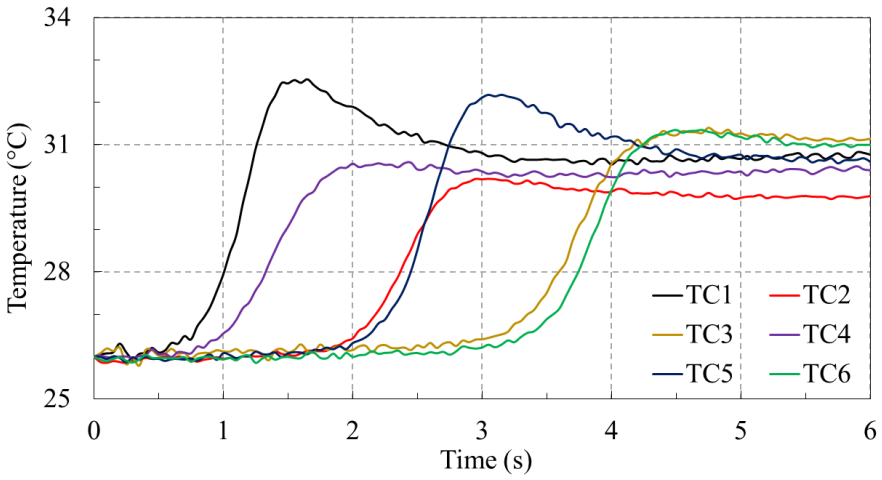

Figure 3.10 Workpiece temperature measured by six embedded thermocouples.

3.5.1.3. Tool-foil thermocouple calibration

Figure 3.11 shows the temperature vs. voltage calibration curve in three tests based on the setup described in Sec. 3.3.2 for the tool-foil thermocouple method. Three calibration tests were repeatable. The fitted quadratic calibration equation, as shown in Fig. 3.11, was used to convert measured tool-foil thermocouple voltage to temperature.

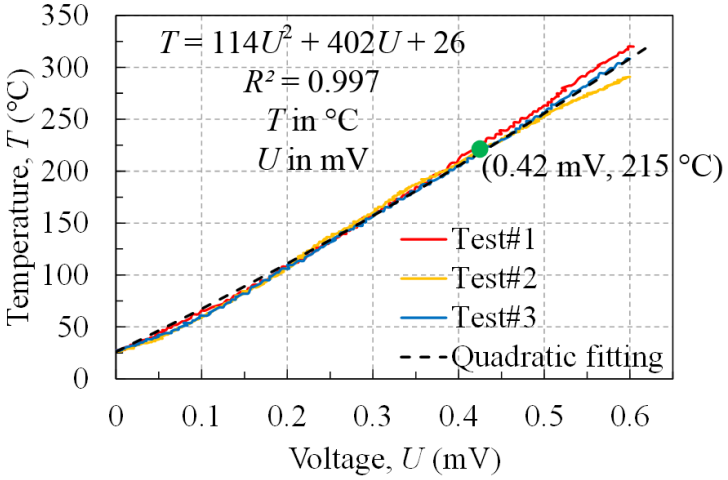

Figure 3.11 Calibration curve of the tool-foil thermocouple voltage output (*U*) and temperature (*T*).

3.5.1.4. Tool-foil Thermocouple Temperature Measurement

The tool-foil voltage, F_z, and M_z in finish boring experiment are shown in Fig. 3.12(a). As shown in Fig. 3.12(b), the peaks of tool-foil thermocouple voltage corresponded to the low points (valleys) of M_z, indicating that these voltage peaks were generated when the tool was in contact with the soft foil and insulation materials. As illustrated in the cross-section of tool-foil cutting in Fig. 3.4(b), among the multiple intermittent contact between the foil and curved tool tip, the last contact (as marked with yellow circle) best indicated the workpiece temperature on machined bore inner surface at the tool-workpiece interface. Thus, the last voltage peak (0.42 mV) was used to convert to the workpiece temperature (215°C) on machined surface in finish boring using the point indicated in the calibration curve in Fig. 3.11.

3.5.2 FEM Thermal Model Results

3.5.2.1. Inverse Heat Transfer Method for the Solution of Heat Partition Ratio

Following the procedures in Sec. 3.4.2, results of the heat partition ratio B are listed in Table 3.2. The corresponding heat fluxes based on the partitioned thermal energy applied onto corresponding elemental surfaces in Models #1 to #4 were calculated as 14380, 3174, 3174 and 8.816 MW/m^2. These heat fluxes were used in FEM to calculate the temperature at TC1. Figure 3.13 shows the experimentally measured and calibrated FEM models (#1 to #4) predicted temperature at TC1.

Table 3.2 Heat partition ratio obtained by inverse heat transfer method

Model	Heat partition ratio, B	RMSD
#1 Advection	67.5%	0.028
#2 Surface heat	26.0%	0.029
#3 Heat carrier	26.0%	0.030
#4 Ring heat	26.0%	0.026

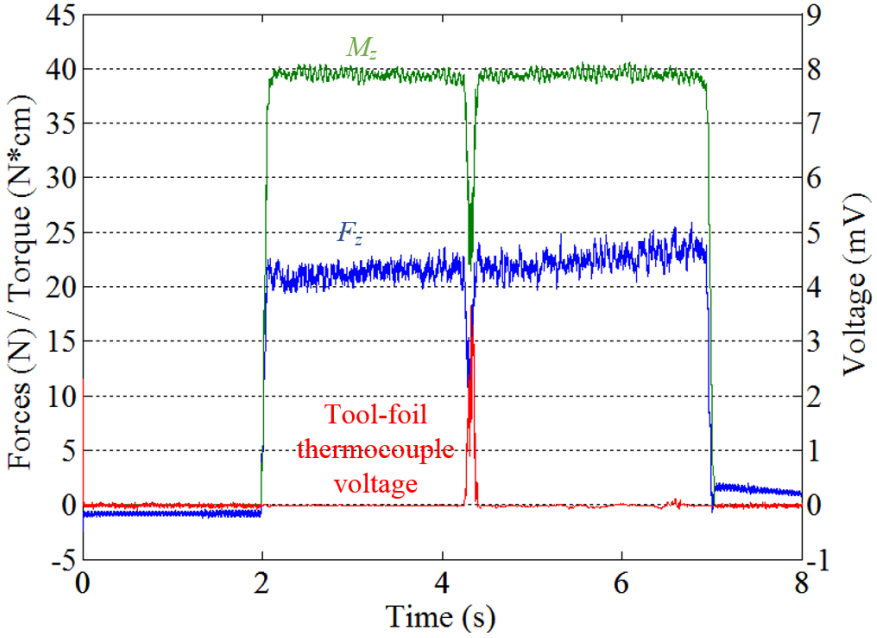

(a)

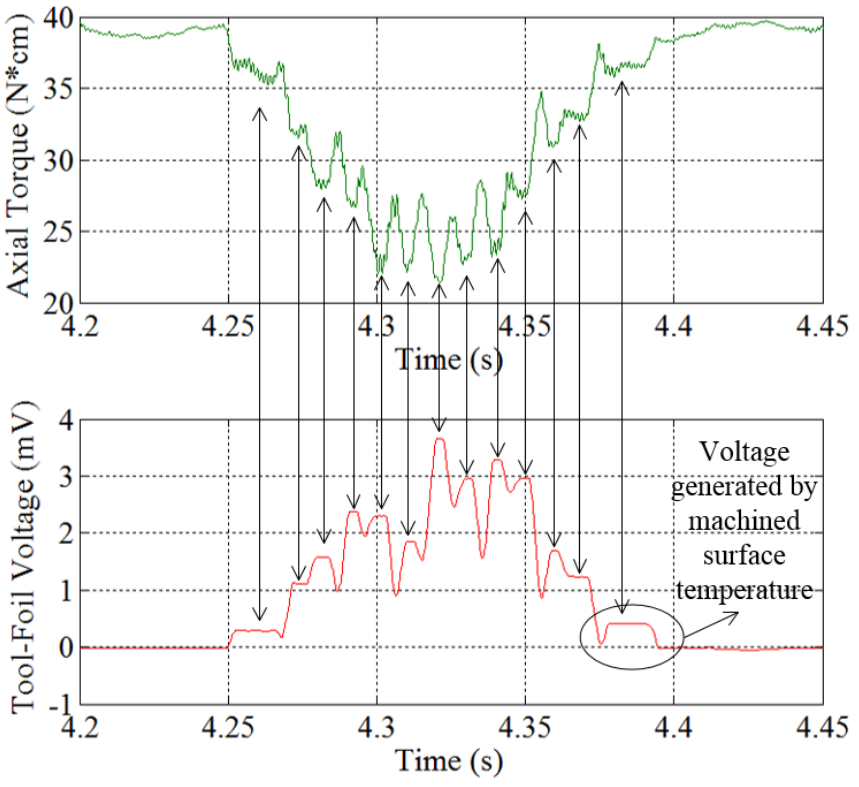

(b)

Figure 3.12 Finish boring test with tool-foil thermocouple: (a) the measured F_z, M_z, and tool-foil thermocouple voltage and (b) close-up view of M_z and tool-foil thermocouple voltage in a 0.25 s span.

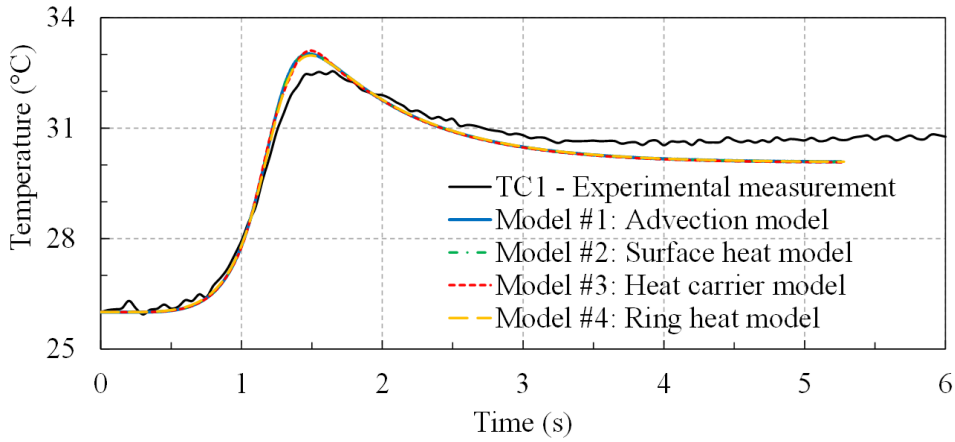

Figure 3.13 Comparison of the TC1 temperature between experimentally measured data and FEM thermal model predicted results based on the value of *B* solved using the inverse heat transfer method.

3.5.2.2. Workpiece Temperature at Embedded Thermocouple Locations

Using the heat flux, the workpiece temperature at six embedded thermocouple locations can be calculated based on four FEM thermal models. Figure 3.14(a) shows FEM model temperature predictions at six thermocouple locations. All four models yielded almost identical temperature predictions at all thermocouple locations. Figure 3.14(b) shows the comparison between FEM Model #4 ring heat model predictions and experimental measurements at six thermocouple locations. The model outputs show good correlations with the experimental measurements. At TC2, the larger discrepancy might be due to improper contact of thermocouple tip and hole bottom surface.

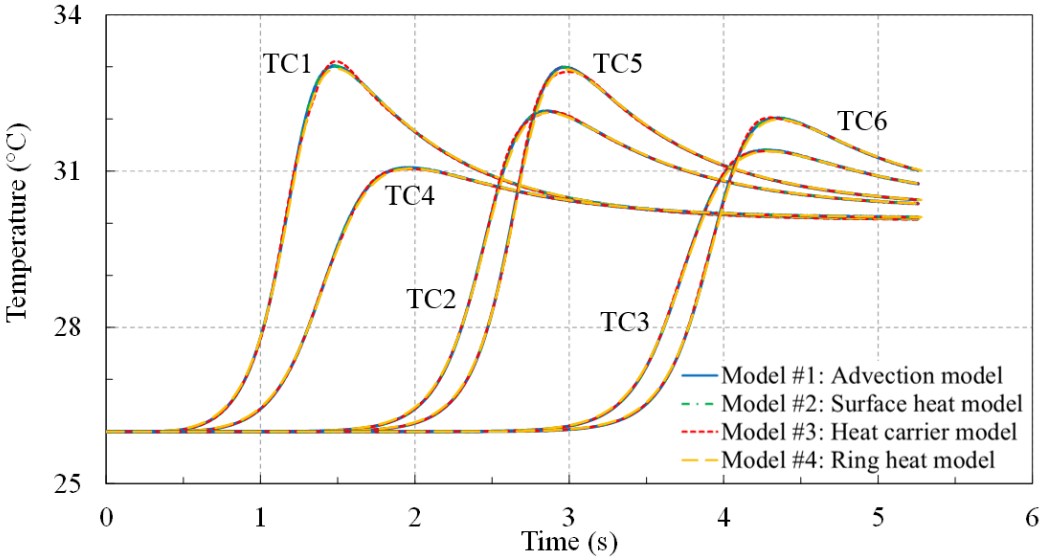

(a)

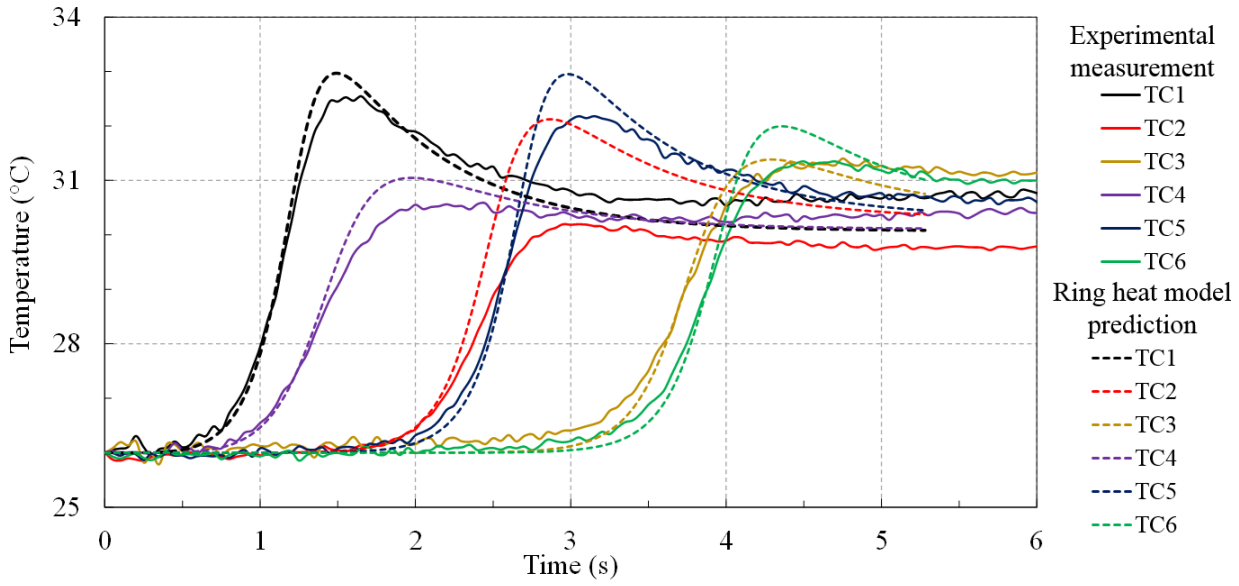

(b)

Figure 3.14 Comparison between (a) four FEM thermal Models and (b) Model #4 and experimentally measured temperatures at six thermocouple locations.

3.5.2.3. Machined Surface Temperature Prediction

The node on machined surface corresponding to axial and circumferential location of TC1 was extracted from the simulation results for machined surface temperature comparison. Figure 3.15 shows the machined surface temperature predicted by four FEM Models. Two peaks were

observed. The first peak happened when the heat source moved across the element above the node, while the second peak appeared when the heat source was applied on the element below the node.

At the first peak, Model #1 had a lower peak value and faster temperature drop because of additional surrounding material (elements) to dissipate the heat. Model #3, the heat carrier model, tended to overestimate the peak temperature. This overestimation could be greater if the mesh becomes coarser or nodes of the workpiece mesh are misaligned with the carrier. In thermal contact, heat flows through nodal points. When the carrier is heated, the heat conducts through the nodes, via the thermal contact condition in ABAQUS, into the workpiece. As a result, at an instantaneous time when the nodes are in contact, a rapid temperature rise would occur. If the nodal contact frequency is low, the heat is accumulated in the carrier and released suddenly, consequently leading to a huge temperature rise. Proper mesh arrangement can mitigate the problem but may not completely eliminate it.

At the second peak, FEM Models #1 to #3 provided similar peak temperature predictions at 228, 234, and 221°C correspondingly, which correlated well with the tool-foil thermocouple prediction of 215°C. This validates results of two temperature measurement methods.

Model #4, the ring heat model, gave a maximum temperature prediction of only 60°C at both peaks. Because the ring heat flux was evenly applied on the spiral tool path instead of individual element, Model #4 could not show the detailed nodal temperature peaks within each revolution.

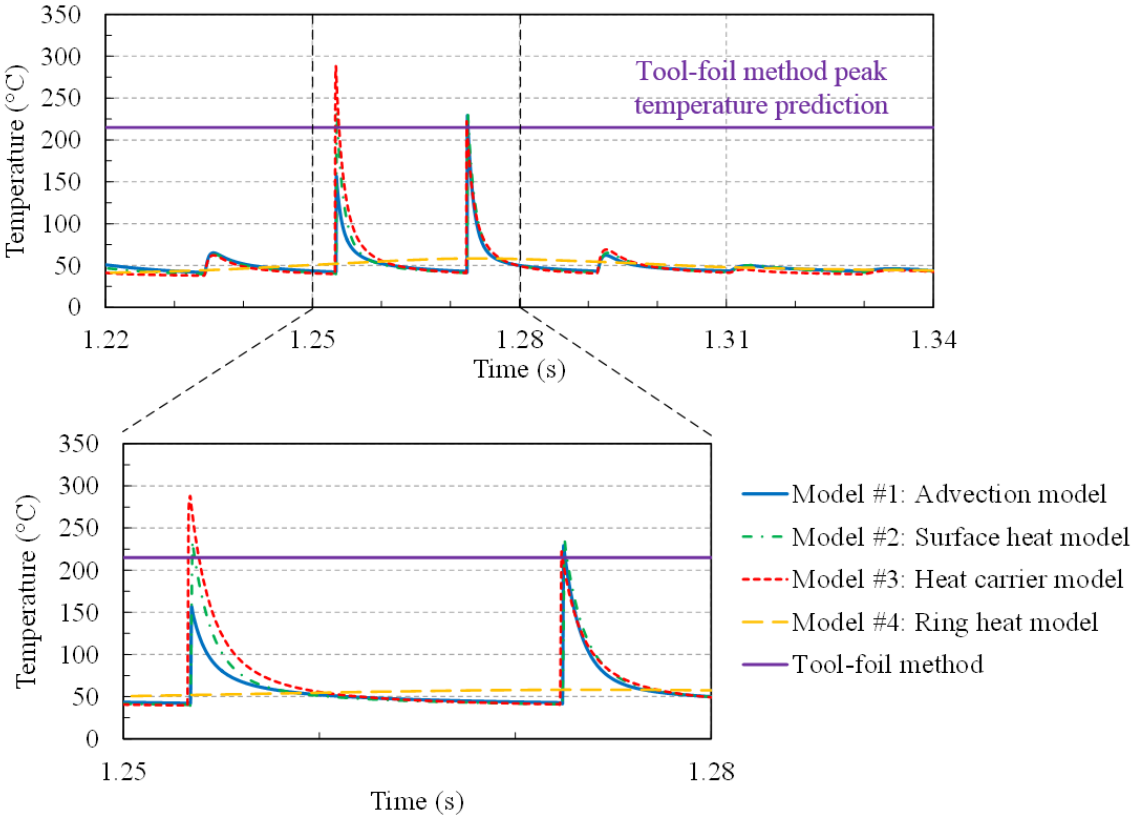

Figure 3.15 Peak temperature prediction by four models at machined surface node corresponding to TC1 location.

3.5.2.4. Computational Time

The computational time of the four FEM models using the same workstation (Intel Xeon CPU E5-2630 V3, 2 processors, 80 GB RAM) with 32 CPUs are compared in Fig. 3.16. Model #1 was the most time-consuming, followed by Model #2, at about 36% of Model #1. Computational time for Model #4 (0.1%) was significantly shorter and Model #3 (5.0%) was the second fastest. Note that this comparison in computational time was qualitative because it would be affected by the complexity of actual models, number of elements, type of elements, computer, etc.

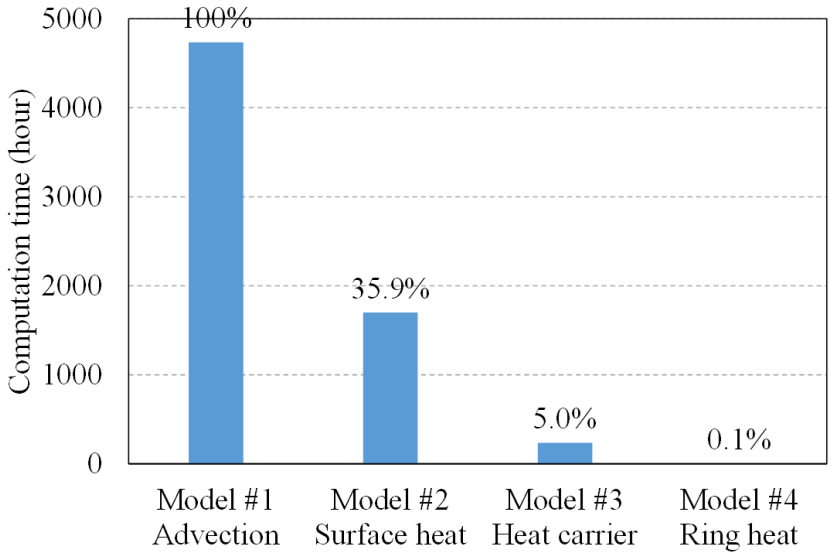

Figure 3.16 Comparison of computation time of the four FEM Models.

3.6 Discussions

Based on the results, the models are compared in terms of efficiency, accuracy and feasibility in finish boring.

Model #1, the advection model, is the most time-consuming method because of its highest complexity involving step-by-step heat flux input and element removal. As shown in Fig. 3.14, all models provided comparable temperature predictions as seen in experimental measurements at thermocouple locations 2.0-3.1 mm away from the machined surface. But for temperature on the machined surface, the element removal simulation in Model #1 makes it the most accurate model. As shown in Fig. 3.15, at the first peak, result of Model #1 shows the most realistic temperature profile by simulating the heat dissipation process within the actual workpiece shape during cutting.

Model #2, the surface heat model, while similar to Model #1, has no element removal involved and thus runs faster. It provides comparatively realistic local temperature (2.6% discrepancy at the second peak compared to that of Model #1) except for the heat dissipation around the first peak. Despite many time steps required, it is a good trade-off (compared to Model #1) for simulating finish boring processes with a shallow depth of cut.

Model #3, the heat carrier model, is even faster than Model #2 because fewer time steps are needed using the explicit solver, which is more efficient than the implicit method (Model #2) due to elimination of iteration and convergence checking at each time step. However, the

computational time largely depends on the stable time increment in the explicit method. Key parameters that affect stable time increment need to be tuned properly to maximize its efficiency. When dealing with large and complex models or curved, inclined cutting trajectory, Model #3 is a practical option because of its simplicity in model setup. It provides reasonably realistic local temperature (3.1% discrepancy at the second peak compared to results of Model #1) for workpiece thermal expansion analysis. However, it may overestimate the peak temperature due to thermal contact setup.

Model #4, the ring heat model, is the simplest and most time efficient because it simulates on an average basis without as many steps as the other models. It is easy to use and extends to a complex model. It provides a time-efficient method to evaluate the global workpiece temperature rise, but it lacks the capability to simulate local temperature gradient and associated behaviors. Although the affected area is relatively small compared to the entire contour, the large temperature gradient at the cutting edge determines the actual depth of cut during finish boring, and thus the final bore shape. For finish boring cylindricity analysis, it is important to have an accurate prediction of workpiece temperature on the machined surface around the cutting edge.

In simulation of a finish boring process to study the cylindricity error of the machined bore in a complex geometry like engine blocks, Models #1 and 2 are limited by the large number of time steps. A fine mesh on a cylinder liner model may requires tens of thousands of elements and time steps. Model #4 provides only global temperature distribution, but it can be utilized to quickly solve the inverse heat transfer problem to determine how much of the total thermal energy is left in the workpiece after boring. Based on that value of the heat partition ratio B, Model #3 is the best trade-off between accuracy and computational efficiency. It offers comparatively accurate local temperature field within an affordable computational time. Thus, a combination of Models #3 (the heat carrier) and #4 (the ring heat) would be the most feasible solution for predicting workpiece temperature in finish boring process.

For detailed workpiece temperature distribution in finish boring to study thermal expansion induced bore cylindricity error, it is suggested to use the ring heat model first to calibrate the heat source strength and then the heat carrier model to calculate local temperature profile. If detailed temperature profile near the cutting tip is required only for a specific area, it is more efficient to couple the two modelling concepts by using the ring heat model first to simulate until the time instance of a specific revolution of the tool. Then, the heat carrier model can use the ring model

temperature output as the initial condition to estimate the local temperature in a specific time during the next revolution.

3.7 Conclusions

In this chapter, four FEM thermal models were modified from the literature for analysis of the workpiece temperature in finish boring. Finish boring tests were carried out to experimentally measure the workpiece temperature and evaluate the four thermal models. Globally, good correlations were achieved between four models and temperature measured by embedded thermocouples, indicating that all four models could predict global workpiece temperature in finish boring. Locally, Model #1 (the advection model) provided the most accurate peak temperature prediction on machined surface while Models #2 (the surface heat model) and #3 (the heat carrier model) gave peak temperature predictions within 2-3% discrepancy. The model prediction matched with experimental measurements by tool-foil thermocouple method. Only Model #4 (the ring heat model) lacked the competency of predicting the peak temperature around the cutting edge. For finish boring study on workpiece temperature distribution and machined bore distortion, to reach the best trade-off between accuracy and computational efficiency, it is suggested to use Model #4 (the ring heat model) first to determine the portion of heat left in the workpiece through inverse heat transfer method and then Model #3 (the heat carrier model) to determine the detailed workpiece temperature profile near the tool tip.

References

[1] J.D. Meadows, Geometric Dimensioning and Tolerancing Handbook: Applications, Analysis & Measurement, ASME Press, New York, 2009.

[2] G. Subramani, S.G. Kapoor, R.E. DeVor, A model for the prediction of bore cylindricity during machining, Journal of Manufacturing Science and Engineering 115 (1) (1993) 15-22.

[3] N.N. Kakade, J.G. Chow, Finite element analysis of engine bore distortions during boring operation, Journal of Manufacturing Science and Engineering 115 (4) (1993) 379-384.

[4] Y. Tang, K. Ding, H. Sasahara, K. Nishimura, T. Watanabe, Clarification of the amount of machining error resulting from the cutting force and thermal expansion during the cylinder liner boring process, Journal of Advanced Mechanical Design, Systems, and Manufacturing 2 (3) (2008) 332-342.

[5] Y. Tang, H. Sasahara, Investigation of thermal behavior on cylinder liner during its boring process, International Journal of Machine Tools and Manufacture 47 (14) (2007) 2162-2171.

[6] Y. Zheng, H. Li, W.W. Olson, J.W. Sutherland, Evaluating cutting fluid effects on cylinder boring surface errors by inverse heat transfer and finite element methods, Journal of Manufacturing Science and Engineering 122 (3) (2000) 377-383.

[7] D. Ulutan, T. Ozel, Machining induced surface integrity in titanium and nickel alloys: A review, International Journal of Machine Tools and Manufacture 51 (3) (2011) 250-280.

[8] Y.B. Guo, C.R. Liu, 3D FEA modeling of hard turning, Journal of Manufacturing Science and Engineering 124 (2) (2002) 189-199.

[9] J. Sun, Y.B. Guo, A comprehensive experimental study on surface integrity by end milling Ti–6Al–4V, Journal of Materials Processing Technology 209 (8) (2009) 4036-4042.

[10] F. Hashimoto, Y.B. Guo, A.W. Warren, Surface integrity difference between hard turned and ground surfaces and its impact on fatigue life, CIRP Annals-Manufacturing Technology 55 (1) (2006) 81-84.

[11] G. Subramani, M.C. Whitmore, S.G. Kapoor, R.E. DeVor, Temperature distribution in a hollow cylindrical workpiece during machining: theoretical model and experimental results, Journal of Manufacturing Science and Engineering 113 (4) (1991) 373-380.

[12] A.O. Tay, M. G. Stevenson, G.D.V. Davis, Using the finite element method to determine temperature distributions in orthogonal machining, Proceedings of the Institution of Mechanical Engineers 188 (1) (1974) 627-638.

[13] J.S. Strenkowski, K.J. Moon, Finite element prediction of chip geometry and tool/workpiece temperature distributions in orthogonal metal cutting, Journal of Engineering for Industry 112 (4) (1990) 313-318.

[14] T.D. Marusich, M. Ortiz, Modelling and simulation of high‐speed machining, International Journal for Numerical Methods in Engineering 38 (21) (1995) 3675-3694.

[15] T. Özel, E. Zeren, Finite element modeling the influence of edge roundness on the stress and temperature fields induced by high-speed machining, The International Journal of Advanced Manufacturing Technology 35 (4) (2007) 255-267.

[16] P.R. Dawson, S. Malkin, Inclined moving heat source model for calculating metal cutting temperatures, Journal of Engineering for Industry 106 (3) (1984) 179-186.

[17] M. Bono, J. Ni, A model for predicting the heat flow into the workpiece in dry drilling, Journal of Manufacturing Science and Engineering 124 (4) (2002) 773-777.

[18] B.L. Tai, A.J. Jessop, D.A. Stephenson, A.J. Shih, Workpiece thermal distortion in minimum quantity lubrication deep hole drilling—finite element modeling and experimental validation, Journal of Manufacturing Science and Engineering 134 (1) (2012) 011008.

[19] R.G. Watts, Temperature distributions in solid and hollow cylinders due to a moving circumferential ring heat source, Journal of Heat Transfer 91 (1969) 465–470.

[20] L. Chen, B.L. Tai, R. Chaudhari, X. Song, A.J. Shih, Measurement of machined surface temperature in hard turning, International Journal of Machine Tools and Manufacture (submitted).

CHAPTER 4
BORE CYLINDRICITY IN FINISH CYLINDER BORING

4.1 Introduction

Precision finish boring is a critical process for machining an accurate cylinder for engine block, hydraulic actuator, pumps, and other precision mechanical components. The geometrical accuracy of cylinders is defined by cylindricity, which is critical to the product performance. Using the cylinder bore in engine block as an example, cylindricity is important for the engine power, oil consumption, and piston ring friction [1-3]. The cylindricity tolerance is specified by a tolerance zone bounded by two concentric cylinders within which the surface must lie [4]. For a typical engine cylinder of about 70 to 100 mm in diameter, the typical cylindricity tolerance is about 20 to 25 μm. To achieve such accurate cylindricity, a three-pass cylinder boring process, including the rough boring, semi-finish boring, and finish boring, is common in the engine block production. Finish boring is the machining process to achieve the cylinder bore dimensional and geometrical accuracy before the subsequent honing process.

Figure 4.1(a) illustrates the engine block finish boring, which utilizes a boring bar with single-point cutting tool (Fig. 4.1(b)). This chapter is aimed to understand four major error sources due to 1) cutting force, 2) workpiece thermal expansion, 3) machine tool (particularly spindle), and 4) fixture/clamping for the bore cylindricity in finish boring.

Cutting force leads to deformation of workpiece and deflection of the boring tool [5-7]. The local high temperature in the workpiece results in the workpiece thermal expansion and causes cylindricity errors [5-8]. On machine tool, the spindle error changes the tool trajectory thus affects the bore shape [9-11]. In the close-up schematic view of the finish boring tool-workpiece contact region shown in Fig. 4.1(c), the single point cutting tool has a nominal depth of cut. During boring,

the cutting force pushes the workpiece and cutting tool away from each other, resulting in smaller depth of cut. The high temperature at the tool tip leads to thermal expansion of the bore towards the bore center, enlarging the depth of cut. The effect of spindle error motion on the bore shape has not been studied and will be investigated. All these effects lead to the variation of actual depth of cut in boring, as illustrated in Fig. 4.1(d), and generate an imperfect cylinder bore and the cylindricity error.

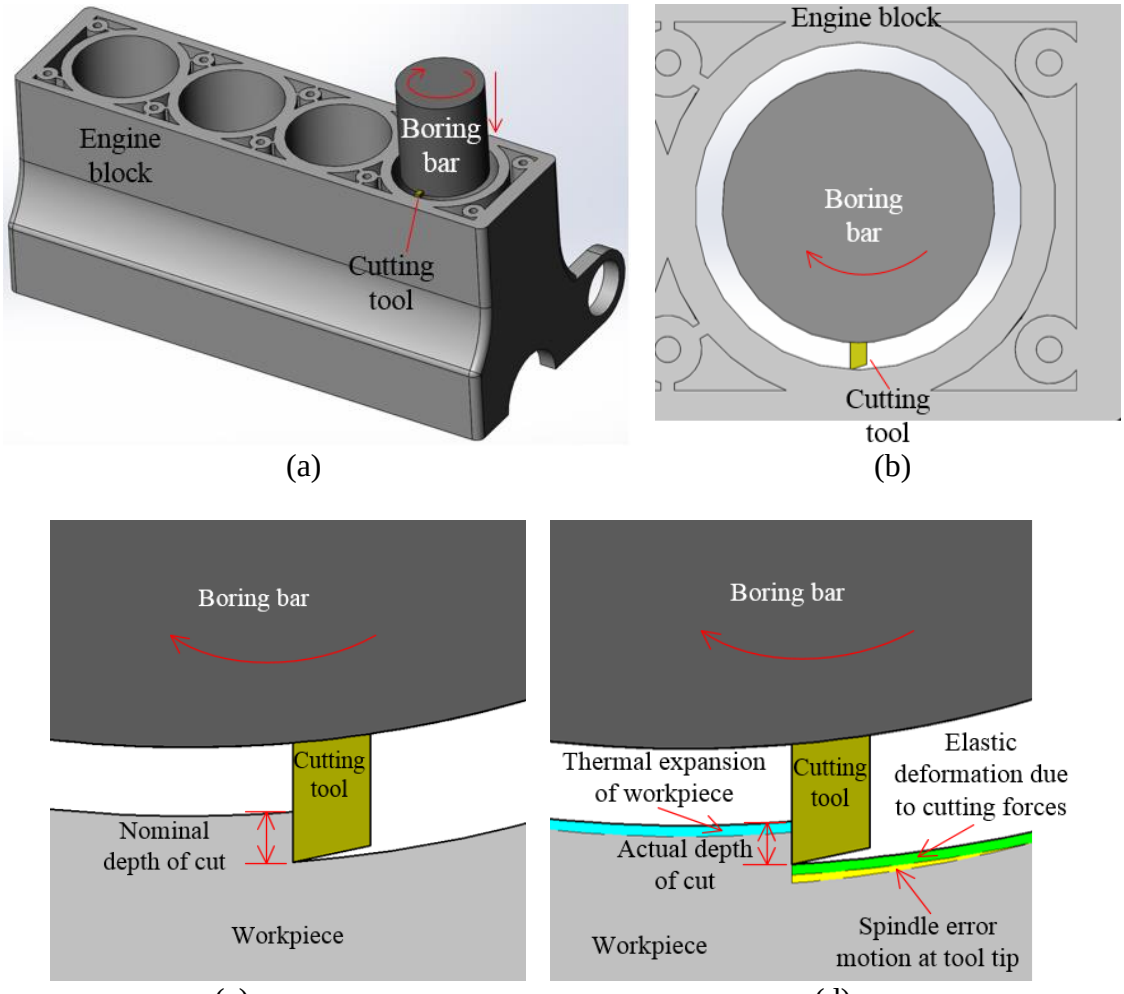

Figure 4.1 Finish cylinder boring process: (a) overview for boring a four cylinder engine block, (b) top view of the workpiece, boring bar, and cutting tool, and close-up views of (c) the nominal depth of cut, and (d) the actual depth of cut.

After boring, the fixture and clamping forces reach a new state with a thinner liner. The clamping force is a potential cylindricity error source depending on the workpiece geometry. Other

cylindricity error sources like the boring tool wear and workpiece residual stress are not considered in this study.

Research has been conducted to study the cylindricity in boring. Subramani et al. [5] predicted the cylindricity in semi-finish boring of a cast iron engine block using the finite element method (FEM) incorporating a mechanistic force model (for cutting force induced elastic deformation) and an analytical thermal model [12] (for thermal expansion of the workpiece). The cylinder block geometry (e.g. water jacket) affected the structural stiffness and elastic deformation due to cutting force. The azimuthal symmetry assumption in the thermal model led to a thermal expansion prediction independent of the circumferential position. Kakade and Chow [6] applied FEM to simulate the rough boring process using the single nodal heat source, constant heat partition ratio, layer-by-layer element removal for thermal expansion, and experimentally measured cutting force for elastic deformation. The cylinder bore distortion due to thermal effect was about an order of magnitude larger than that due to cutting force. However, the point heat source setup in the study would overestimate the workpiece temperature [12] and experimental validation of the bore distortion predictions was missing. Zheng et al. [7] evaluated the bore cylindricity in dry and wet boring using FEM to calculate the elastic deformation based on measured cutting force and thermal expansion based on one-dimensional analytical thermal model, showing that thermal deformation was the dominate factor (90% for dry boring and 85% for wet boring of Aluminum 308). The temperature gradient in the radial direction was missing. Tang et al. [8] developed an experimental method to identify the workpiece thermal expansion in finish boring using a YAG laser heating process. The deformation caused by thermal expansion was dominant, contributing to about 66% to 87% of the total deformation. The contribution of elastic deformation was not validated through experiment or modelling.

Aforementioned studies reported that workpiece geometry around the cylinder bore and thermal expansion of the bore are major factors determining the bore cylindricity. There is a lack of accurate thermal models to predict the workpiece temperature and thermal expansion in finish boring. Also, previous studies were based on the assumption of no machine nor spindle error. In finish boring process, the cylindricity error is usually within 10 μm. The machine and spindle error at the cutting tip (about 200 mm from the spindle) will be in the μm level and needs to be considered as an error source for cylindricity in finish boring.

In this chapter, a combination of experimental and FEM analysis is presented to identify

the bore cylindricity error sources in finish boring. FEM is applied to estimate the workpiece thermal expansion and deformation of the workpiece due to cutting and clamping forces. The spindle error is measured experimentally. Harmonic analysis is conducted. The coordinate measuring machine (CMM) measurements of bore geometry are compared with the FEM and spindle radial error motion results.

In this chapter, experimental setups for finish boring and CMM and spindle error measurement are first introduced. FEM for calculation of the workpiece temperature, thermal expansion, and deformation due to cutting and clamping forces are presented. Experimental and FEM results are elaborated for error source identification through harmonic analysis, followed by discussions and conclusions of the work.

4.2 Experimental Studies

4.2.1 Finish Boring Experiment

The finish boring experiment, as shown in Fig. 4.2(a), was conducted on a horizontal machining center (HMC-400EP by Cincinnati Machine, Cincinnati, OH, USA). A single point boring bar (Model 312.611 by Big Kaiser, Hoffman Estates, IL, USA) and a polycrystalline cubic boron nitride (PCBN) insert (TPGW2151EC by Kennametal, Latrobe, PA, USA) were used for dry finish boring with 0.4 mm radial depth of cut, 0.15 mm/rev feed rate, and 794 m/min cutting speed (3228 rpm spindle speed).

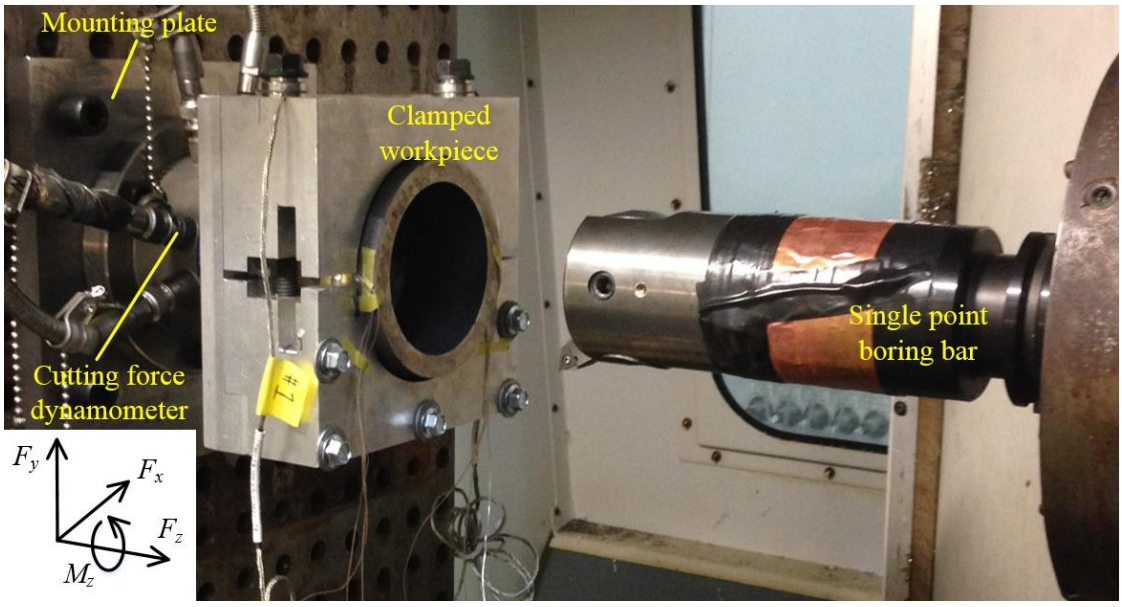

(a)

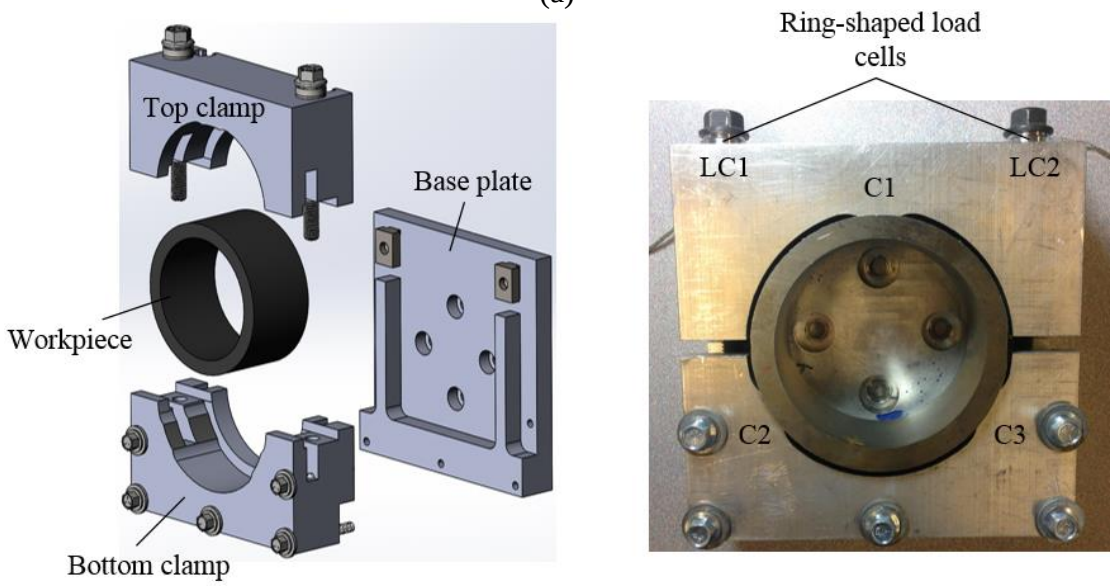

(b)

(c)

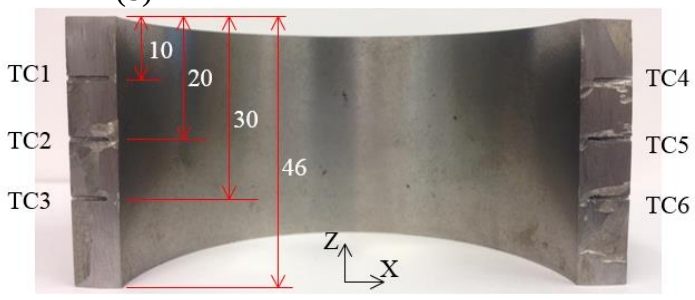

(d)

Figure 4.2 Experimental setup for finish boring experiment: (a) an overview, (b) three-piece three-jaw fixture with two load cells (LC1 and LC2), (c) a ring load cell for clamping force measurement, and (d) pre-drilled holes for thermocouple (TC1 to TC6) (unit: mm).

The workpiece was a grey cast iron liner with 77.5 mm inner diameter (78.3 mm diameter after boring), 96.8 mm outer diameter, and 46.0 mm length. Stress relief annealing was conducted before boring to minimize the residual stress effect on cylindricity error after boring. A three-piece fixture with top clamp, bottom clamp and base plate made of Aluminum 6061 is shown in Fig. 4.2(b). Three clamping jaws, marked as C1, C2, and C3 in Fig. 4.2(b), were in contact with the workpiece. Two bolts were used to clamp the fixture. The clamping forces were measured by two ring-shaped load cells (LC901-3/8-10K by Omega Engineering, Norwalk, CT, USA), marked as LC1 and LC2 in Fig. 4.2(b) and shown in Fig. 4.2(c), between the bolt and fixture. The boring cutting forces (F_x, F_y, and F_z) and torque (M_z), as denoted in Fig. 4.2(a), were measured using a piezoelectric dynamometer (Model 9273 by Kistler, Winterthur, Switzerland). Six thermocouples, three on each side, denoted as TC1 to TC6, were embedded inside the liner through six pre-drilled holes. After boring, the machined workpiece was sectioned into two pieces to measure the distance between the thermocouple hole bottom and the machined surface, as shown in Fig. 4.2(d).

4.2.2 CMM Measurement of Bore Cylindricity

Cylindricity of the workpiece after finish boring was measured by a CMM (Model Contura by Zeiss, Oberkochen, Germany) with the setup shown in Fig. 4.3(a). The whole fixture, including the dynamometer and mounting plate, was placed on the CMM for cylindricity measurement to avoid unclamping. Another XYZ coordinate was defined for CMM measurement as shown in Figs. 4.3(b) and (c) with origin at center of the fixture base plate. Z axis was defined in the axial direction of the cylindrical workpiece, and Y axis was along the clamping direction of the fixture. These axes were identified in the first CMM alignment scan of the bore. After the alignment scan, the CMM determines the bore centerline and calculate the scan path in six layers, as marked in Fig. 4.3(d). In each layer, 2000 points were collected for a 450° scan (90° overlap). Cylindricity of the bore was determined using the minimum zone method [13].

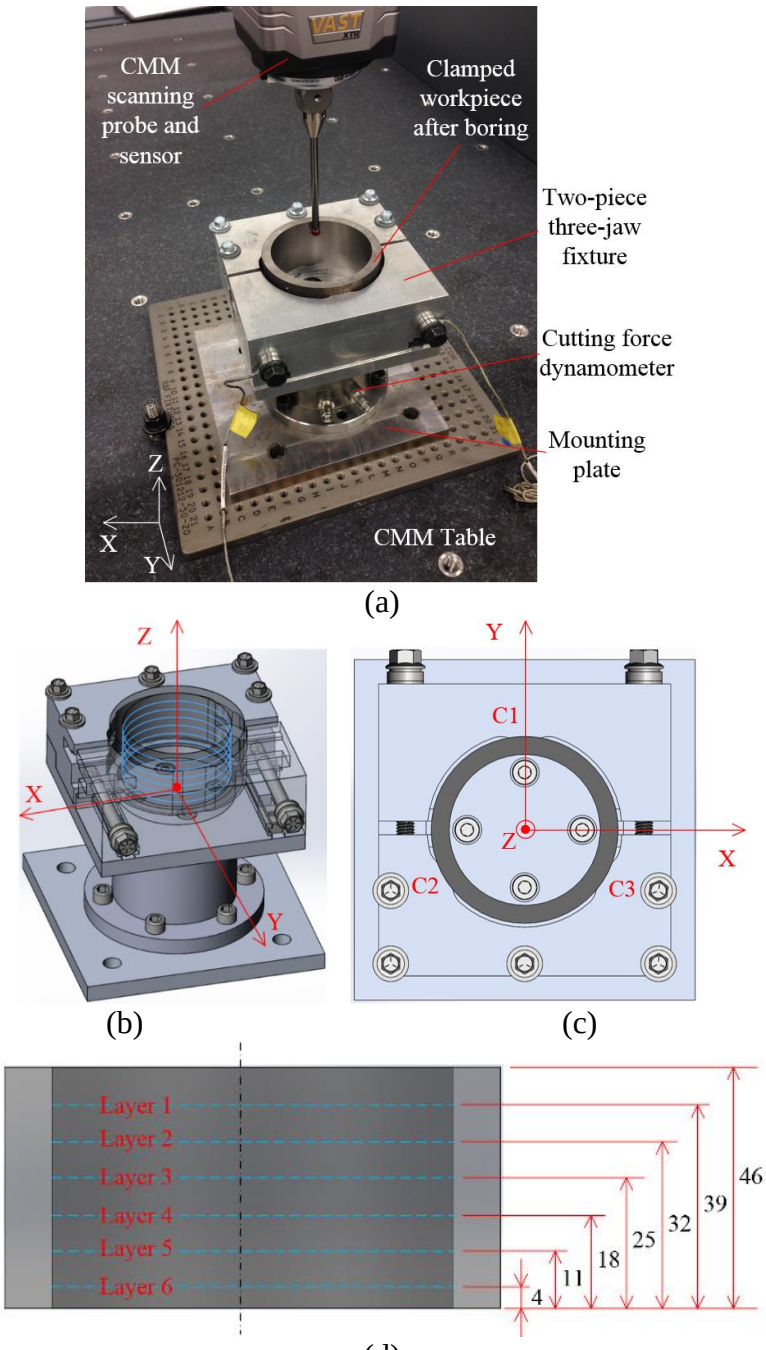

Figure 4.3 CMM measurement: (a) experimental setup, (b) orientation and 6 scanning layers, (c) top view of the workpiece in measurement, and (d) cross-sectional view of the 6 scanning layers and their height (unit: mm).

4.2.3 Spindle Error Measurement

The spindle error analyzer (SEA by Lion Precision, St. Paul, MN, USA), as shown in Fig. 4.4(a), was utilized to measure the spindle error of the boring machine. This system consisted of a

wobble plate, two 25.4 mm diameter master (or gage) balls as spherical reference artifacts, and five capacitive displacement sensors, denoted as X1, X2, Y1, Y2 and Z1 in Fig. 4.4(b). Using the wobble plate (Fig. 4.4(a)), two reference spheres rotated eccentrically to the spindle axis and generated a sinusoidal signal at X1, X2, Y1, and Y2 with same frequency. This signal was acquired by these four capacitance sensors to identify the starting and ending point of each revolution and thus spindle angular position, θ. Removing the eccentricity induced sinusoidal signal from the sensor outputs, radial error components along X and Y directions, denoted as ΔX and ΔY, could be obtained.

The radial error motion of the spindle Δr_1 at master ball #1 as a function of spindle angular position, θ, can be calculated as:

$$\Delta r_1(\theta) = \Delta X_1(\theta)\cos\theta + \Delta Y_1(\theta)\sin\theta \quad (1)$$

where $\Delta X_1(\theta)$ and $\Delta Y_1(\theta)$ are outputs at sensors X1 and Y1 in angular position θ removing the sinusoidal signal part due to master ball eccentricity.

Spindle error at the master ball #2 ($\Delta r_2(\theta)$) position is analyzed using the same approach and measured data at sensors X2 and Y2.

During the spindle error measurement, the reference artifact was rotating at 3228 rpm, the same spindle speed in finish boring. Displacement data were recorded by five capacitive displacement sensors for 32 revolutions with 256 data points in each revolution. Data from the axial capacitive displacement sensor Z1 was not used in the analysis.

As shown in Fig. 4.4(b), master balls #1 and #2 were 173 and 97 mm, respectively, from the spindle nose. The distance between boring tool tip and the spindle nose was 230 mm (Fig. 4.4(c)). The radial error motion at the tool tip rotation center was calculated using linear extrapolation based on Δr_1 and Δr_2 at master balls #1 and #2, respectively. For the single point boring bar used in this finish boring experiment, the radial motion of the tool tip had the same error shape as that of the tool tip rotation center, varying by an angular offset due to the insert holder position. Based on radial error motion of the tool tip, the synchronous radial error motion at the tool tip, defined as the portion of radial error motion that occurs at integer multiples of the rotation frequency, was acquired through the mean contour of the total radial error motion averaged over the number of revolutions [14] to calculate the spindle error (to be presented in Sec. 4.4.3).

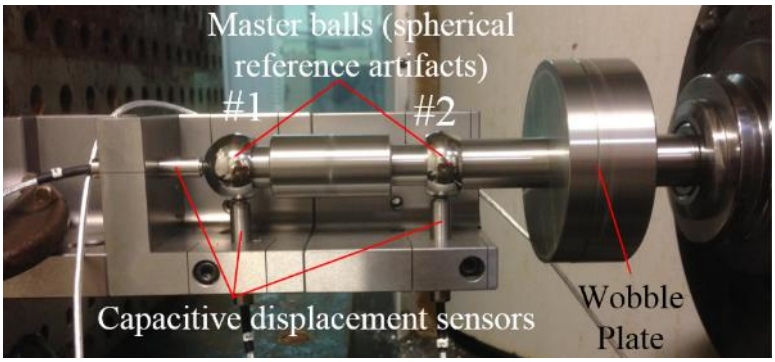

(a)

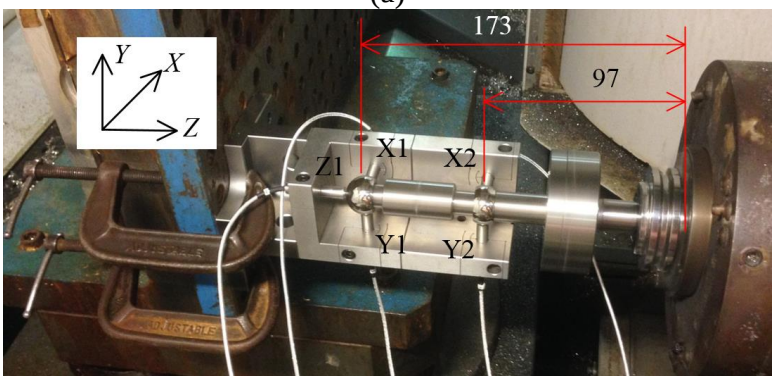

(b)

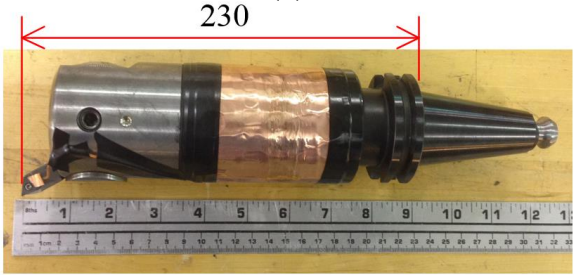

(c)

Figure 4.4 Experimental setup for spindle error measurement using the spindle error analyzer: (a) overview of the setup, (b) dimensions and displacement capacitive sensors arrangement, and (c) distance between boring tool tip and spindle nose (unit: mm).

4.3 FEM Models

The FEM (ABAQUS v6.11-1) was applied to predict the workpiece deformation due to cutting and clamping forces (Sec. 4.3.1) and the workpiece thermal expansion (Sec. 4.3.2).

4.3.1 FEM Models for Workpiece Deformation due to Cutting and Clamping Forces

Two FEM models were developed based on the same mesh setup to calculate deformation of the workpiece due to cutting and clamping forces.

4.3.1.1 FEM Mesh of the Workpiece and Fixture

The workpiece, three key components of the clamping fixture (top clamp, bottom clamp, and base plate), and two clamping bolts were modeled by the FEM mesh shown in Fig. 4.5(a). The eight-node linear brick solid elements, C3D8R and C3D8I in ABAQUS, were selected to mesh the workpiece and clamping fixture, respectively. The bottom clamp and base plate were meshed as one part. Three clamping areas (as shown in Fig. 4.5(a) and close-up view in Fig. 4.6(a)) were meshed with smaller element size to better simulate the contact between clamping jaws and workpiece. Two clamping bolts were mesh using the six-node linear triangular prism element (C3D6 in ABAQUS) in the center axis and the eight-node linear brick solid element (C3D8R) surrounding the center axis. Two load cells (LC1 and LC2) were simplified as part of the clamping bolts in the mesh. The overall mesh included 254,247 nodes and 220,994 elements.

As shown in Figs. 4.5(b) and (c), the base plate was connected using four bolts to the dynamometer, which was assumed to be rigid. The boundary condition in four connecting bolt areas (shown in Fig. 4.5(b)) was assumed to be fixed to simulate the rigid connection to the dynamometer.

Material properties used in FEM are listed in Table 4.1.

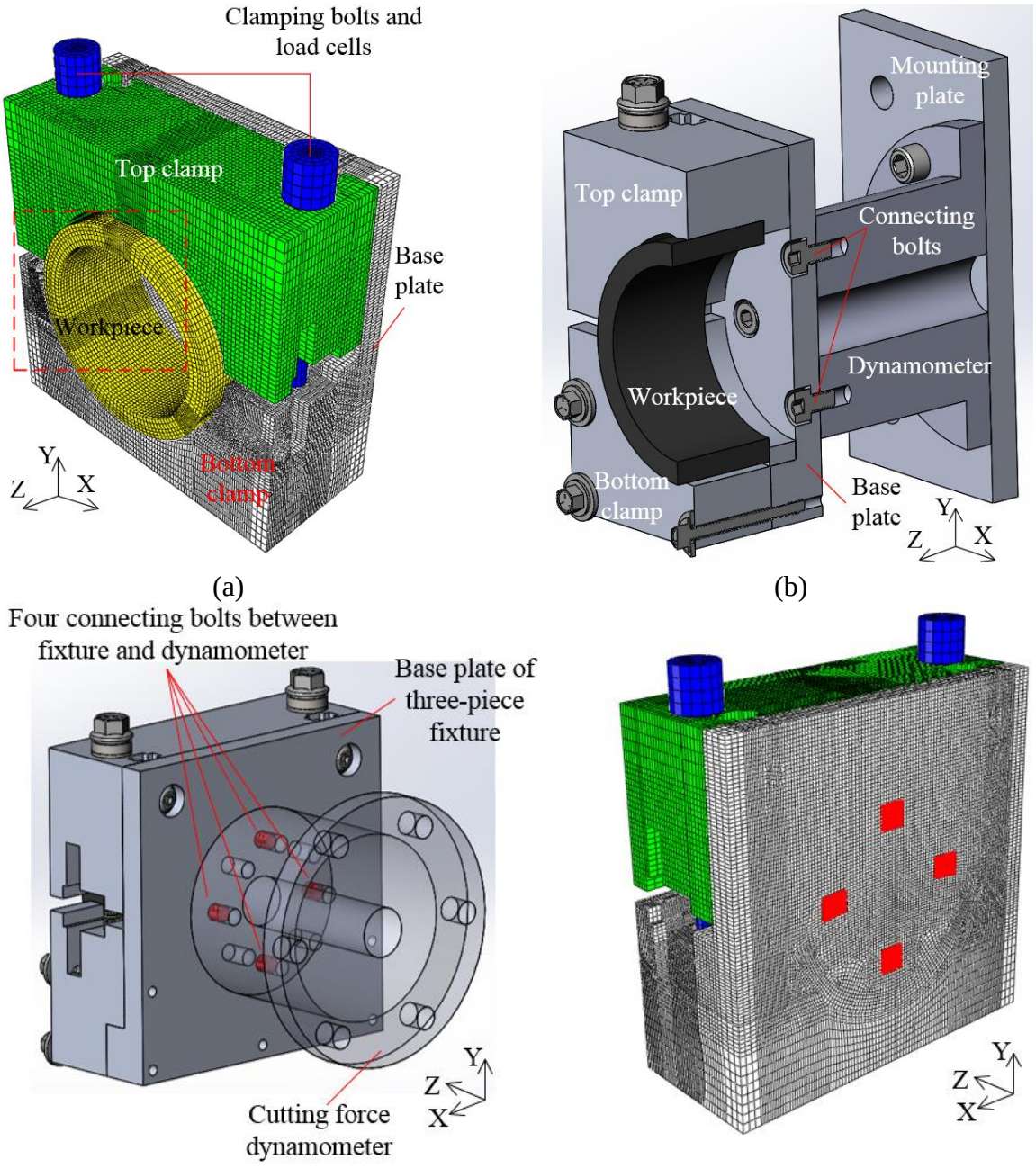

Figure 4.5 FEM setup for analysis of workpiece deformation: (a) overall mesh and key components, (b) and (c) four bolts connecting the base plate of fixture and dynamometer, and (d) four regions on the base plate surface with fixed boundary condition.

Table 4.1 Properties of workpiece and fixture materials.

Material	Grey cast iron	Aluminum 6061	Medium carbon alloy steel
Density (kg/m^3)	7200	2700	7800
Specific heat (J/kg·K)	544	896	486
Thermal conductivity (W/m·K)	45.2	167	51.9
Young's modulus (GPa)	96.5	68.9	200
Poisson's ratio	0.26	0.33	0.29
Hardness, Brinell	235	95	126
Thermal expansion coefficient	1.00×10^{-5} @ 100°C 1.07×10^{-5} @ 200°C 1.19×10^{-5} @ 300°C	--	--

4.3.1.2 Workpiece Deformation due to Cutting Force

Contact areas among components of the clamping fixture and bolts were assumed to be rigidly connected. The experimentally measured cutting force was applied as three nodal force components, $F_{tangential}$, F_{radial}, and F_{axial} illustrated in Fig. 4.6, at a node in each time step. These nodal force components moved node-by-node along the circumferential and axial direction to calculate workpiece deformation and corresponding change in the actual depth of cut during finish boring.

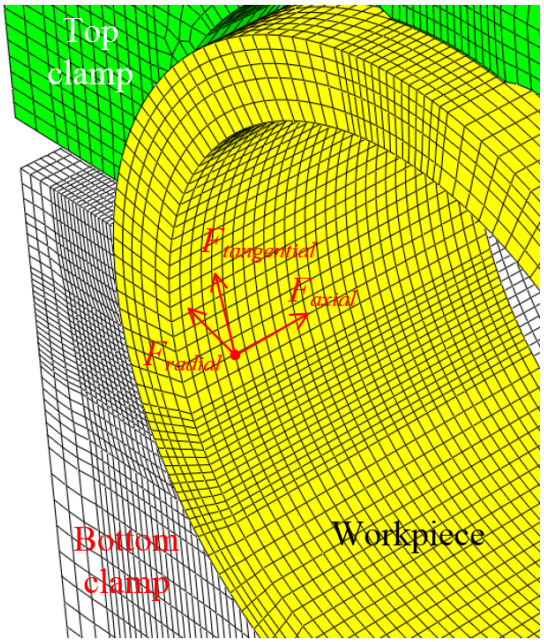

Figure 4.6 Cutting force in close-up view of the FEM mesh.

4.3.1.3 Workpiece Deformation due to Clamping Forces

Contact areas between two clamping bolts and bottom clamp of the fixture were assumed to be rigidly connected through the bolt threads, as shown in Fig. 4.7(a). All other contact areas among fixture component and bolt were assumed to contact rigidly along the normal direction and slide frictionless in the tangential direction. FEM trials with friction in contacting areas had been conducted and results showed that the frictional effect was negligible. Changes in clamping force before and after boring measured by two load cells were applied as the bolt preload on the cross sections of two clamping bolts shown in Fig. 4.7(b).

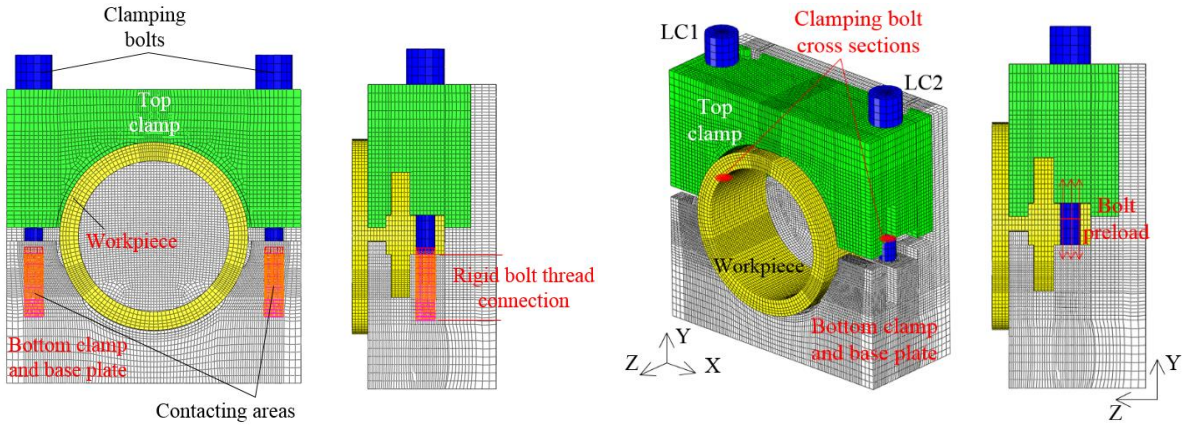

(a) (b)

Figure 4.7 FEM setups for workpiece deformation due to clamping forces: (a) rigid bolt connections and (b) clamping force load.

4.3.2 FEM Models for Thermal Expansion of the Workpiece

Two FEM models were developed to calculate the workpiece temperature and thermal expansion.

4.3.2.1 FEM Mesh for Thermal Model

A different FEM mesh is required for the thermal model. Temperature rise and corresponding thermal expansion of the clamping fixture in boring were negligible. Thus, the fixture was assumed to be rigid and only the machined workpiece geometry was modelled by this FEM mesh. The spiral mesh [15], as shown in the concept in Fig. 4.8(a), was utilized to model the workpiece after finish boring. Elements were lined up with the spiral tool trajectory in boring. The FEM mesh for workpiece temperature, as shown in the cross-sectional view, had 307 layers of

0.15 mm thickness (the same as the feed per revolution in finish boring). Around the circumference, each revolution contained 360 elements (0.68 mm in the bore circumferential direction). In the 9.25 mm radial direction, there were 12 elements with 0.2 mm thickness for the inner most element and thickness of the adjacent element increased with a constant ratio of 1.25. This spiral mesh setup had two small 0.15 mm steps at the start and end of the mesh to form a cylindrical structure, as shown in the Section B-B view in Fig. 4.8(b). This height was small compared to the workpiece height (46.05 mm) and its impact on the workpiece temperature was negligible. Due to the high cutting speed and short cutting time (less than 6 s) in finish boring, the temperature rise in the fixture was negligible.

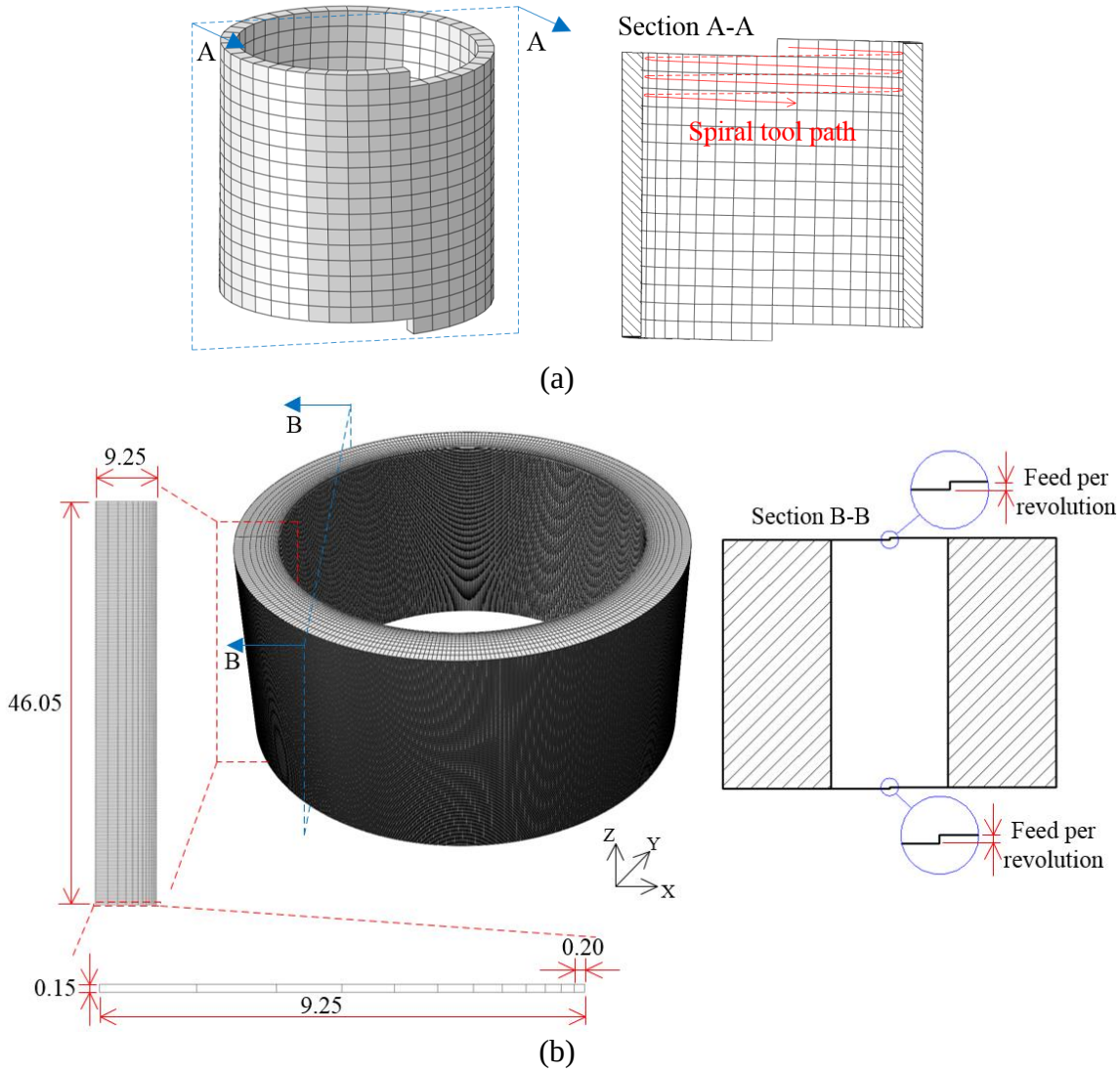

Figure 4.8 Mesh for FEM thermal model: (a) the concept of spiral mesh and (b) the spiral mesh for finish boring (unit: mm).

4.3.2.2 FEM Thermal Model for Workpiece Temperature

The ring heat model [15] was applied to determine the ratio of heat entering the workpiece (also known as heat partition) during boring. The concept of the ring heat model is shown in Fig. 4.9(a). A spiral ring shape heat flux of one revolution of tool path was moved step-by-step in the axial direction by one element height (the feed per revolution). The 3D 8-node linear element for heat transfer analysis (DC3D8 in ABAQUS) was selected to mesh the workpiece. The initial temperature was 27°C, the room temperature for finish boring experiment. All outer surfaces of the workpiece were assumed to be adiabatic for the dry cutting condition. In each time step, the heat flux was evenly applied on the 360 elemental surfaces of a spiral ring (78.3 mm in diameter and 0.15 mm in height) for the time duration of one spindle (or tool) revolution (0.019 s). The strength of surface heat flux, q, was determined using the inverse heat transfer method with the objective function minimizing the root-mean-square deviation (RMSD) between the experimentally measured and FEM predicted temperatures at six thermocouple locations over the duration of boring.

Based on the heat flux (q), spiral ring area (A), measured tangential cutting force ($F_{tangential}$) and cutting speed (v), the heat partition ratio, B, is:

$$B = \frac{qA}{F_{tangential}v} \tag{2}$$

B represents the ratio of total heat that left in the workpiece after machining.

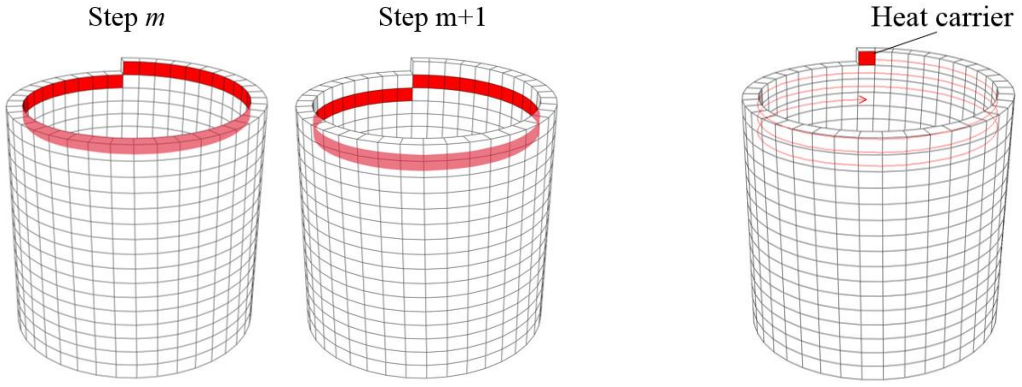

Figure 4.9 FEM workpiece temperature model concept: (a) ring heat model and (b) heat carrier model.

The heat carrier model [15], as shown in the concept in Fig. 4.9(b), was applied to simulate the spirally rotating heat flux entering the workpiece at the cutting region during boring. A moving isothermal heat carrier with the same trajectory and speed as the boring tool delivered a constant heat flux to the workpiece. The 3D 8-node brick element (C3D8T in ABAQUS) was selected to model the workpiece and the heat carrier to predict the workpiece temperature. Thermal conductance in the gap between the heat carrier and workpiece was 100 W/m·K. The fraction of total heat that flows into the workpiece, determined by the ring heat model, was uniformly added on the 0.68 mm (width) by 0.15 mm (height) heat carrier outer surface, matching to the bore surface. The ABAQUS/Explicit solver was used.

4.3.2.3 FEM Model for Workpiece Thermal Expansion

The 8-node linear brick element with reduced integration (C3D8R in ABAQUS) was selected to mesh the workpiece for thermal expansion modeling. The boundary conditions at three clamping areas (C1, C2, and C3) and bottom support area of the workpiece were highlighted (in red) in Fig. 4.10. Figure 4.10(a) shows the C1, C2, and C3 clamping areas in the workpiece. Figure 4.10(b) shows the ring-shaped bottom support area in the workpiece in contact with the top and bottom clamps of the fixture. Nodes on the workpiece surface in contact with three clamping areas (C1, C2, and C3 in Fig. 4.10(c)) were assumed to be fixed to model the tight clamping condition. Nodes on the workpiece bottom support area (as marked in Fig. 4.10(d)) was fixed along Z direction. The effect of 7 mm gap between top and bottom clamps was neglected.

The workpiece temperature from the heat carrier model in Sec. 4.3.2.2 was used as the input in this model to calculate the workpiece thermal expansion during boring.

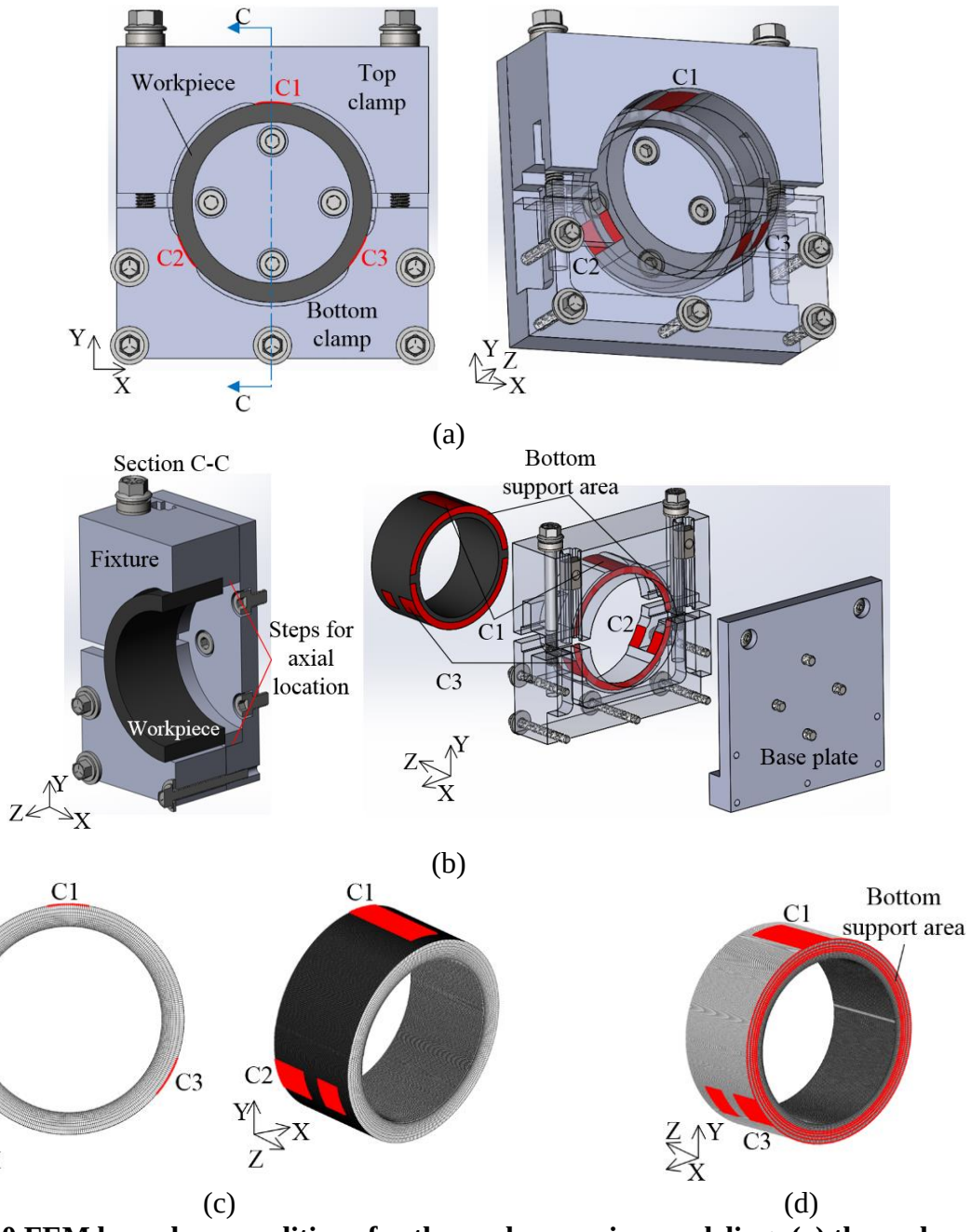

Figure 4.10 FEM boundary conditions for thermal expansion modeling: (a) three clamping areas, (b) cross-sectional and exploded views of the workpiece bottom support area, (c) three clamping areas in workpiece FEM mesh, and (d) bottom support area in workpiece FEM mesh.

4.4 Experimental Results

4.4.1 Cutting Force

The measured F_x, F_y, F_z, and M_z are shown in Fig. 4.11. F_x and F_y showed two sinusoidal curves with 90° phase shift while F_z and M_z were almost constant. The average axial cutting force F_z is 28.3 N and average axial moment M_z is 3.78 N·m. The average tangential cutting force calculated based on M_z and finished bore diameter (78.3 mm) was 96.6 N. The radial cutting force calculated based on this average tangential force and the average force in the XY plane (vector sum of F_x and F_y) was 53.2 N.

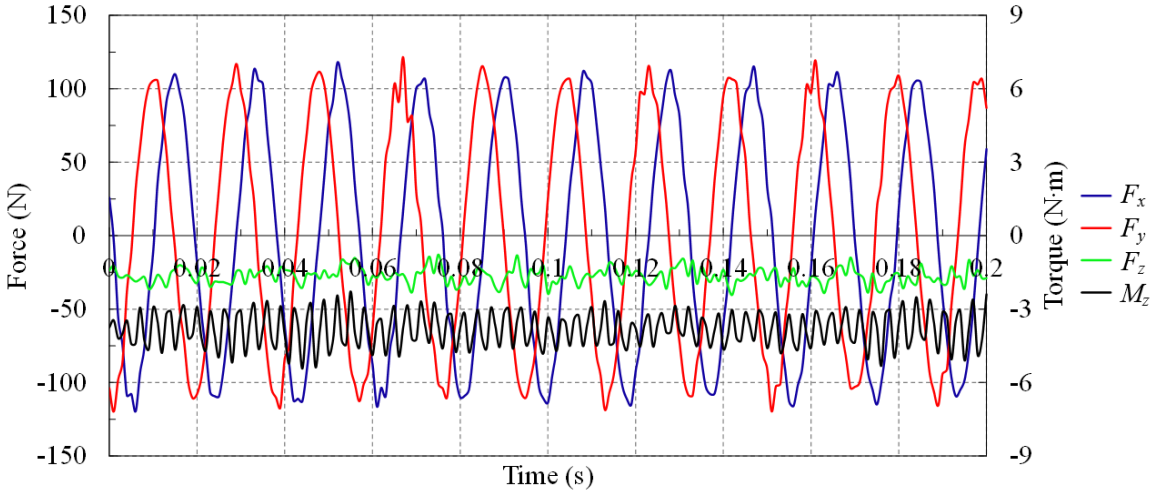

Figure 4.11 F_x, F_y, F_z, and M_z measured by piezoelectric dynamometer for a 0.2 s time span during boring.

4.4.2 Clamping Force

Measured forces at two clamping bolts (LC1 and LC2) before and after finish boring are listed in Table 4.2. The clamping force drop, 77 N in LC1 and 72 N in LC2, was measured after boring. This change in clamping force was the input in FEM analysis to estimate the workpiece deformation.

Table 4.2 Clamping forces measured by load cells before and after finish boring.

Load cell	Clamping force (N)		Change in Clamping force (N)
	Before boring	After boring	
LC1	1,494	1,417	77
LC2	1,500	1,428	72

4.4.3 Workpiece Temperature

On the sectioned workpiece shown in Fig. 4.2(d), the distance between the thermocouple hole bottom and the finished bore surface were measured. Results are listed in Table 4.3. Temperatures measured by six thermocouples (defined in Fig. 4.2(d)) during finish boring are shown in Fig. 4.12. The temperature increased as the cutting tool passed the nearby thermocouple. The workpiece temperature increased by about 4 to 6°C at different radial locations during boring.

Table 4.3 Distance between thermocouple hole bottom and bore surface.

Thermocouple number	Distance (mm)
TC1	2.7
TC2	3.1
TC3	3.5
TC4	3.7
TC5	2.8
TC6	3.0

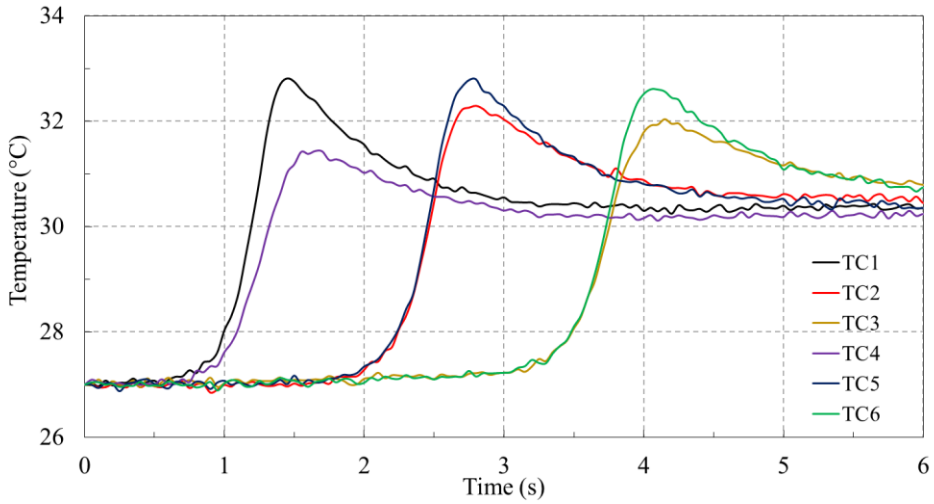

Figure 4.12 Temperature measurement by six embedded thermocouples.

4.4.4 CMM Measurements

CMM measurement results of the finished bore are shown in Fig. 4.13. Based on the minimum zone method, the cylindricity of the bore was 5.6 μm. The radial deviation of measurement points in six layers (Fig. 4.3(d)) to the mean minimum zone reference cylinder (MZCY) are shown in the top view in Fig. 4.13(a). Two minimum zone reference circles (MZCIs) at 2.8 and –2.8 μm radial distance from the mean MZCY encompass all data points in six layers. The perspective view of this radial deviation of bore measurement in 6 layers is shown in Fig. 4.13(b).

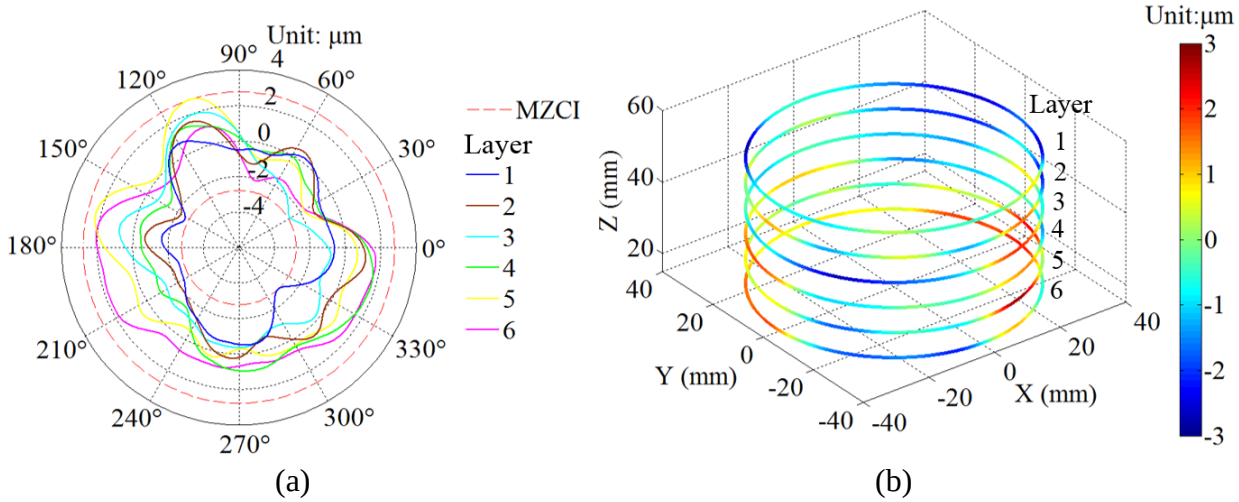

(a) (b)

Figure 4.13 CMM measurement results at six layers (5.6 μm cylindricity): (a) top view and (b) perspective view of radial deviation from mean MZCY.

4.4.5 Spindle Error Measurements

Displacements measured by two capacitive sensors X1 and Y1 at master ball #1 for 32 revolutions are shown in Figs. 4.14(a) and (b), respectively. As stated in Sec. 4.2.3, the wobble plate generated eccentricity in the master ball and a steady sinusoidal signal at capacitive displacement sensors, as evident by the shape in Figs. 4.14(a) and (b). Two sinusoidal curves at X1 and Y1 with the same period, amplitude, and 90° phase shift were fitted using the least square method [16, 17]. Period of the sinusoidal signal was determined by the spindle speed (3228 rpm). The amplitude of 5.5 μm and vertical shifts of –8.0 and 6.6 μm for X1 and Y1, respectively, were obtained for the best-fit sinusoidal curves shown in in Figs. 4.14 (a) and (b).

After removing the sinusoidal component in X1 and Y2, the spindle error motion ΔX_1 and ΔY_1 at master ball #1 is shown in Figs. 4.14(c) and (d) for 32 revolutions. Substituting ΔX_1 and ΔY_1 to Eq. (1), the spindle radial error motion Δr_1 at master ball #1 was calculated, as shown in Fig. 4.14(e). The average of Δr_1 in 32 revolutions was the synchronous error motion, as defined by ISO standard 230-7:2015 [14], of the spindle at master ball #1. Based on the minimum zone method, the magnitude of the synchronous error motion at master ball #1 was about 2.2 μm.

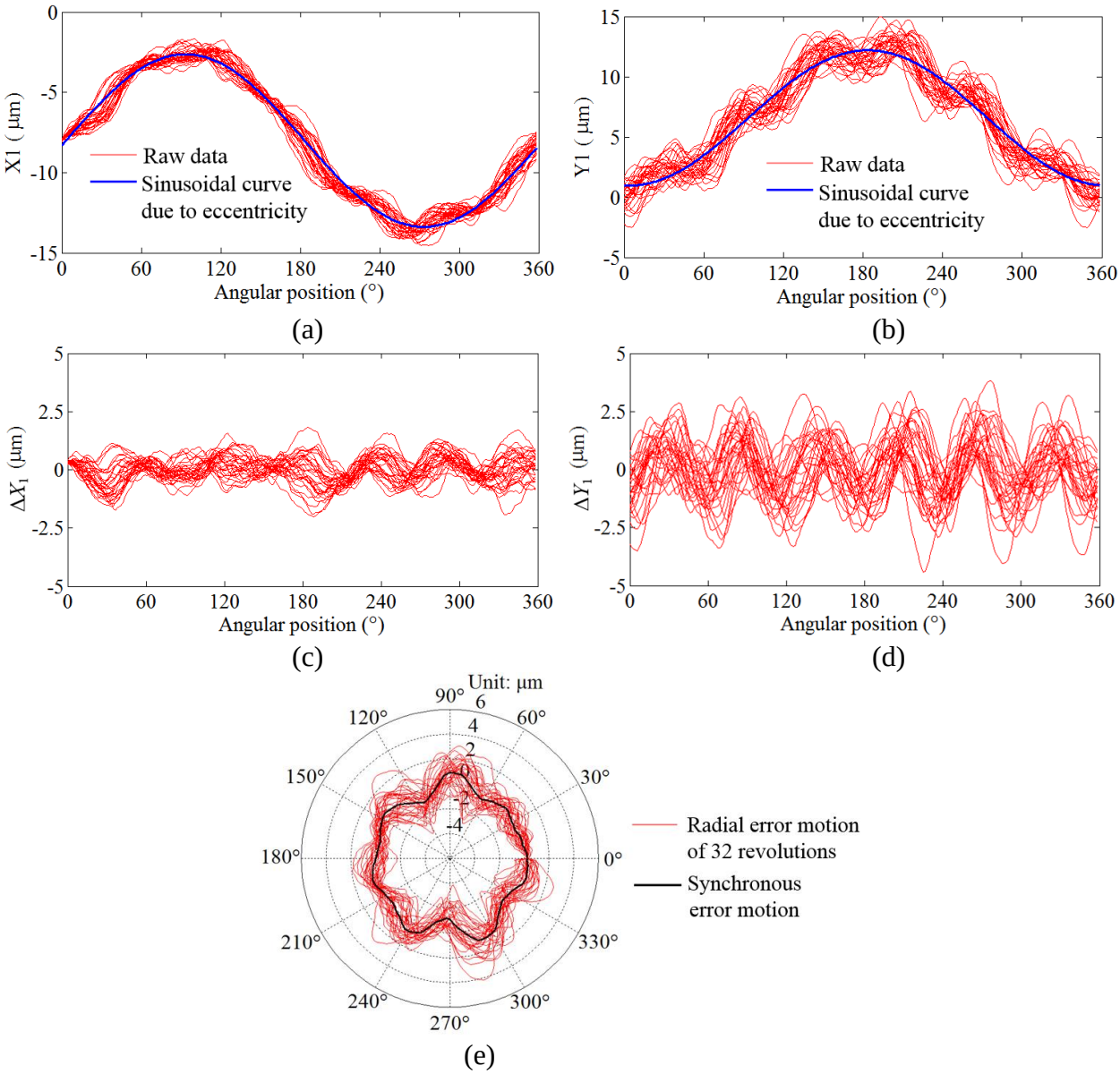

Figure 4.14 Spindle error of 32 revolutions at master ball #1: capacitive displacement sensor measurements at (a) X1 and (b) Y1, and error motions (c) Δ*X*1, (d) Δ*Y*1, and (e) Δ*r*1 and the synchronous error motion.

Repeating that process for capacitive sensors X2 and Y2, the spindle radial error motion (Δr_2) and the synchronous error motion at master ball #2, as shown in Fig. 4.15, was calculated. Since master ball #2 is closer to the spindle nose (see Fig. 4.4), the magnitude of the synchronous error motion at master ball #2 is smaller, about 1.1 μm.

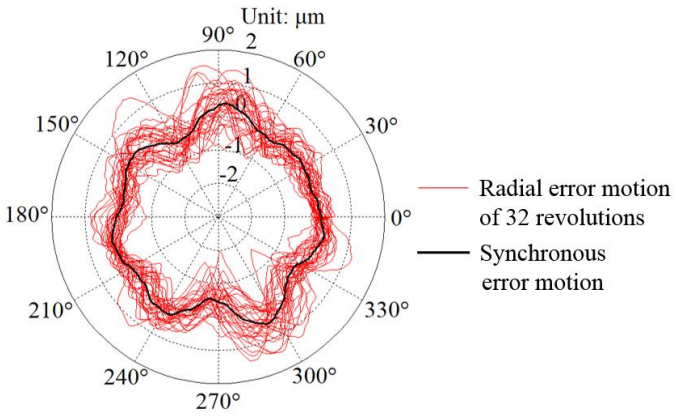

Figure 4.15 Spindle error motion at master ball #2.

The radial error motion at the tool tip, which is even further away from the spindle nose (Fig. 4.4), was obtained by linear extrapolation of the error motion at master balls #1 and #2 for 32 revolutions, as shown in Fig. 4.16(a). The average of these 32 data points for each angular position is the synchronous error motion at the tool tip, as shown in Fig. 4.16(a). Based on the minimum zone method, this synchronous error motion at the tool tip was 3.2 µm, as shown in Fig. 4.16(b).

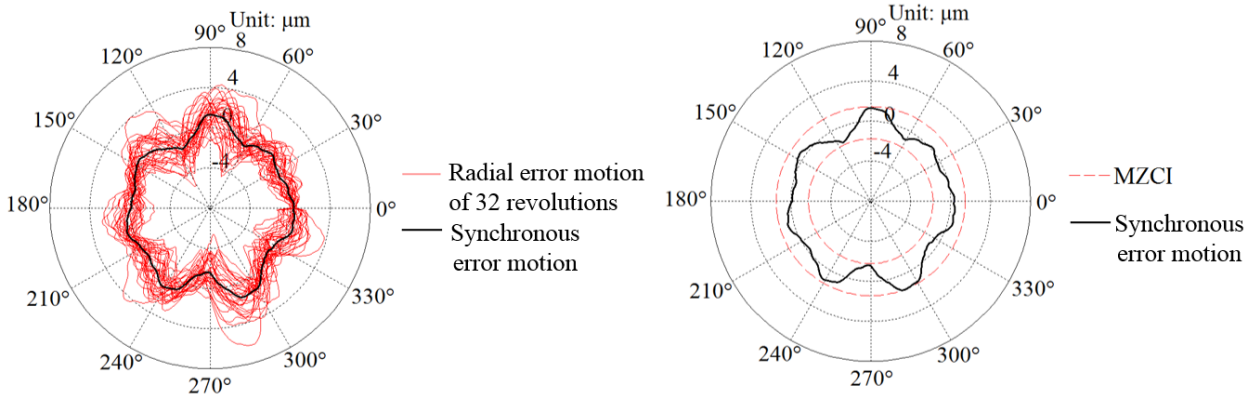

(a) (b)

Figure 4.16 (a) Spindle error motion at the boring tool tip based on linear extrapolation of spindle errors at master balls #1 and #2 and (b) radial deviation of the synchronous error motion from mean MZCI (synchronous error motion value= 3.2 µm).

Polar plots of the radial spindle error measurement in Figs. 4.14 to 4.16 do not correlate to X and Y axes in Fig. 4.4. The angular position of the spindle was determined by eccentricity of the master ball, which did not correlate to the machine axes. The angular correlation between the radial error motion of the boring tool tip and its center of rotation is not known in the spindle

error experimental setup. This will be further discussed in Sec. 4.6 (Fig. 4.26) when the bore cylindricity is related to the spindle error measurements.

4.5 FEM Modelling Results

FEM simulations were conducted to calculate the workpiece temperature and thermal expansion (Sec. 4.5.1) and the workpiece deformation due to cutting force (Sec. 4.5.2) and clamping forces (Sec. 4.5.3). Combination of these deformation results is presented in Sec. 4.5.4.

4.5.1 Workpiece Temperature and Thermal Expansion

Based on the thermocouple measured temperatures (Fig. 4.12), thermocouple positions from the finished bore surface (Table 4.3), and ring heat model (Sec. 4.3.2.2), the inverse heat transfer solution of the surface heat flux, q, was 9.01 MW/m^2. The RMSD between FEM thermal model prediction and experimental measurements was small, 0.5°C. The heat partition ratio, B, calculated using Eq. (2), was 0.26, which was identical to that in previous study under the same cutting condition [15].

The heat flux applied to the heat carrier was 3242 MW/m^2. The heat carrier delivers the surface heat to the workpiece. FEM predicted and measured temperatures at six thermocouple locations in the workpiece are shown in Fig. 4.17. Good agreements were achieved (particularly in the stage before the peak temperature) and demonstrated the accuracy of inverse heat transfer solution and FEM thermal models. Discrepancies between FEM predictions and experimental measurements after peak temperatures are likely due to the assumption of adiabatic boundary condition. During boring, the heat conduction to the fixture and convection to the surrounding caused the decrease in workpiece temperature. Its effect was more obvious after the cutting tool passed through the thermocouple. The bore surface temperature prediction by the heat carrier model was about 240°C, close to the 215°C measured experimentally using the tool-foil thermocouple method under the same cutting condition [15].

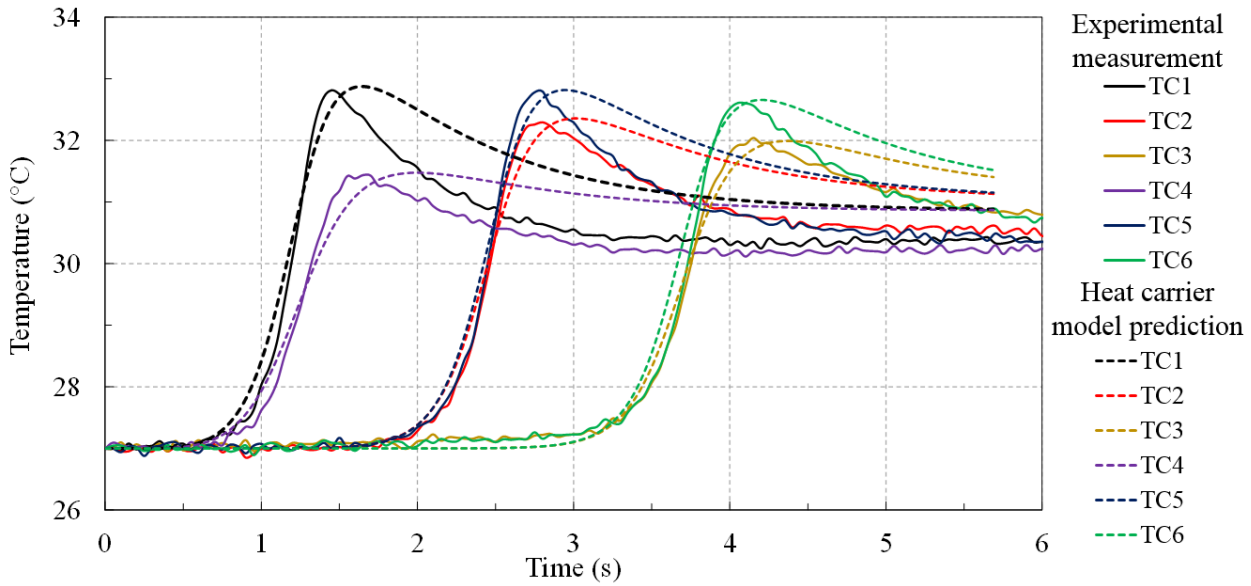

Figure 4.17 Comparison between FEM predicted and experimentally measured temperatures at six thermocouple locations.

Figure 4.18 shows FEM predicted workpiece thermal expansion in the radial direction with the cutting tool 14, 28, and 42 mm from the top (or outside) face of the workpiece during boring. Due to temperature rise, the workpiece expanded outwards between three clamping jaw locations (marked as A_1, A_2, and A_3 in Figs. 4.18(a) and (b)), where the workpiece extended beyond three jaws without clamping support, as illustrated in Fig. 4.5. In three areas close to clamping jaws (marked as B_1, B_2, and B_3 in Fig. 4.18), the workpiece deformed toward the center axis due to the fixed boundary condition at C1, C2, and C3. At the tool-workpiece cutting area, the workpiece temperature is high and concentrated, which has resulted in the locally inward expansion (toward the center axis of the workpiece) on the bore inner surface.

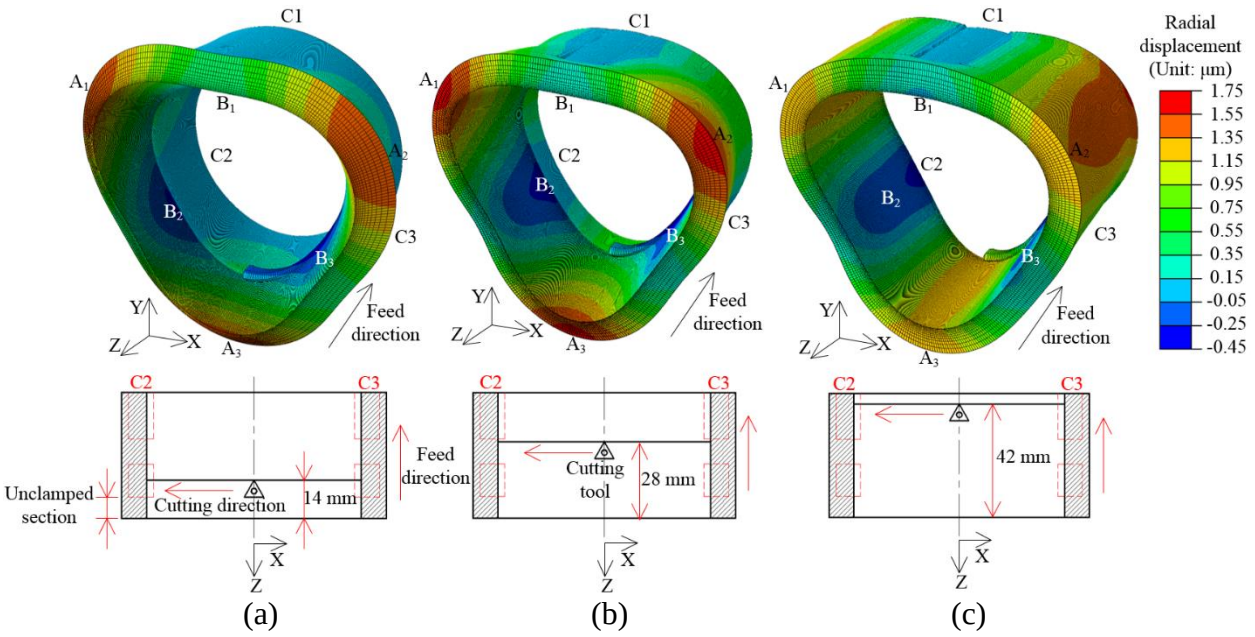

Figure 4.18 FEM model predicted workpiece thermal expansion (deformation scaled by 10,000 times) in three axial locations: (a) 14 mm, (b) 28 mm, and (c) 42 mm from the top of the bore.

The magnitude of workpiece thermal expansion at the cutting tip determined the actual depth of cut and the bore shape, which is illustrated in Fig. 4.19. This shape is represented by the deviation in the radial direction from mean MZCY in six layers (with the same height as in CMM measurement). The outside layer (Layer 1) has an open three-lobe shape. The inside layers (Layers 4, 5, and 6) have smaller size due to clamping constraints and heat accumulation. Due to the three-haw chuck, all layers have the three-lobe geometry. Deviations from the mean MZCY in the radial direction are summarized in Fig. 4.19(b). Cylindricity of the deformed bore shape due to thermal expansion was about 1.7 μm based on the minimum zone method.

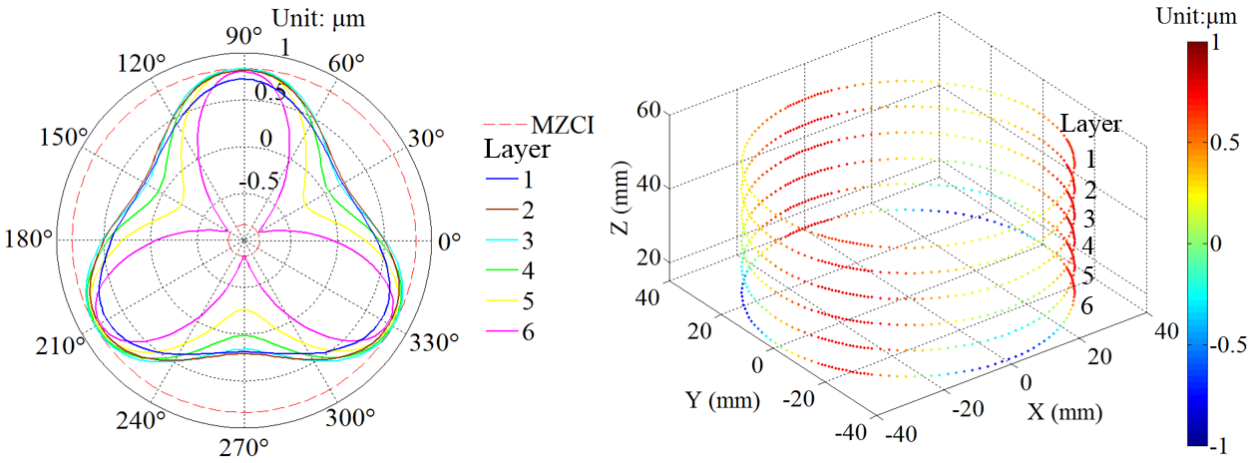

(a) (b)

Figure 4.19 Thermal expansion in six layers (1.7 µm cylindricity): (a) top view and (b) perspective view of radial deviation from mean MZCY.

4.5.2 Workpiece Deformation due to Cutting Force

During boring, the workpiece deforms due to cutting force. Such deformation changes the depth of cut and bore geometry. By applying the measured cutting force on the bore surface in FEM, simulation results of workpiece radial deformation due to cutting force can be estimated. For example, at cutting tool 21.0 mm from top of the bore face, the deformation of the workpiece and fixture are shown in Fig. 4.20. At this instance, the largest workpiece deformation occurred at the node where three nodal force components, $F_{tangential}$ (96.6 N), F_{radial} (53.2 N), and F_{axial} (28.3 N) were applied. The radially outward elastic deformation at the cutting point resulted in a smaller depth of cut and led to less material removal during boring and smaller bore size after boring.

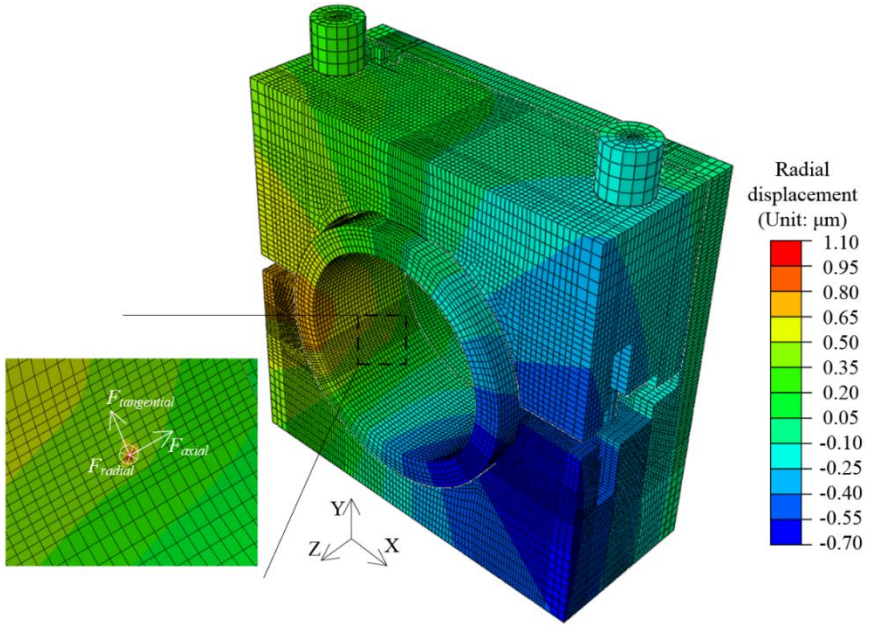

Figure 4.20 Simulation result of workpiece deformation due to cutting force.

The shape of the bore after finish boring due to the workpiece deformation by cutting force is shown in Figure 4.21. This shape is also represented by the deviation in the radial direction from mean MZCY in 6 layers with the same height as in CMM measurement. The cylindricity was about 0.8 μm. Layers 1 and 2 and areas adjacent to C1, C2, and C3 with clamping support had smaller bore size due to larger radial deformation at cutting edge, smaller depth of cut, and less material removal in boring.

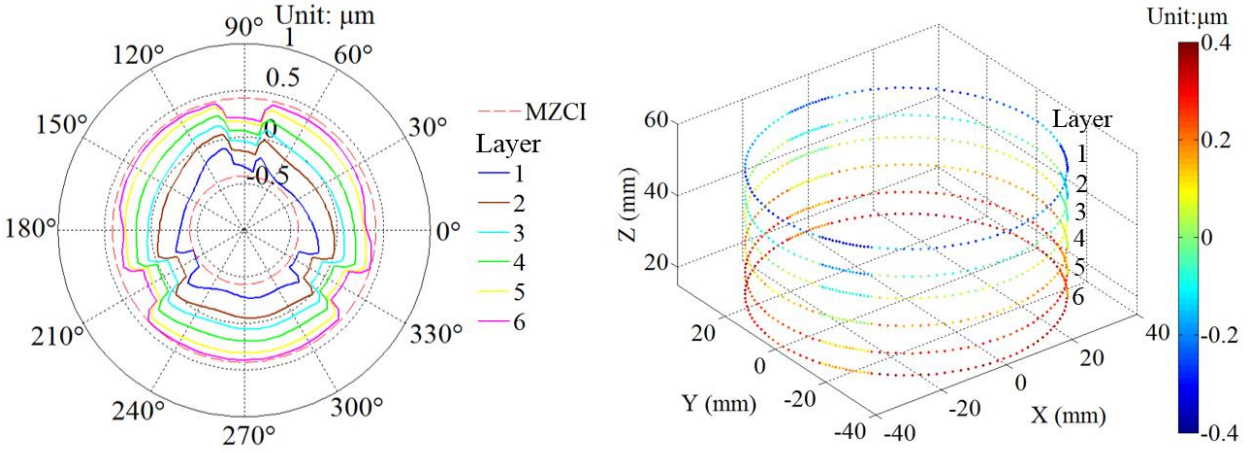

(a) (b)

Figure 4.21 Result of workpiece deformation due to cutting force along six CMM layers (0.8 μm cylindricity): (a) top view and (b) perspective view of radial deviation from mean MZCY.

4.5.3 Workpiece Deformation due to Clamping Forces

FEM simulation of workpiece deformation due to clamping forces is shown in Fig. 4.22. The changes in clamping forces (77 N in LC1 and 72 N in LC2) were applied on the cross sections of the two clamping bolts. Figure 4.23 shows the radial deviations from mean MZCY due to decreases in clamping forces after boring. The cylindricity was about 1.9 µm.

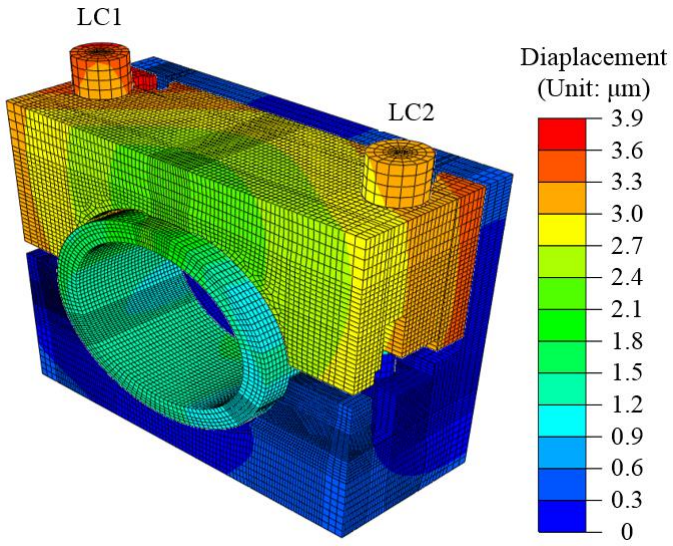

Figure 4.22 FEM results of workpiece deformation due to clamping forces at LC1 and LC2.

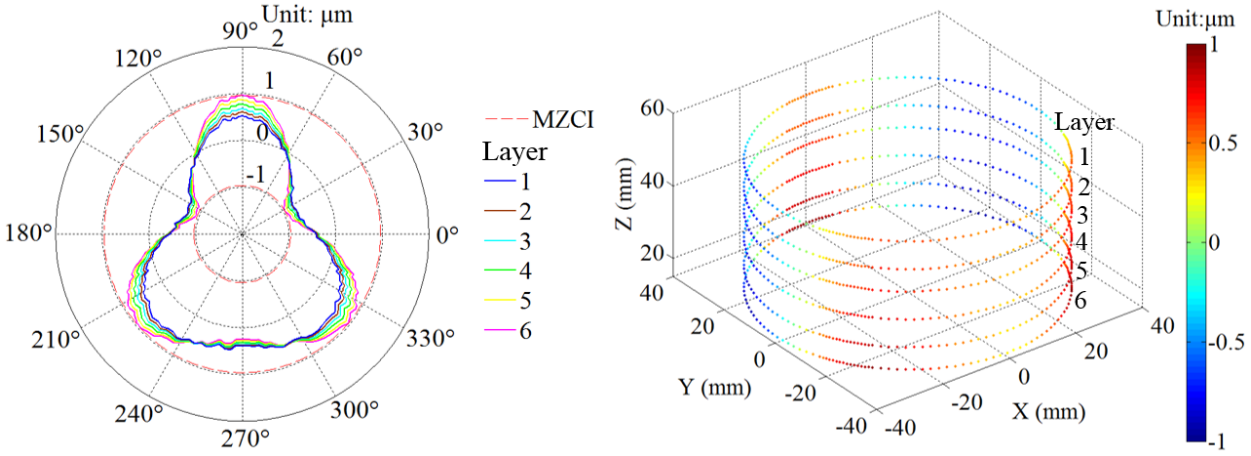

(a) (b)

Figure 4.23 Workpiece deformation due to the clamping forces after boring along six CMM layers (1.9 µm cylindricity): (a) top view and (b) perspective view of radial deviation from mean MZCY.

4.5.4 Combination of Workpiece Thermal Expansion and Deformation due to Cutting Force and Clamping Forces

Based on the assumption that all error sources were independent from each other, workpiece deformations in Secs. 4.5.1 to 4.5.3 were linearly added together. The obtained deformed bore shapes were used for cylindricity evaluations based on the minimum zone method. As shown in Fig. 4.24(a), the combination of workpiece thermal expansion and deformation due to cutting force resulted a combined cylindricity of 1.5 μm with maximum workpiece radial deformation of 1.7 μm. This is much smaller than the magnitude reported in previous rough and semi-finish boring research [5,6]. Adding the effect of change in clamping forces, the cylindricity was about 3.4 μm, as shown in Fig. 4.24(b).

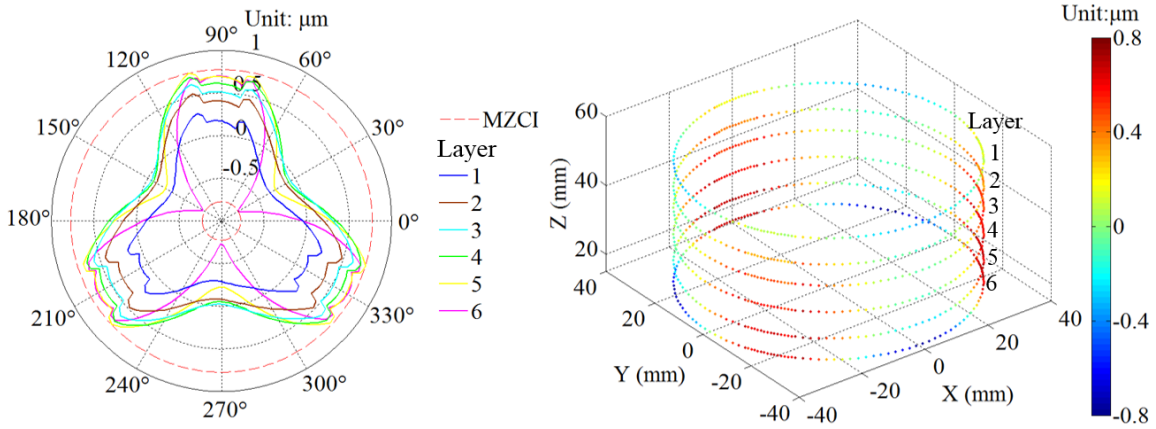

(a)

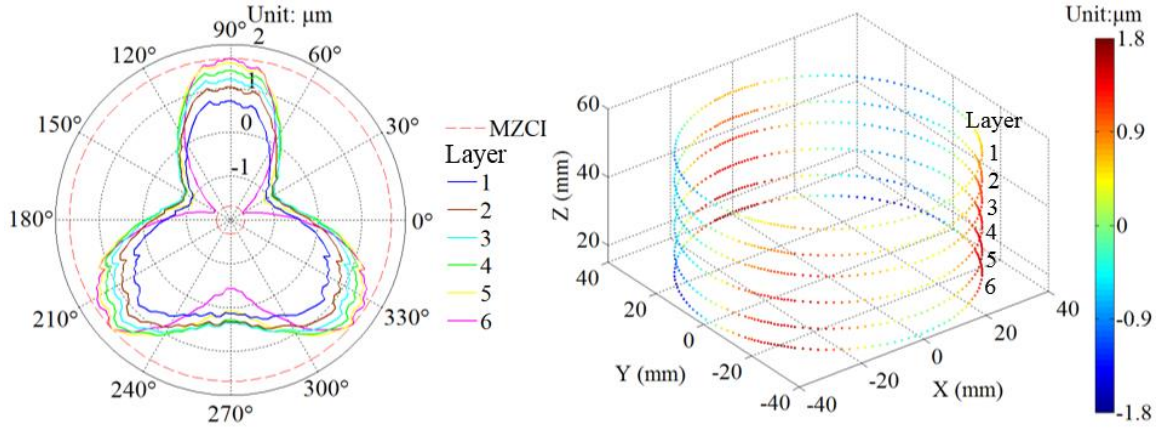

(b)

Figure 4.24 Radial deviation of combined FEM deformation results from mean MZCY in top and perspective views along six CMM layers: (a) combined thermal expansion and workpiece deformation due to cutting force (1.5 μm cylindricity) and (b) combined all three effects (thermal expansion and workpiece deformation due to cutting and clamping forces) (3.4 μm cylindricity).

4.6 Cylindricity Error Source Identification

The difference in cylindricity between the FEM (3.4 μm in Sec. 4.5.4) and CMM measurement (5.6 μm in Sec. 4.4.4) indicates that the spindle error (Sec. 4.4.5) needs to be considered. Harmonic analysis, which converts the data from angular to frequency domain, is applied to analyze the CMM measurements, spindle error, and FEM workpiece deformation result. The sampling frequency was set the same as the number of data points per revolution. As a result, the *n*-th order harmonic corresponds to *n* undulations per revolution (upr) or *n*-lobe shape of the bore.

Results of the harmonic analysis of the CMM measurement (Fig. 4.13(a)), FEM analysis (Fig. 4.24(b)), and spindle error (Fig. 4.16(a)) are shown in Figs. 4.25(a), (b), and (c), respectively. In Fig. 4.25(a), since the CMM centers the bore in measurement, the eccentricity and magnitude of the 1st harmonic (one lobe) are both zero. The shape of bore measured by CMM covers a broad spectrum from 2nd to 10th harmonics. The combined FEM result of the bore deformation, as shown in Fig. 4.25(b), has only 1st to 3rd harmonics. Higher order harmonic deformation was not revealed in FEM. On the contrary, the spindle radial error motion was dominated by 4th and higher order harmonics, as shown in Fig. 4.25(c).

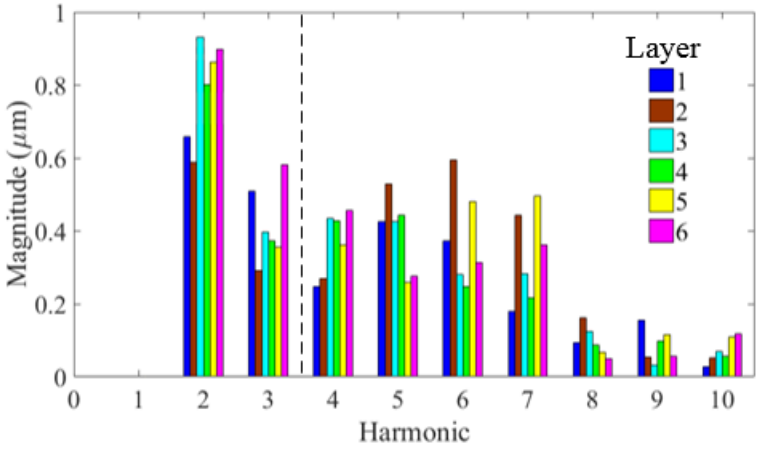

(a)

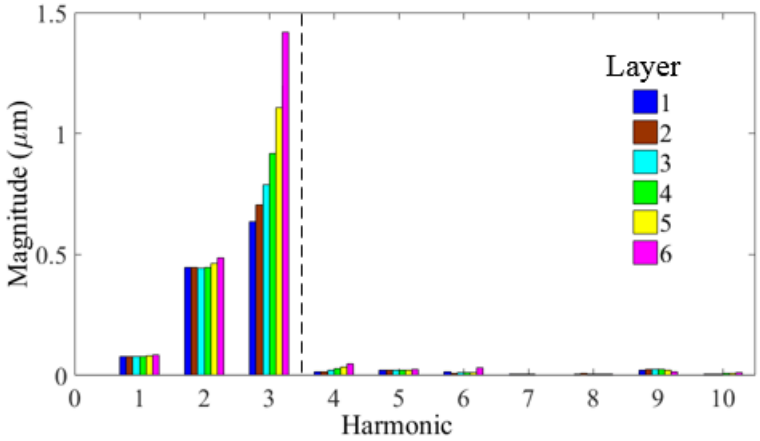

(b)

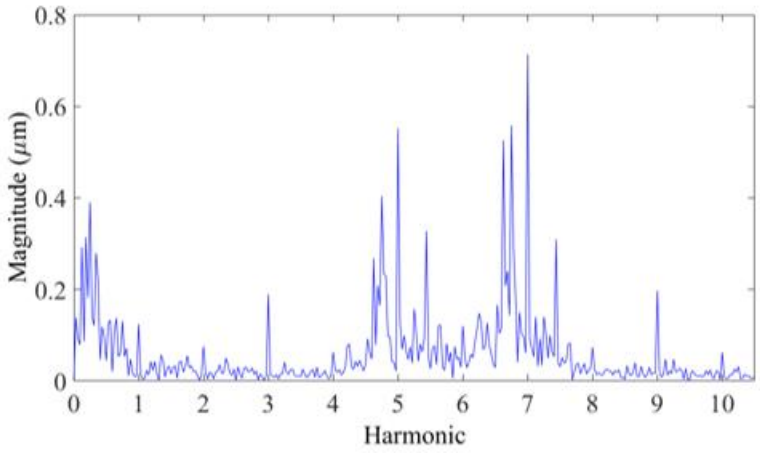

(c)

Figure 4.25 Harmonic analysis: (a) CMM measurements, (b) FEM, and (c) spindle radial error motion.

The CMM measurement was decomposed into two parts, as shown in Fig. 4.25, the low (1st to 3rd) and high (above 4th) harmonics. The radial deviation from the mean MZCY of the

high (4th to 10th) harmonics in CMM measurement for six layers is shown in Fig. 4.26(a). The 2.9 µm cylindricity is close to the 3.2 µm radial synchronous error motion at the tool tip (Fig. 4.16). The average of the radial deviation from the mean MZCY in six layers, as shown in Fig. 4.26(b), matches well with the radial synchronous error motion (Fig. 4.16) from spindle error measurement. By rotating the spindle radial synchronous error motion by 175° counterclockwise, the RMSD between the high harmonic CMM measurement and spindle radial synchronous error motion was minimized to 0.6 µm and the shapes, as shown in Fig. 4.26(b), matched well.

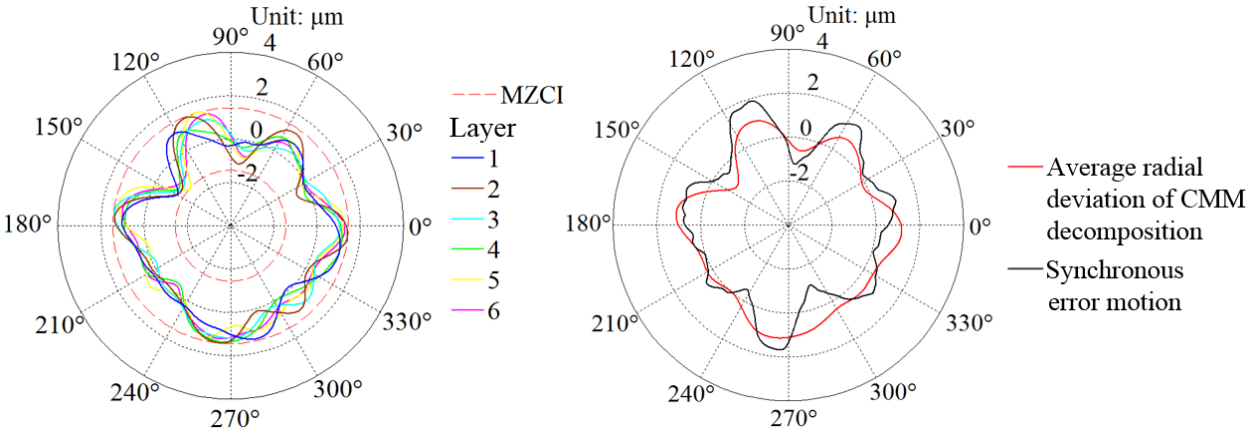

Figure 4.26 (a) The radial deviation from mean MZCY in polar plot of the 4th to 10th harmonics in CMM measurement (2.9 µm cylindricity) and (b) average radial deviation of six layers compared to the spindle radial synchronous error motion (after rotating 175° to minimize RMSD).

4.7 Discussions

In finish boring, spindle error from the machine tool can be a dominant error source for the bore cylindricity, especially for higher order harmonics (beyond 3rd harmonic). In this study, the spindle error (3.2 µm radial synchronous error motion) contributed to almost half of the overall cylindricity error (5.6 µm in CMM measurement). In this study, the experimentally measured spindle error did not correlate with the machine axes. To solve this issue, a new spindle error measurement system may be utilized. An encoder can be used to determine the angular position of the spindle with an index sensor to identify the starting point of each revolution instead of using eccentricity of the master balls. The unknown correlation between the radial error motion of the boring tool tip and its center of rotation can be obtained based on the boring bar geometry and

spindle nose - tool holder interface configuration. After correlating the spindle error result with the machine axes, cylindricity error induced by the four error sources discussed in this study can be directly combined together to match the CMM measurement result.

Radial deviation of the workpiece due to thermal expansion and cutting force is mainly determined by the structure of the workpiece and fixture. Three-lobe is the dominant harmonic for the three-jaw fixture in this study. For a typical closed-deck engine block with four bolts per cylinder, the four-lobe distortion would be the main component. In this dry finish boring study, the cylindricity error contributed by thermal expansion and workpiece deformation due to cutting force was small, around 1.5 μm. Its effect is not as dominant as that in rough and semi-finish boring due to reduced cutting force and lower workpiece temperature in finish boring. Flood cooling or minimum quantity lubrication in boring will further reduce the thermal effect on finish boring geometry.

The lower order harmonic part resulted in 3.8 μm cylindricity, which correlated with the 3.4 μm FEM result. The discrepancy is likely due to the clamping load change. The FEM analysis in Sec. 5 shows that clamping is a major source of cylindricity error in this study. In automotive powertrain production, due to the different clamping fixture setup (smaller clamping force along radial direction of the cylinder) and large volume of the engine block workpiece, impact of the clamping force induced cylindricity error will be smaller.

4.8 Conclusions

Experimental and FEM analysis was conducted in this study to identify bore cylindricity error sources in finish boring. The spindle radial error motion was found to be the dominant error source under finish boring cutting condition with small depth of cut and feed rate and relatively low cutting force, workpiece deformation, and thermal expansion. Further advancements are still needed to study the unloading effect on bore geometry and optimization of the boring process parameters to achieve better bore shape.

References

[1] Z. Ma, N.A. Henein, W. Bryzik, J. Glidewell, Break-in liner wear and piston ring assembly friction in a spark-ignited engine, Tribology Transactions 41 (4) (1998) 497-504.

[2] M.R. Rodrigues, S.F. Porto, S.F., Torque plate honing on block cylinder bores, SAE Technical Paper 931679 (1993).

[3] K. Matsuo, S. Kiga, S. Murata, N. Satou, H. Miyake, K. Suzuki, K. Sugiyama, T. Monchujo, Reduction of piston system friction by applying a bore circularity machining technique to the cylinder block, SAE Technical Paper 2005-01-1656 (2005).

[4] J.D. Meadows, Geometric Dimensioning and Tolerancing Handbook: Applications, Analysis & Measurement, ASME Press, New York, 2009.

[5] G. Subramani, S. G. Kapoor, R. E. DeVor, A model for the prediction of bore cylindricity during machining, Journal of Engineering for Industry 115 (1) (1993) 15-22.

[6] N.N. Kakade, J.G. Chow, Finite element analysis of engine bore distortions during boring operation, Journal of Manufacturing Science and Engineering 115 (4) (1993) 379-384.

[7] Y. Zheng, H. Li, W.W. Olson, J.W. Sutherland, Evaluating cutting fluid effects on cylinder boring surface errors by inverse heat transfer and finite element methods, Journal of Manufacturing Science and Engineering 122 (3) (2000) 377-383.

[8] Y. Tang, K. Ding, H. Sasahara, K. Nishimura, T. Watanabe, Clarification of the amount of machining error resulting from the cutting force and thermal expansion during the cylinder liner boring process, Journal of Advanced Mechanical Design, Systems, and Manufacturing 2 (3) (2008) 332-342.

[9] K. Kim, K.F. Eman, S.M. Wu, In-process control of cylindricity in boring operations, Journal of Engineering for Industry 109 (4) (1987) 291-296.

[10] D.L. Martin, A.N. Tabenkin, F.G. Parsons, Precision spindle and bearing error analysis, International Journal of Machine Tools and Manufacture 35 (2) (1995) 187-193.

[11] J.P. Choi, S.J. Lee, H.D. Kwon, Roundness error prediction with a volumetric error model including spindle error motions of a machine tool, The International Journal of Advanced Manufacturing Technology 21 (12) (2003) 923-928.

[12] G. Subramani, M.C. Whitmore, S.G. Kapoor, R.E. DeVor, Temperature distribution in a hollow cylindrical workpiece during machining: theoretical model and experimental results, Journal of Engineering for Industry 113 (4) (1991) 373-380.

[13] ISO 12180-1:2011 - Geometrical product specifications (GPS) -- Cylindricity -- Part 1: Vocabulary and parameters of cylindrical form, n.d. ⟨http://www.iso.org/iso/home/store/catalogue_tc/catalogue_detail.htm?csnumber=53611⟩ (accessed 17.02.05).

[14] ISO 230-7:2015 - Test code for machine tools -- Part 7: Geometric accuracy of axes of rotation, n.d. ⟨http://www.iso.org/iso/catalogue_detail.htm?csnumber=56624⟩ (accessed 17.02.05).

[15] L. Chen, B.L. Tai, J.A. Yang, A.J. Shih, Experimental study and finite element modeling of workpiece temperature in finish cylinder boring, Journal of Manufacturing Science and Engineering (submitted).

[16] T.F. Coleman, Y. Li, On the convergence of interior-reflective Newton methods for nonlinear minimization subject to bounds, Mathematical Programming 67 (1) (1994) 189-224.

[17] T.F. Coleman, Y. Li, An interior trust region approach for nonlinear minimization subject to bounds, SIAM Journal on Optimization 6 (2) (1996) 418-445.

CHAPTER 5
CONCLUSIONS AND FUTURE WORK

5.1 Conclusions

This dissertation studied the cylindrical machining workpiece temperature and bore cylindricity for finish cylinder boring process. Both experimental methods and finite element method (FEM) models were developed to evaluate workpiece temperature in cylindrical machining processes. Experimental and FEM analysis was combined to identify the bore cylindricity error sources in finish boring process was developed.

The major achievements of this dissertation are:

(1) *The experimental methods for machined surface workpiece temperature measurement in hard turning*:

Two experimental methods were developed to measure workpiece peak temperature on machined surface near the cutting edge in hard turning. The tool-foil thermocouple method was developed to estimate the machined surface temperature using a metal foil embedded in the workpiece to measure the tool tip temperature. The embedded thermocouple method was developed utilizing a thermocouple embedded in the tool with its tip continuously sliding on the machined surface behind the cutting edge. Good correlation was observed between predictions of two methods under various hard turning parameters. Both methods were able to experimentally measure workpiece temperature on the machined surface near the cutting edge, providing valuable temperature information for white layer prevention in hard turning. The tool-foil thermocouple method was also applicable to machined surface workpiece temperature evaluation in cylinder boring.

(2) *FEM modelling technics for workpiece temperature distribution in finish boring process*:

Four FEM models, adopted and modified from previous studies, namely the advection model, surface heat model, heat carrier model and ring heat model, were used to predict the workpiece temperature in finish cylinder boring. All four models were validated through experiments and showed the capability of predicting global temperature rise. Each model had its own advantages, disadvantages and applicable scenarios. The comparison result provided a guideline for selecting the proper modelling concept for cylindrical machining studies.

(3) *Error source identification of bore cylindricity in finish boring*:

Experimental and FEM analysis was combined to identify the bore cylindricity error sources in finish cylinder boring, taking into account thermal expansion of workpiece, workpiece deformation due to cutting and clamping forces and spindle error from the machine tool. Experiments were conducted to measure the workpiece temperature, spindle error, and bore shape. FEM was conducted to analyze the heat flux, workpiece temperature and deformation. Harmonic analysis was applied to distinguish and identify the high and low harmonic error sources. Good agreement was observed between high (above 4th) harmonics in coordinate measuring machine (CMM) measurement and radial synchronous error motion of the spindle. Lower (1st to 3rd) harmonics in CMM measurement correlated with the thermal expansion and workpiece deformation due to cutting and clamping forces.

The conclusions and important findings in this research can be summarized as follows:

(1) Both the tool-foil thermocouple and embedded thermocouple methods were feasible for the measurement of machined surface workpiece temperature in hard turning.

(2) All four FEM thermal models could predict global workpiece temperature in finish boring. Locally, the advection model provided the most accurate peak temperature prediction on machined surface while the surface heat model and #3 the heat carrier model gave peak temperature predictions within 2-3% discrepancy. Only the ring

heat model lacked the competency of predicting the peak temperature around the cutting edge.

(3) For finish boring study on workpiece temperature distribution and machined bore distortion, to reach the best trade-off between accuracy and computational efficiency, it is suggested to use the ring heat model first to determine the portion of heat left in the workpiece through inverse heat transfer method and then the heat carrier model to determine the detailed workpiece temperature profile near the tool tip.

(4) The spindle radial error motion was found to be the dominant bore cylindricity error source for finish boring in this study. For finish cylinder boring in engine block production, it is suggested to evaluate the machine tool accuracy and include spindle error in the bore cylindricity error budget.

(5) The effect of thermal expansion and cutting force induced workpiece deformation on bore cylindricity was not as significant in finish boring as reported in rough and semi-finish boring processes.

5.2 Future Work

The experimental methods, numerical models and methodologies proposed in this dissertation can be further improved and extended in the following directions:

(1) Metallurgical studies can be conducted to correlate the experimentally measured machined surface temperature to the initiation of the white layer in hard turning. Models can be developed to predict white layer depth based on workpiece temperature measurements.

(2) A database can be created through hard turning experiments to link cutting conditions and cutting time to a machined surface workpiece temperature prediction for the prevention of white layer formation and tool life management in hard turning.

(3) FEM modelling technics can be explored to efficiently apply the developed thermal model concepts to complex geometry like an engine block.

(4) Thermal studies in this dissertation were mainly based on dry cutting condition. Both experimental and modelling approaches can be modified and explored to be applied to flood cooling or minimum quantity lubrication cutting conditions.

(5) In the FEM models to predict bore cylindricity, thermal expansion and workpiece deformation due to cutting and clamping forces were assumed independent. The prediction error due to this assumption can be quantified. Especially for clamping force induced deformation, instead of estimating it by using the change in clamping forces and perfect cylinder geometry, a comprehensive model can be developed to simulate the thermal-mechanical coupled material removal process and the corresponding structure rebalance for a better understanding of the unloading effect.

(6) Some bore cylindricity error sources like residual stress and tool wear were not included in the error source identification in this study. Further research can be conducted to take these error sources into consideration.

(7) The developed cylindricity error source identification approach can be further advanced to be applied to a real engine block geometry for the optimization of the boring process parameters.